DESIGN AND FABRICATION OF MICRONEEDLES FOR DRUG DELIVERY

JI JING

NATIONAL UNIVERSITY OF SINGAPORE

2007

DESIGN AND FABRICATION OF MICRONEEDLES FOR DRUG DELIVERY

JI JING

(*B.Eng.,M.Eng., NWPU, CHINA*)

A THESIS SUBMITTED

FOR THE DEGREE OF DOCTOR OF PHILOSOPHY

DEPARTMENT OF MECHANICAL ENGINEERING

NATIONAL UNIVERSITY OF SINGAPORE

2007

Acknowledgements

I'm very thankful that I have the opportunity to do my graduate study at National University of Singapore. My four years here have been challenging, but the knowledge and experience which I learnt at NUS will benefit me in the years to come.

I would like to thank Professor Francis, EH Tay, my advisor, for providing the opportunity to work on microneedles for the drug delivery project. He was always a source of support during my graduate. At my first group meeting in Dr. Tay's group, he encouraged us to be innovative researchers. I am very interested in the microfabrication technology. Dr. Tay provided fantastic research opportunities in doing microfabrication. He had always allowed students to explore their own interests and really make research projects their own.

I would like to thank Professor Miao Jianming, for the helpful discussion and suggestions about my research and answering my microfabrication processing questions. Dr. Miao was able to provide process equipment for my work. After meeting with Dr. Miao a few times, I found out that he can do much more than providing the equipment, he was a true visionary with a deep understanding about the microfabrication technology.

I would like to thank Professor Yung C. Liang and Professor Yoo Won Jong, for participating in my Qualifying Examination, as well as being thesis committee members.

I would like to thank all the members of the MEMS lab and MNSI, ZhaoYi, Wei Jiashen, Li Jun, Gao Chunping,Yu Liming, Shi Yu, and Nyan Myo Naing, for their suggestions and sharing of experience over the years.

I would like to thank the medical device group in IBN, for providing an opportunity to learn microfabrication technology.

I would like to thank NTU Micromachining Center staff, for their kindness to help me with setting up new experiments or working with new equipment.

I would like to thank my friends in Singapore, China, and Unite States, for encouraging me when I was frustrated. Especially, for my best friend, Zhu Xia, we always forgot the time when we were on the phone. I appreciate the friendships she has provided.

Most important of all, I would like to thank Xun Guo, my husband, for the innumerable sacrifices he has made to walk this journey with me. His unwavering support during my

graduate study and his suggestions on my research made those tough days much easier. He is always staying there for me and watching over me.

I also would like to thank my parents and the rest of my family, for their understanding and continual support. I would like to thank my mum and dad for their unlimited love.

Ji Jing
January 2007

Table of Contents

Pages

Summary

Microneedle array with biodegradable porous tips was designed and fabricated for the application of transdermal drug delivery. Pyramidal silicon microneedles with sharp tips were fabricated by an isotropic etching process in an inductively coupled plasma (ICP) etcher. Using full factorial factors design method, each effect of the process variables on etching results was analyzed to optimize the isotropic etching process. The results of the design of experiment (DOE) model indicate that the etching rates are predominantly depended on the ion flux which is related with coil power and SF_6 flow rate. The higher V/L ratio benefits from lower SF_6 flow rate and higher platen power. The photoresist etching rate increases with platen power increasing. Moreover, the process of photoresist reflow was developed to expose top part of tips which were deposited by a silicon nitride layer. In addition, the biodegradable porous tips were then fabricated by an optimized anodic electrochemical etching process. The electrochemical etching conditions were characterized to investigate the formation of porous silicon with various porosities and structures. It was found that macroporous structure was formed in HF/acetone nitride (MeCN) electrolyte while the nanoporous structure was observed using HF/ethanol solution. The higher porosity was obtained at higher current density and longer etching time.

An analytical model was built up to predict the critical loadings of a microneedle during insertion. For a single porous tip needle with 30 μm height, a 5 μm length of top side, and a 20 μm length of bottom side, the critical buckling force is found to be 39 mN which is much greater than the force (~3.25 mN) required for insertion into the skin. The critical bending force for the needle is found to be 0.6 mN, which is also greater than the bending force (~0.24 mN) exerted during insertion. The variation in width dimensions that would lead to borderline (1.3 N) capacity was characterized to determine the values of width dimensions. Microneedle insertion experiments were carried out to investigate the insertion ability of the fabricated microneedle arrays. The results of insertion test verify that the fabricated microneedle array with porous tips is able to create microholes on the skin.

A microsystem consisting of a hollow silicon microneedle array and glass pump components was further designed and fabricated for injection. Dimensions for the inner channel and actuator mechanism were designed to deliver a desired flow rate. In the design, a 10 by 10 microneedle array with inner diameters ranged from 14 μm to 16 μm could deliver water at 100 μL in 60 seconds. The high aspect ratio, hollow microneedle array was fabricated using a dual-step dry etching process which includes deep reactive ion etching (DRIE) and isotropic etching. In addition, an optimized HF/HCL solution was developed to fabricate the glass components. Atomic force microscope (AFM) images of the etched glasses verified that the quality of surface was improved by using the solution, HF/HCl with the ratio 10:1 in volume.

List of Tables

Pages

List of Figures

Pages

List of Symbols

a	length of top side of a pyramidal structure, μm
A	interfacial surface area, μm^2
b	length of bottom side of a pyramidal structure, μm
c	perpendicular distance from the neutral axis to the point farthest away from the neutral axis
d_{31}	piezoelectric constant
D	diameter of the microneedle
D_G	the diameter of glass member
D_{PZT}	the diameter of PZT disc
f	frequency
F	force applied by the needle
F_z	the body force
E	Young's modulus of the material
G	roughness of skin
G_c	crack fracture toughness of skin
G_p	puncture fracture roughness
H	length of the cross-section of a pyramidal structure
I	moment of inertia

L	length of needle
L_d	the length of diffuser
M	the bending moment
P	loading force
P_{cr}	buckling force
P_t	bending force
p	pressure
p_1	the actuation pressure
p_2	the output pressure
Q	volumetric flow rate
S	section modulus, which is represented by I/c
t_{PZT}	the thickness of PZT disc
t_G	glass Membrane thickness, mm
W	the work of fracture of the material
W_1	the neck width for inlet
W_2	the neck width for outlet
$V_{x,}$	the velocity of the fluid in x direction
V_y	the velocity of the fluid in y direction
V_z	the velocity of the fluid z direction
x	the axial position of the needle,

x_i	the displacement during insertion,
y	the deflected shape of needle
Δp	the pressure drop $\Delta p = p_1 - p_2$
ΔV	the volume flow per stroke,
ΔZ	is the deflection in a stroke

Greek Symbols

α	the tapering angle is $\tan^{-1}((b-a)/2L)$
γ	the divergence angle
θ	the pre-exponential constant
μ	the viscosity
τ	the exponential constant
ρ	the density
ε_τ	relative Permittivity

Chapter 1 Introduction

1.1 Overview of Microneedle Applications

Microneedles have emerged as important biomedical devices because they have immense potential applications in different areas of medicine and biology. Microneedles reduce both insertion pain and tissue damage in a patient due to their small size. The efficiency of transdermal drug delivery will be increased due to the increased skin permeability when the skin barrier is pieced mechanically by microneedles [1]. Furthermore, microneedles allow the implementation of time varying delivery of different therapeutics, which is essential for a more effective drug delivery system. The direct delivery of DNA/portent based drugs into the metabolic system and the continuous delivery of insulin to a diabetic patient have been reported using microneedles [2]. Side-effects of overdose in drug delivery can be minimized by using the microneedle based microsystems due to their potential ability to release drugs in precise controlled dosage. Microneedles may also be used to extract and analyze bodily fluids such that a patient's metabolite can be continuous monitored [3][4]. Other applications of microneedle technology include sample collection for biological analysis, delivery of cell or cellular extract based vaccines, and sample handling. Essentially, microneedles are able to provide the interconnection between the microscopic and macroscopic world [5].

1.1.1 Motivation of Research on Microneedle

During a needle insertion, the damage to the tissue and the likelihood of infection occurring at the site of insertion are directly related to the size of the needle. Currently, needles used in common medical applications range from 7 gauge (the largest) to 33 gauge (the smallest) on the Stubs scale. Twenty-one gauge needles, which have a 813 μm (0.032 inch) outside diameter and a 495 μm (0.0195 inch) inside diameter, are most commonly used for drawing blood. The smallest 33 gauge needles have a 203 μm (0.008 inch) outside diameter and a 89 μm (0.0035 inch) inside diameter. Hypodermic needles are normally made from a stainless steel tube which is drawn through progressively smaller dies. However, it is not feasible to fabricate needles with a diameter less than 200 μm using this method. In a bid to fabricate microneedle with dementions less than 100 μm, micrfabrication technologies such as lithography and thin film deposition have been applied so as to minimalize the invasion effects and reduce the likelihood of infection.

In the transdermal drug delivery systems, microneedles have the significant advantage over other transdermal delivery approaches which include chemical enhancer, electroporation, iontophoresis, sonophoresis, magnetophoresis and thermal energy of increasing permeability of the skin [6].The microneedles mechanically create the pathway through the upper skin layer and pierce the upper epidermis so as to increase skin permeability and, therefore, improve drug delivery efficiency. With microholes in the skin, the drug delivery relied mainly on the

subsequent drug absorption into the bloodstream rather than the drug composition and concentration. The absorption of fluid through the microholes occurs at a much faster rate than permeation of the same fluid across the skin. Microneedles could provide a promised potential to deliver the sophisticated drugs, which are not feasible to be delivered in traditional methods due to the poor absorption and enzymatic degradation in the gastrointestinal tract or liver, to the blood stream.

In the delivery of drug to local tissues, microneedles were used to transport drugs in less administered dose to certain target location in order to avoid side effects encountered in the systemic delivery. Microsystems which consist of microneedles, sensors, micropumps, valves and flow channel are designed to deliver precise doses of drugs in the tissues. Such concepts were formulated in recent research [7]. The microsystem will allow a lower drug dosage to be injected over a longer period of time. This technique helps to maintain a constant drug concentration in the blood and hence, avoid the side effects associated with a high concentration bolus injection. Therefore, the microsystem has great potential for the controlled precise delivery.

Microneedle may also be used to sample body fluids for analysis. The miniaturization of fluidic devices enables portable devices to be designed for continuous metabolite monitoring of a person. The portable devices can be used to monitor the glucose level for a diabetes patient. The

sampling devices may also be used in cellular operation such as delivery RNA/DNA to cells/embryo [8].

1.1.2 Specific Applications of Microneedle in Drug and Gene Delivery

Microneedles, which have the capability of piercing skin or other tissues, can be used to deliver drugs through the skin, into a blood vessel, or into a cell [9]. With the advanced microfabrication technologies, microneedles which are fabricated using several materials such as silicon, glass, metal, and polymer have been developed. The microneedles have been fabricated in-plane, where the needle is parallel to the substrate, or out-of-plane, where the needle structure is perpendicular to the substrate. Many of fabricated microneedles are designed for transdermal therapies to deliver drugs such as insulin and heparin. On the other hand, microneedles can also be used for local delivery of other drugs, for example, drugs in anti-restenosis and anti-tumor therapies.

In transdermal drug delivery, microneedles are designed to painlessly deliver drugs into subcutaneous tissue with the rate at therapy level by enhancing skin permeability. The microneedles have the ability to transport sophisticated drugs to epidermis layer with significant therapeutic effects [10]. The earliest silicon microneedle array, fabricated by a reactive ion etching (RIE) process, could increase the skin permeability by up to four orders of magnitude using a fluorescent dye, calcein [11]. A hollow metal tube array and a hollow metal

microneedle array were subsequently demonstrated for transdermal delivery application [12]. These metal microneedles were fabricated by forming polymer or silicon molds and electrodepositing nickel, gold or other metals onto the molds. These hollow microneedles were inserted into human epidermis and were shown to increase skin permeability by up to five orders of magnitude above the assay sensitivity limit. More recently, Park *et al* developed biodegradable polymer microneedle array using PDMS mold for replication of the microneedles [13]. This polymer microneedle array had the ability to increase skin permeability by up to three orders of magnitude in *in vitro* experiments; and the microneedle using biodegradable polymer was show to be clinically applicable. In the above studies, the increase in skin permeability was observed in both skin test methods: with microneedles (inserted and left in skin) and without microneedles (inserted and removed from skin). Applications of microneedles which were fabricated from metal sheets for in vivo transdermal delivery of drugs such as insulin, oligodeoxynucleotide (ODN) and protein vaccine have been reported. Martanto *et al* fabricated the solid metal microneedle array by laser-cutting the shape of each needle out of a stainless steel sheet [14]. During medical trial test, an insulin solution was placed on top of the microneedle array which was then inserted into skin for four hours. A significant effect on blood glucose levels was observed. In another study, other types of metal microneedle arrays were etched from titanium sheets or stainless steel sheets. Drugs were subsequently coated on the surface to enhance the effect of *in vivo* transdermal delivery. Using these microneedle arrays, Lin *et al* demonstrated that the ODN delivery flux reached 8.08+0.06 $\mu g/cm^2/h$; and high ODN

concentration was found in the deep skin layer [15]. Matriano *et al* also applied these microneedle arrays to protein vaccine delivery and achieved high delivery rates of up to 20 μg in 5s [16].

Furthermore, microneedles are fabricated to deliver target drugs to a specific region or tissue in the body in order to avoid detrimental effects that could result from delivering certain drugs systemically. By using microneedle, it is possible to delivery very small and precise amounts of bioactive compounds into highly localized areas of neural tissue. The minimal invasion can also be realized in the neural operation. A multichannel silicon probe has been fabricated to deliver such compounds into neural tissue while simultaneously recording electrical signals from neurons and electrically stimulating neurons *in vivo* [45]. In addition, when the region of a tumor has been identified, a microneedle could deliver continuously anti-tumor drugs in chemotherapy by direct injection of drugs into the tumor or around the tumor so as to minimize the effect on healthy cells.

Microneedle has huge potential application in the therapy for diabetes due to its ability to continuously realize low dosage delivery of insulin. It can also monitor the glucose level in the bloodstream in real-time when they are integrated with other microsensors. Microneedle also has the ability to deliver DNA vaccinations and antibiotics into metabolic system. Moreover, microneedle has great prospect to be used on the chemotherapy of tumor because it can localize

the drug delivery zone and reduce the side-effects significantly. In addition, microneedle has the ability to delivery genetic materials into cells for cellular research. Hollow microcapillaries have been fabricated for injection of DNA and florescent dyes into animal/plant cells [18].

1.2 Overview of Microfabrication Technology

Microfabrication technology has traditionally been used to produce microelectronic devices such as microprocessors. In the early years, the fabrication technology for silicon based structures focused on lithography, etching, and deposition. In 1990's, microfabrication technology has been further developed. Besides IC based methods, other fabrication processes such as micromolding, wire electro discharge machining, laser machining, ion and electro beam machining and dicing were also exploited for miniaturization [19]. The surface micromachining and bulk micromachining are the two branches of microfabrication techniques. Surface micromachining is an addictive process, which consists of fabrication microstructure from deposited thin films [20]. The bulk micromachining is a subtractive process that uses the selective removal of materials from substrate to form microstructures [21].

Microfabrication technology was widely used in various fields. The most notable applications include the fabrication of accelerometers [22], nozzles [23], microreactors [24], micorpumps [25] and micro-turbine engines [26]. More recently, the microfabrication technology has been increasingly used to machine micro-scale devices related to biological applications [27][28].

Compared to the numerous biological applications such as biosensors and fluidic microdevices for sample separation, the use of microfabrication in the drug delivery has been limited. One potential approach was to use microneedles to achieve optimum therapeutic effect for new drugs. With the application of advanced microfabrication technology, novel microdevices would be fabricated to fulfill the requirements for drug delivery.

1.3 Thesis Objectives

The specific objectives of this thesis are to:

(1) Develop microneedle with biodegradable porous tips to solve the biocompatibility issues of microneedle in clinical application

(2) Optimize the microfabrication processes, such as the isotropic etching in inductivity coupled plasma (ICP) etcher and anodic electrochemical etching in HF/organic electrolytes for microneedle fabrication

(3) Build the model of microfabricated microneedle structure inserted into skin to predicate the condition of fracture by the analysis of critical bending and buckling loadings

(4) Design microsystem consisting of hollow microneedles, fluidic channels, pressure cavity and actuation components for drug to be delivered of at desired volume and flow rate into localized tissues

(5) Develop and optimize process to fabricate hollow microneedle array with structural enhancement and to achieve good etched surface quality for silicon and glass components

Figure 1.1 shows the schematic of the designed microneedle array with biodegradable porous tips. To our best knowledge, it is the first time to propose the approach for improvement of biocompatibility of silicon microneedles application. The microneedle with biodegradable tips provides an attractive approach in clinical applications. The microneedles with porous tips have the potential advantage in big molecular delivery due to the sorption of porous structure. The fabricated biodegradable porous tip is expected to exhibit several advantages over conventional microneedles, especially when the microneedle had broken off and remained in the skin; and the porous structure may provide an alternative approach for drugs loading. The analytical solutions of critical loading for microneedle structures design may explain the performances of the needles during the insertion into the skin. The theoretical analysis for fracture could be used to predict the quantitative values of force needed to cause needle fracture using different shapes of cross-section of other fix-free column structures. Results of characterization of isotropic

etching process in high density plasma etcher may be useful for fabricating other devices such as microlens and AFM tips using similar etching procedure.

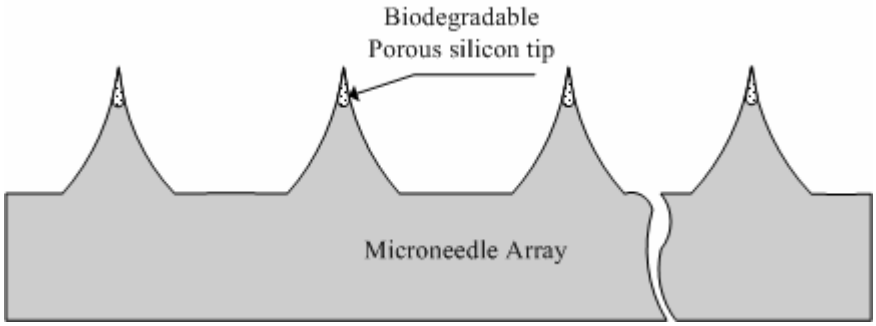

Figure 1.1 Schematic of designed microneedle array with biodegradable tips

Figure 1.2 shows the schematic of the designed microsystem based on a hollow microneedle array and piezoelectric actuation mechanism. The prototype has the ability to deliver precise and controlled volume of drugs into tissue. Fabrication of hollow microneedle arrays is always a challenge. Current reported microneedles have been achieved with mask with diameter ~200-450 μm. The out-of-plane hollow microneedle array with its high aspect ratio structure and small size should have minimal tissue damage and reduce side effects in local delivery applications. In the design, the dimension of mask is less than 100 μm so as to decrease the damage and likelihood of infection. The fabrication procedure, where isotropic etching in inductive coupled plasma (ICP) etcher and deep reactive ion etching (DRIE) are combined to achieve arrays of microneedle structure, may provide an approach to fabricate 3-D structure as compared with 2-D in silicon bulk machining. The investigation of an improved etchant would be applied for glass deep etching. In addition, the microsystem could be integrated with digital

circuit to control the actuator components for controlled release so as to reduce the toxicity effect of constant delivery.

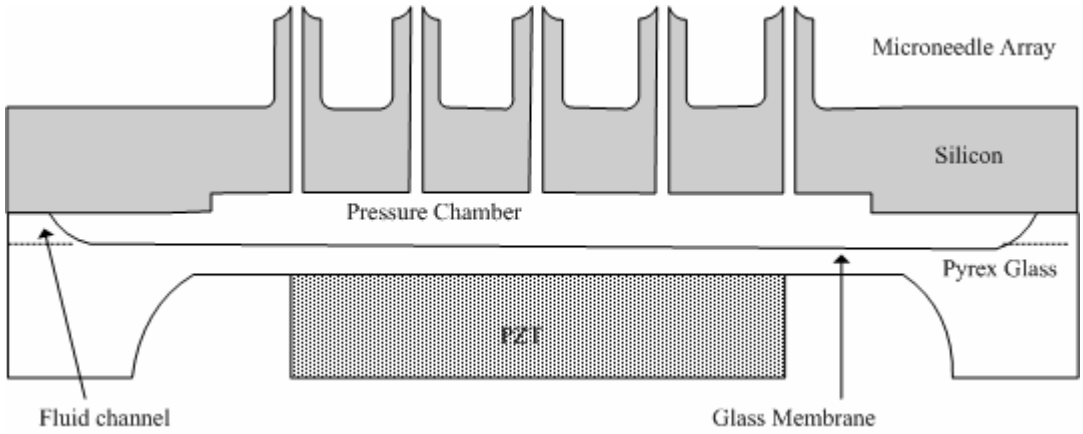

Figure 1.2 Schematic of microsystem based on hollow microneedle array

Chapter 2 Review of Microfabricated Microneedles

2.1 Microneedles in Transdermal Drug Delivery

Transdermal drug delivery is an alternative method for delivery of DNA/protein based drugs. These drugs which have sophisticated compounds are not suitable to be delivered by traditional methods due to their ineffective delivery routes [29]. Figure 2.1 shows the structure of skin. The outer layer is the stratum corneum (SC), which is a dead tissue of 10 μm~20 μm thickness. The next layer is viable epidermis (VE) of 50~100 μm thickness. The VE consists very few nerves and living cells that have blood vessels with capability of transporting drugs. The layer of Dermis (D) lies below the VE. This layer forms the bulk of the skin volume and contains nerves and blood vessels. The efficiency of transdermal drug delivery is significantly limited by low permeability of the SC. In addition, Figure 2.1 shows the current delivery mechanisms of different schemes for enhancement of the skin permeability. Label a represents transdermal diffusion which is related to chemical enhancer. Label b represents the iontophoresis which makes transport pathway through hair follicles. Label c represents the electroporation which disrupts the lipid bilayers. Label d represents microhole which is created by microneedle.

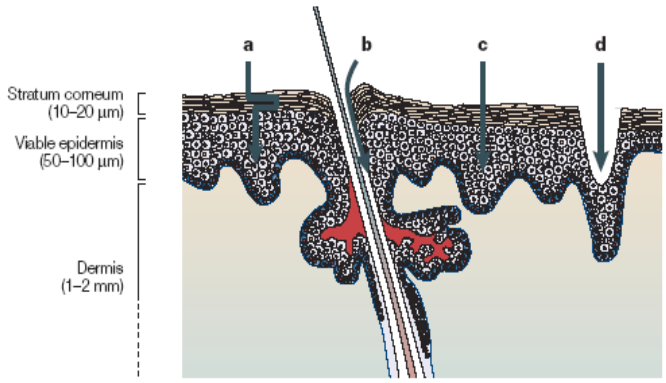

Figure 2.1 Schematic representation of a cross section through human skin [29]

Iontophoresis uses low voltage electric field through the skin to drive ionized molecules by electrophoresis and non-ionized molecules by electroosmosis [31][32]. Electroporation applies short electric pulse (microseconds to milliseconds) to create pores in skin for small drug or macromolecules transition [33]. Sonophoresis applies low frequency ultrasonic energy to disrupt the stratum corneum [34]. Thermal energy uses heat to increase the skin permeability and energy of drug molecules to enhance the transdermal transport [35]. In addition, magnetophoresis has also been applied in transdermal drug delivery using magnetic energy to increase drug flux across skin [36]. However, these methods usually accompany with the side effects of shin irritation [30]. Moreover, limited improvement of the drug absorption ratio was obtained using these methods. In addition, further study in clinical research is needed for these methods. A new research area of transdermal drug delivery is to physically create micron-scale holes in the SC using microneedles.

2.1.1 Microfabrication Technology

Figure 2.2 presents the fabricated microneedles which have been reported for transdermal delivery applications. Their fabrication processes are also summarized in this figure.

Henry *et al* conducted the first study to apply silicon microneedle array, which was fabricated by a reactive ion etching (RIE) process using SF_6/O_2 gases, in transdermal drug delivery [11][37]. Figure 2.2-(a) shows the fabricated microneedle array. The length of the silicon microneedle has been reported to be approximately 150 μm with sharp tips, whose radius is less than 1 μm. A chromium masking layer was deposited and patterned in 20 by 20 arrays of dots with 50-80 μm in diameter and 150 μm center-to-center spaces. The fabrication of the microneedle array was finished when the mask layer became totally undercut and fell off the microneedle tips.

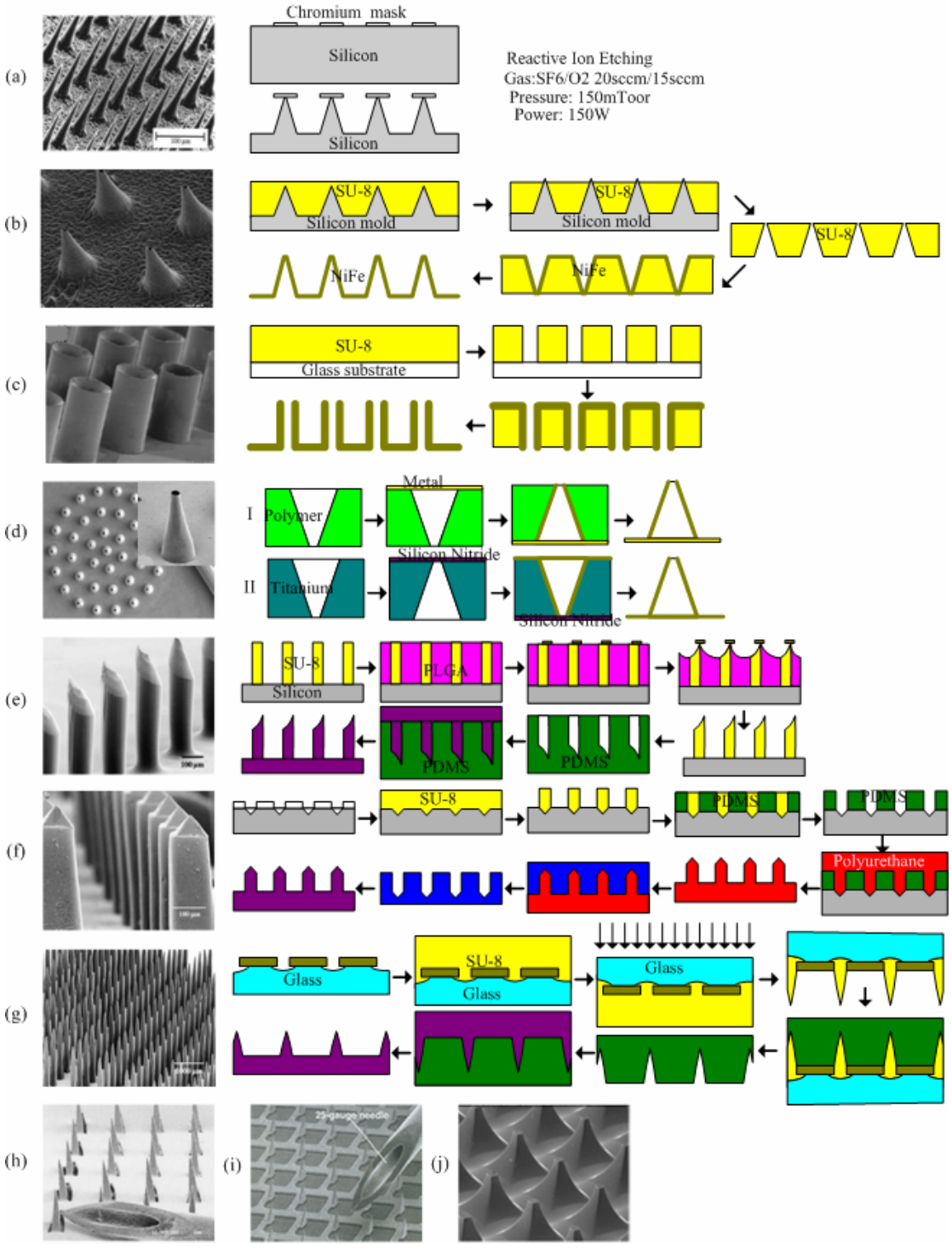

Figure 2.2 Micrographs of fabricated microneedles including microfabrication processes, for transdermal drug delivery ((a) Ref. [11, 37], (b, c) Ref. [38] (d) Ref. [39, 40] (e, f, g) Ref. [13, 41] (h) Ref. [14, 15] (i) Ref. [16] (j) Ref. [42])

Hollow microneedle arrays were subsequently fabricated by seeding metal to molds (Figure 2.2-(b)) [38]. The solid microneedle array (Figure 2.2-(a)) was used as a template to fabricate SU-8 mold. First, the SU-8 was cast onto the silicon microneedle array. After the upper layer of SU-8 was removed by plasma etching, the thick photoresist mold was formed. The NiFe was then filled into the mold to form microneedles by electroplating. Microtubes (Figure 2.2-(c)) were fabricated by defining mold in SU-8 epoxy and filling it by electroplating metals. A thick layer of SU-8 was patterned in vertical holes by the standard photolithography process. A conductive metal seed layer was then deposited onto the epoxy mold; and then a metal layer was electroplated to partially fill the mold. After the SU-8 mold was etched away, the microtubes were obtained. Deep reactive ion etching (DRIE) was also conducted in fabrication of the lumen for hollow silicon microneedle using an inductively coupled reactive ion etcher. This deep etch created arrays of holes through the silicon wafer; and the tapered wall of the microneedles was fabricated by reactive ion etching (RIE) process, which was used for fabrication of the solid microneedles in Figure 2.2-(a).

Davis *et al* developed laser micromachining process for microneedles fabrication [39][40]. The fabricated microneedles are shown in Figure 2.2-(d). Excimer (UV) and infrared (IR) laser machining were used to create molds for electro-deposition of metals. Mold materials included titanium and polymers such as polyimide and polyethylene terephthalate. In the process flow presented by Figure 2.2-(d)-I, an excimer laser drilled the desired microneedle geometry

through a polymer sheet, whose thickness determined the microneedle height. The polymer mold was then deposited by a seed layer of Ti /Cu /Ti, using direct current sputtering. The upper layer of titanium was removed using 2% hydrofluoric acid just prior to electroplating to expose the copper layer. The mold was then electroplated at certain current density to create the microneedle array. The plating duration determined the thickness of the metal wall. Finally, the polymer mold was dissolved; and the metal seed layer was removed, resulting in the fabricated microneedles. Figure 2.2-(d)-II shows another process fabrication the microneedle by a metal mold. An infrared laser was used to drill taped holes through a titanium sheet. The backside of the metal mold was deposited a thin silicon nitride (Si_3N_4) layer by PECVD to prevent electroplating onto the mold. The metal mold was subsequently electroplated with the desired constituent material to form microneedles. Lastly, the metal mold was etched to release the finial fabricated microneedles.

Biodegradable polymer microneedle arrays were further developed using microfabricated mold for replication of the microneedles [13][41]. Three prototypes of microneedle structures including beveled-tip, chisel-tip, and tapered-cone microneedles were micromachined in polylactic acid, polyglycolic acid, and their co-polymers. Figure 2.2-(e) shows the microneedles with beveled tips. The master for this microneedle was SU-8 epoxy cylinders with diameter of 100 μm. Subsequently, the space between cylinders was filled with a sacrificial polymer (PLGA) and the entire surface was coated with a thick layer of copper by

electron beam deposition. This copper layer was etched to leave a pattern of rectangles that asymmetrically covered the tops of the epoxy cylinders and some of the sacrificial polymer on one side of each cylinder. Reactive ion etching was conducted to partially remove the uncovered sacrificial layer and asymmetrically etch the tip of the adjacent epoxy cylinders. All remaining sacrificial polymer was removed by ethyl acetate, leaving an array of epoxy cylinders with asymmetrically beveled tips. In Figure 2.2-(f), the chisel-tip microneedles were fabricated using a combination of wet silicon etching and reactive ion etching of polymers. A layer of silicon nitride was deposited onto a silicon wafer by plasma enhanced chemical vapor deposition (PECVD) and patterned with array of square dots each measuring 100 μm. KOH etching was then applied to etch inverted pyramid-shaped holes. Etching occurred along the crystal plane to form tapered walls terminating in a sharp point. The wet etching process provides the chisel shape of the needle tips. To form the shape of the needle shaft, SU-8 epoxy photoresist was spinning coated onto the etched wafer; and a second mask was aligned with the silicon nitride pattern. After post-baking to crosslink the UV exposed SU-8 on a hotplate and then cooling, the non-crosslinked epoxy was developed with PGMEA. To finally make master needle structures, the space between the obelisk SU-8 structures was filled with PDMS. The crosslinked SU-8 was removed by reactive ion etching with oxygen plasma to leave a PDMS-silicon mold. Subsequently, polyurethane was poured into the mold and crosslinked to form polymeric microneedles with chisel tips. Removal of these needles from the mold yielded the final master structure. Figure 2.2-(g) shows the tapered-cone microneedles. A chromium

layer was sputter-deposited and lithographically patterned on a glass substrate to form array of circular dots. Glass etchant was used to isotropically etch the glass substrate through the openings in the patterned chromium layer to create concave holes in the glass. Subsequently, SU-8 photoresist was cast onto the substrate. After soft-baking, the film was exposed from the bottom (through the glass substrate) using UV light. Finally, a master structure of tapered cone microneedles was fabricated in the developer for SU-8.

McAllister summarized various microneedles developed by Georgiatech (GIT) research group [12]. Various microfabrication techniques were developed for silicon, metal, glass and biodegradable polymer microneedle arrays in solid and hollow structure with tapered and beveled tips and feature sized from few microns to hundreds of microns in their research.

In addition, microneedles were fabricated in metal sheet by laser cutting or acid etching [14][15][16]. Figure 2.2-(h) shows the laser cut microneedles in stainless sheet. Each needle was 50 μm by 200 μm in width at the base, and tapered over a 1000 μm length to a sharp tip with 20° angle. The laser beam directly created the shape of the needles in the sheet. 3-D metal array was formed by bending the needles at 90^{o} out the plane of the sheet. Figure 2.2-(i) presents the metal microneedle arrays fabricated in titanium sheet via wet etch.

The blunt-tip microneedle, shown in Figure 2.2-(j), was fabricated by the etching stop before the mask totally undercut using isotropic wet etching techniques [42]. The heights of the projector ranged from 50 to 200 μm. The top of projectors consisted of a flat 100 ~ 900 μm^2 areas.

2.1.2 Drugs Loading Methods

Fabricated microneedles have been applied in delivery of Oligonucleotide, insulin, protein vaccine and DNA vaccine across the skin. The 20-merphosphorothioated oligodeoxynucleotides (ODNs) have been delivered across the skin of hairless guinea pigs at the rate of 8.08 + 0.60 $\mu g/cm^2/h$ with microneedle array as compared to 0.08+0.02 $\mu g/cm^2/h$ without the array [16]. This microneedle array is shown in Figure 2.2-(i). The approach of the ODN delivery is the "poke with patch", which uses microneedles to make holes, and then applies a transdermal patch to the skin surface. Delivery of the ODNs can occur by diffusion or possibly iontophoresis if an electric filed is applied. The approach of "poke with patch" has also been used to deliver insulin to diabetic hairless rats *in vivo* using the microneedles in Figure 2.2-(h) [14]. The microneedle array was inserted into skin using a high-velocity injector. A solution of insulin was then dispensed on top of the microneedle array. Blood glucose levels steadily decreased by as much as 80% after the solution left on the patch 4 h using the microneedles. The insulin solution placed on skin without microneedles did not have significant effects on the blood glucose level. The delivery of protein vaccine used the approach

of "coat and poke", where the needles were first coated with drug and then inserted into the skin. There are no drug reservoirs on the skin surface, and all drugs to be delivered were on the microneedle itself. The microneedles (Figure 2.2-(i)) were also be used to transport ovalbumin as a model protein antigen to the skin of hairless guinea pigs *in vivo* [15]. The antigen release from the microneedles surface was found to occur rapidly at the rate up to 20 μg/5s. The antibody responses using the microneedles were found to be up to 50-fold greater than using subcutaneous or intramuscular injection. The delivery of DNA vaccine was used the approach of "dip and scrape", where microneedles were first dipped into a drug solution and then scraped across the skin surface to leave behind drug within micro-abrasions created by the microneedles. Naked plasmid DNA was delivered to skin using the microneedle in Figure 2.2-(j) [42]. Expression of a luciferase report gene was increased up to 2800-fold using microneedles.

2.1.3 Insertion Mechanism

The mechanics of microneedles insertion into skin have not been developed very well. The mechanics are critically important to the practical applications. Davis *et al* addressed the issues for the microneedle insertion into skin [43][44]. The hollow microneedles in Figure 2.2-(d), were applied to measure the force required for insertion and the force reached fracture, which are related to the microneedle geometry and physical properties. Measured insertion force varied from 0.1 N to 0.3 N and had an approximately linear dependence on the area of the needle tip. It was assumed that the needle will insert into the skin when the energy delivered to

the skin by the needle exceeds the energy necessary to create a tear in the skin. With this assumption, a model was built up to predict the force required for insertion into skin based on the geometry. The microneedles were modeled as thin shells to predict the force reached for fracture. Fracture force increased significantly with wall thickness and trivially with wall angle, but was independent of tip radius in the model.

2.2 Microneedles in Local Delivery

The fabricated microneedles for local delivery can generally be categorized into in-plane and out-of plane microneedles. In-plane microneedles have been fabricated by thin-film deposition [45][46], diffusion of P+ etching stop layer [47][48] or micromolding [49]. In-plane needles with long straight shaft are quite fragile, especially those structures formed in thin-film deposition. In addition, In-plane needles have a wall thickness limitation and low density because of 2-D plane design and fabrication methods. Compared to in-plane microneedles, out-of-plane microneedles have more robust structural design in wall thickness and density. The Out-of-plane microneedles have been fabricated by metal deposition, inclined LIGA process and a variety of silicon etching technologies. Using the metal deposition technology, a taped hollow metallic microneedle array has been fabricated with SU-8 mold using backside exposure [50]. An inclined LIGA process has been developed to fabricate microneedle arrays using PMMA [51]. The fabrication processes for the metal and PMMA microneedles are complicated due to the limitation of micromachining methods in metal and polymer. Since the

microfabrication technology was initially developed based on silicon substrate, silicon microneedles dominated the development of out-of-plane microneedles. Gardeniers *et al* fabricated out-of-plane hollow microneedles with inclined structure which is defined by the slowest anisotropic etching of (111) plane in KOH wet etching [52]. With the development of dry etching technology in silicon, Stoeber *et al* used dots arrays as a mask to fabricate hollow needles, in which lumen was formed in deep reactive ion etching (DRIE) and outside profile of needle was generated by isotropic wet & dry etching of silicon [53]. Using the advanced inductively coupled plasma (ICP) etching technology, Griss *et al* developed side-opened microneedles, in which outside shape of needle was fabricated by anisotropic and isotropic dry etching process with mask of cross pattern and inner channel was defined by deep reactive ion etching at backside of silicon substrate [54].

2.2.1 Microfabrication Technology

Figure 2.3 presents the microneedles which have been reported for local delivery applications. Their fabrication processes are also summarized in Figure 2.3.

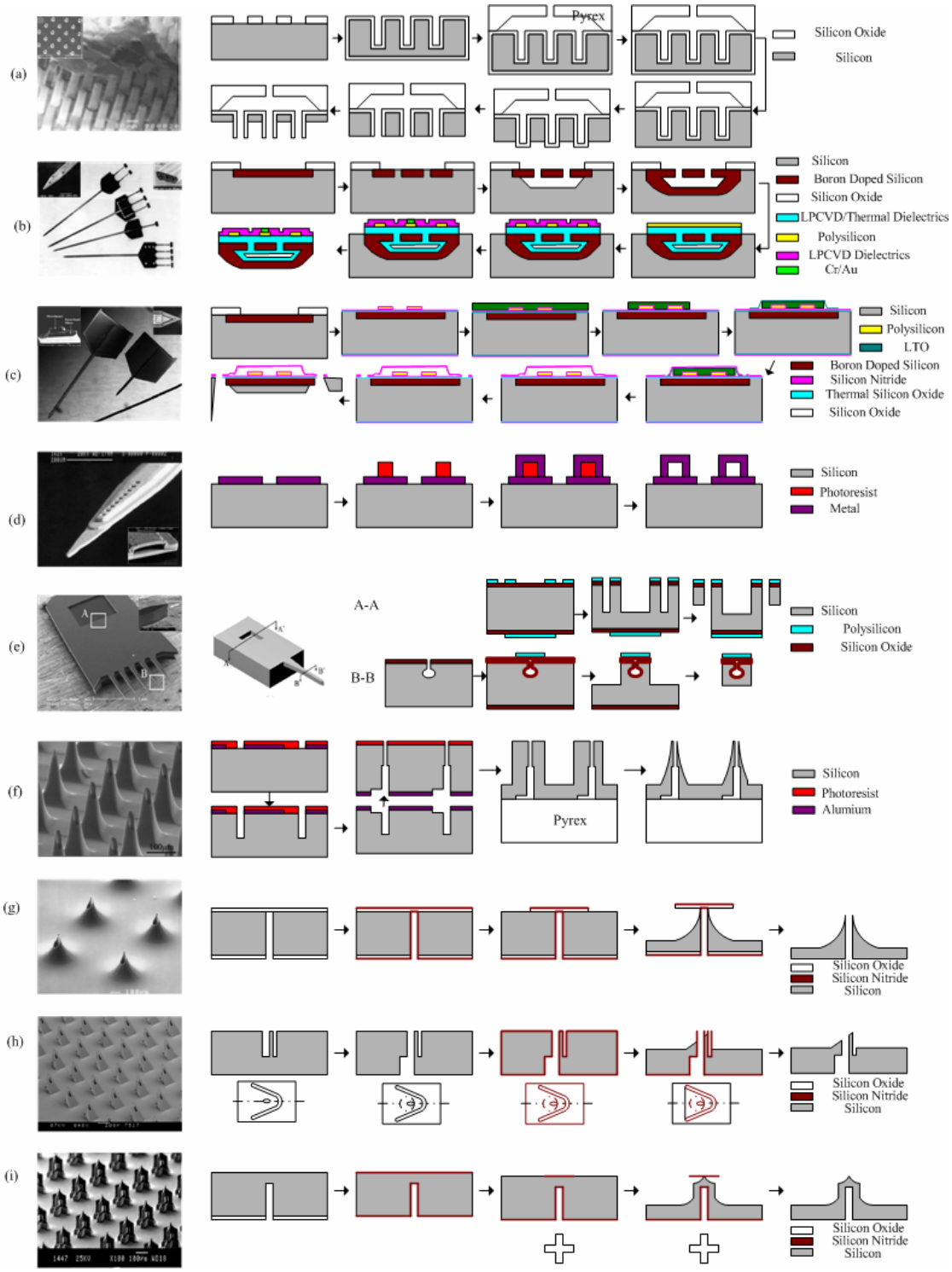

Figure 2.3 Micrographs of fabricated microneedles including microfabrication processes, in local delivery ((a) Ref.[55], (b) Ref. [48] (c) Ref.[47], (d) Ref.[56] , (e) Ref.[57] , (f) Ref.[58] ,(g) Ref.[53,59] (h) Ref.[52,60] (i) Ref.[54,61])

Chun *et al* fabricated the array of microcapillaries for injection of DNA to animal/plant cells [55]. Figure 2.3-(a) shows the array of hollow microacpillaries and its fabrication process. The deep reactive ion etching (DRIE) was conducted to etch microholes in to silicon using silicon dioxide as a mask. After the etched wafer was cleaned, a 1-2 μm oxidation layer was thermal growth onto the wafer. The wafer with microholes was then anodic bonded with a Pyrex glass wafer. The backside silicon was etched in TMAH solution until the tips of the microacpillaries appeared followed by the edges of the tips etched in BOE. Subsequently, the backside silicon was etched in TMAH again till the desired height of microneedle was achieved.

A multichannel silicon probe has been fabricated to deliver a precise amount of bioactive compounds into neural tissue while simultaneously recording electrical signals from neurons and electrically stimulating neurons *in vivo* [48]. Figure 2.3-(b) shows the fabricated neural probes with one to four microchannels for chemical delivery and the fabrication process of the microprobe. The fabrication of the microchannels started out with a shallow boron diffusion layer on the wafer surface. The pattern of chevron ribs was defined in the boron dope layer to etch intended channels. An anisotropic silicon etch (EDP) was used to undercut the chevron structure to form a flow tube. After undercutting the flow channels, deep boron diffusion was performed to define the probe shank. Sealing of the channel was accomplished using thermal oxidation, LPCVD deposited dielectrics, and an optional planarizing etch-back. After sealing the microchannels and planarizing the wafer surface, an LPCVD polysilicon conductor layer

was deposited and doped with phosphorus to achieve a sheet resistance. The polysilicon was then patterned using RIE, followed by LPCVD oxide/nitride/oxide triple layer passivation. The wafer was thinned from the backside using an isotropic wet etch, and individual devices were released in a final EDP etch.

Lin *et al* fabricated silicon-processed microneedles in combination with resistive heaters and IC-interface region using surface and bulk micromachining techniques [47]. The microneedles were used to reduce the insertion pain and tissue trauma of the hypodermic needles and deliver drugs in a controlled way. Figure 2.3- (c) shows the fabricated silicon microneedles and their fabrication process. The first step was to fabricate resistors for a thermally driven micropump. A (100)-oriented, lightly doped p-type wafer was selectively doped with boron that diffuses at heavily doped p-type region using thermally grown silicon oxide as a masking layer. After this layer was removed, another silicon oxide layer was thermally grown and a layer of LPCVD low-stress nitride was deposited. A LPCVD phosphorus-doped polycrystalline silicon layer was deposited, patterned, and etched. The polysilicon layer at the back side of the wafer was then etched away and a thin layer (150 nm) of LPCVD low-stress nitride was deposited to cover and protect the polysilicon resistors during EDP etching. Second step was to achieve the microchannel. A layer of 5 μm phosphorus-doped glass (PSG) was deposited, followed by deposition with a layer of 3 μm LTO. The microchannel was patterned and wet-etched in buffered HF. To form the edge of the microchannel, another layer of 1 μm LTO was deposited

by LPCVD, and then was patterned. Subsequently, the wafer was coated with 1μm thick LPCVD low-stress nitride and holes were defined using a plasma etcher. The sacrificial PSG and LTO inside the microchannel were etched away by concentrated HF. The etch-access holes were sealed by depositing a thick layer of LPCVD low-stress nitride. The final step was to release the microneedles. The separation EDP etch windows were defined by a plasma etcher with etching stop at the first silicon oxide layer. The back side of the wafer was patterned with a blank mask and without alignment in a stepper lithography system to open 1 cm by 1 cm etching areas of individual die to free the microneedles from the wafer backside. A timed EDP etch reduced the silicon wafer thickness to 120 μm. After a DI rinse, the wafer was immersed in BHF solution to etch exposed silicon oxide areas. Immersion in EDP in a timed etch reduces the 120 μm thickness down to 50 μm at the shank end of the microneedle. A combination of corner etching and etching from the crystal backside also removed the thicker non-doped single-crystal silicon for about 50 μm along the needle underside from the tip end.

Metal microhypodermic needles have been fabricated by surface micromachining techniques of metal deposition [56]. The metal microneedles and fabrication process is shown in Figure 2.3-(d). A metal system of adhesion layers and an electroplating seed layer was deposited by onto a silicon wafer by electron beam evaporation. The bottom shell of the microneedles was defined in a photoresist micromold using thick photoresist. Palladium layer was electroplated into the photoresist micromold. After electroplating the bottom shell, a thick photoresist was

spinning-coated and patterned to define the inner dimensions of the microneedle lumens. The photoresist served as a sacrificial layer, which was removed later in the fabrication process. A gold layer was then sputtered onto the sacrificial photoresist structures to serve as an electroplating seed layer for the top and side walls of the microneedles. To complete the electroplated microneedle structures, thick palladium layer was electroplated into the micromolds. The microneedles were released from the silicon substrate by etched away the first deposition metal layer. Finally, the thick sacrificial photoresist used to define the inner lumen dimensions was removed using a sequential rinse in acetone, isopropanol, and de-ionized water.

Paik *et al* have investigated in-plane single crystal silicon microneedles with buried microchannels [57]. In Figure 2.3-(e), fabrication processes for cross section A-A and B-B were illustrated, respectively. Microchannels were fabricated by the anisotropic dry etching, sidewall passivation with thermal oxide or LPCVD nitride film, isotropic dry etching with SF_6 plasma, and trench-refilling with LPCVD polysilicon film. After fabricating the buried microchannel, silicon dioxide films were deposited and patterned on both sides of the wafer. Two steps of deep silicon etching were used to define the reservoir depth and the microneedle shaft thickness on the front side of the wafer and to release the microneedles on the backside of the wafer.

An out-of-plane silicon microneedle array has been further fabricated for biological fluid extraction and in situ analysis, as shown in Figure 2.3-(f) [58]. A thin aluminum film was coated and patterned for channel and reservoir fabrication. A thick layer of photoresist was patterned open holes which are aligned to the previously defined channel structures. The patterned holes were etched into the silicon substrate by DRIE. After stripping the photoresist, the channels and reservoir patterns were etched into the silicon substrate, using the previously patterned aluminum coating as a mask. The needle boreholes were defined in thick photoresist with alignment to both the previously defined channel structures on the opposite side of the wafer. Removing the patterned photoresist from the wafer leaved a clean surface for anodic bonding of pre-drilled Pyrex 7740^{TM} glass lids. The microneedle shanks were then defined by first forming columns in the silicon using a dicing saw, followed by sharpening of the columns in an isotropic, silicon etchant composed of hydrofluoric, nitric and acetic acids.

With the development of deep silicon micromachining technology, various out-of-plane silicon hollow microneedles were fabricated [59][60][61]. Figure 2.3-(g), Figure 2.3-(h) and Figure 2.3-(j) show the three types of microneedles arrays fabricated in silicon wafers. DRIE was conducted to etch all of inner channels of those microneedles. Silicon oxide was used as mask in DRIE etching for the three microneedles. A silicon nitride layer was deposition to protect the inner channel wall during the etching of outside silicon to achieve the profiles of microneedles. With different mask designs, the different profiles of microneedles were achieved.

2.2.2 Fluid Analysis

The frictional losses have been researched in the multichannel neural probe presented in Figure 2.3-(b). Frictional losses in microchannel fluid are importance not only in proving the completeness of theory in conventional fluid dynamics but also for large amount of applications in microelectronics, micromechanics, and biomedicine. The frictional losses associated with fluid flowing in a pipe depend on many factors, including the average velocity of pipe flow, the pipe diameter, the fluid density, the fluid viscosity, and the average pipe wall roughness.. Silicon long microchannels were fabricated to determine the frictional losses of fluids flowing in these microchannels. The pressure drop across the channel was measured using a differential pressure sensor. Product of the Reynolds number and the Darcy friction factor as a function was measured. From the experimental results, the flow constant was determined for microchannel with a typically hydraulic diameter.

Stoeber *et al* found that the Bernoulli equation is a good model for liquid flow through microchannels such as the microneedle lumens [53][59]. It was assumed that the distance between needles was large enough so that fluid flowing through one needle should not influence the fluid dynamic behavior of fluid through a neighboring needle. Standard macroscopic values for a square edged inlet and for an exit that represent the inertial minor losses of piping systems were chosen to model the flow characteristics of the long microneedle lumen. The mean values of these measurements deviate by only 2% from the theoretical result

obtained from the modified Bernoulli equation. It had a good match between the experimental results and the theoretical values.

To determine the applied pressure at the inlet of the microneedle, the fluid flow was characterized for the surface micromachined metallic microneedles, which is shown in Figure 2.3-(d). Fluid flow through the microneedle lumen was assumed to be laminar. The friction loss due to the expansion or contraction of the flow channels was assumed to be negligible. It was found that the roughness factor has no appreciable effect on the friction factor for laminar flow unless it is so large that the measurement of the inner dimensions becomes uncertain. The cross section of the lumen was found to be closer to trapezoidal structure as opposed to a rectangular cross-section that was assumed in the calculation. Individual value of inlet pressure for exact flow rate was estimated.

2.2.3 Structure Fracture Analysis

The fracture of microneedles is highly related to the design of structure which determines the mechanical properties of the microneedles. The experimental tests of bending and buckling were normally carried out to find out the fracture forces for fabricated microneedles. Paik *et al* investigated the design variations of shafts for the in-plane microneedles during the in-plane buckling tests [58]. Their fabricated microneedles were shown in Figure 2.3-(e). The measured out-of- plane bending force was close to the FEM simulation results in their break tests.

The metallic microneedles (Figure 2.3-(d)) have been investigated to characterize the buckling force and penetration force [62]. The microneedles were modeled as a hollow beam. Compared to silicon microneedles, the electroplated metallic microneedles have less probability of failure associated with fracture, because of the robust material properties of metals. The load cell was interfaced with LabView to obtain real time data upon forcing the microneedle against the loading surface. The buckling force was measured by forcing the microneedle against a rigid metal surface, which was affixed to the load cell. The stress concentration due to redistribution of the force around the port was confirmed by the fact that the buckling point for all of the microneedles tested was at the port region. The axial strength of the microneedles was analyzed using ANSYS. A 3-D finite element model was created using a hollow shaft with lumen dimensions, wall thickness, and shaft length equivalent to those fabricated microneedles. The model was used to study the effect of a rectangular port on the stress distribution/failure mode of the microneedle shaft. The failure mode observed in this model was similar to that observed during the experiments.

2.3 Discussion

Microfabrication technologies for microneedles were reviewed in this chapter. Most of the in-plane microneedles were fabricated by the surface micromachining technologies. The bulk micromachining technologies were dominantly applied for the out-of-plane microneedles. The lumen of microneedle was commonly obtained by etching through the wafer using DRIE. The

silicon is still the popular material for microneedles because of mature micromachining technology for silicon. The group in GeorgiaTech (GIT) contributed tremendously for the microneedle in transdermal drug delivery. Besides the advanced microfabrication methods for metal and polymer microneedles, the insertion mechanics and *in vitro* delivery testing were investigated to determine the biological application of microneedles. The current research focused on developing the biodegradable microneedles to improve the biocompatibility of microdevices in clinical application. Most of the research on microneedle for transdermal drug delivery solely focused on the solid microneedle array. The main problem in applied the microneedle to deliver drugs consists of broken microneedle tips during insertion into the skin. The microneedle developed in this thesis has a biodegradable tip which will be readily absorbed by the body. The biodegradable tip also will reduce the risk of granulomas or infection. The design also has advantage in easily enabling mass production of microneedles compared with using the polymer material for fabrication. It is the first proposal of using porous silicon in microneedle fabrication to overcome the foreign allergy in microneedle clinical application. Furthermore, it provides the idea to fabricate microneedle with combination of two different materials. It guarantees the microneedle with enough strength with improvement of biocompatibility. In Chapter 3, the silicon microneedle with biodegradable porous tips was proposed to reduce the possibility of the irritation caused by the broken issues of microneedle during the insertion. In Chapter 4, the analytical model was established to study the critical loadings of microneedles in insertion.

On the other hand, the microneedles with lumens were developed for injection of a precise controlled dose to prescribed locations. Microsystems consisting of in-plane microneedles and integrated circuits have been well developed not only in the fabrication but also in the applications. Compared with the in-plane microneedles, the out-of-plane microneedles have advantages in high efficiency inject DNA/RNA into assembled cells or embryos. However, microsystems based out-of-plane microneedles have not been well studied due to the limitation of microfabrication process. The prototype of microsystem in this report is proposed under consideration of design of controlled flow to determine the dimension of microneedle. The structural enhancement is fabricated based on the novel mask and process design. In Chapter 5, a microsystem consisting of out-of-plane hollow microneedles and glass actuation components was presented. The designs of flow and actuation mechanism were investigated to determine the dimension and actuation conditions of the microsystem.

Chapter 3 Microneedle Array with Biodegradable Tips for Transdermal Delivery

3.1 Design of Microneedle Array with Porous Tips

Microneedles were designed to puncture the skin by creating micro-pores across the skin to increase skin permeability for delivery of the protein/DNA based drugs. Figure 3.1 shows the schematic of a microneedle array insertion into skin [63]. The microneedles were used to pierce the stratum corneum (SC) layer of skin, creating micro-pores on the first skin layer. The microneedles do not penetrate into the dermis layer and thus do not reach the nerve endings, reducing the sensation of pain in transdermal drugs delivery using microneedles.

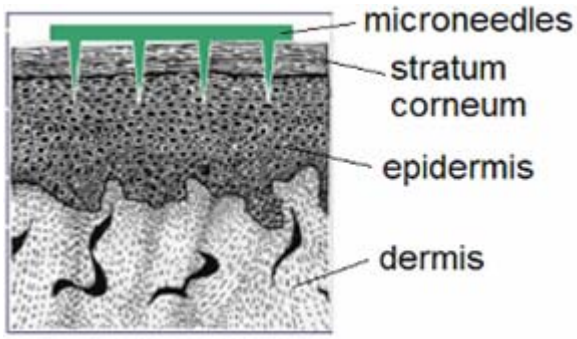

Figure 3.1 Microneedles in transdermal drug delivery

In order to fulfill the functions necessary for transdermal drug delivery, microneedles must meet the following requirements:

- Sharpness for penetrating the skin.
- Strength against fracture, bending and buckling.

- Biocompatibility of microneedle material.

It was found that the interface of the needle sharp tip would be imperfect after insertion test. The brittle tip was broken in the insertion test. Figure 3.2 shows the SEM picture of a broken tip after an insertion experiment. The damage occurred at the tip at a height of ~15 μm. The failure of sharp tips is likely due to the force of insertion exceeding the tensile strength of silicon. The friction and deflection during insertion could also be additional explanations for the fracture of tips. The scraps of broken microneedles may cause inflammations because they might elicit a foreign body response. When microneedle tips would break and become lodged within the skin, they are likely to become encapsulated by poly-morphonuclear and mononuclear leukocytes [64]. The application of biodegradable material in microneedle fabrication would be a potential solution to decrease the possibility of the irritation.

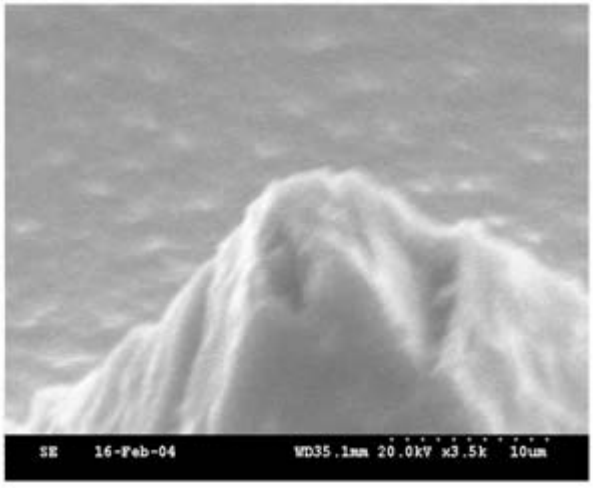

Figure 3.2 SEM picture of damaged microneedle tip after insertion

So far, microneedles with various designs, as reviewed in Chapter 2, have been fabricated with limited consideration of material biocompatibility, which is critical for clinical applications. In the transdermal drug delivery, the drug loading methods in microneedle application were limited to coating the surface and using a patch in the previous studies. The design of a microneedle with biodegradable tip would improve the biocompatibility of microneedles the drug delivery. The porous silicon, known as nano-structured silicon, is widely used in the biological areas because of its biocompatible, bioactive and biodegradable nature [65]. Angelescu *et al* found that porous silicon structures are appropriate for cultivating adherent cells *in vivo* and without noticeable toxicity for biological applications [66]. There were already some biological applications of porous silicon, such as biocapsules and filters in BioMEMS for drug delivery [67][68][69]. Porous silicon also has many possible uses for orthopaedic medical device, such as a bone graft substitute, scaffolding for bone repair and regeneration, molded orthopaedic implants, and paste for spine fusion. The porous silicon material could be mechanical stable for insertion into skin in the transdermal drug delivery. The microneedles with biodegradable porous tips have several advantages if they would break off and remain in the skin. The porous structure provides an alternative approach for drug loading as well.

Porous silicon exhibits a high degree of biocompatibility. It degrades to silicic acid, which causes no harm to the body.[70] Silicic acid is a general name for a family of chemical compounds of silicon, hydrogen, and oxygen, with the general formula $[SiO_x(OH)_{4-2x}]_n$.

Moreover, silicic acid is reputed to be the most natural form of element in the evieroment and it readily to removed by kidneys. Therefore, the very positive attibution of porous silicon is the non toxic waste product from the degradation of porous silicon into monomeric silicic acid. Porous silicon with varying porosity is altered in between bio-inert, bioactive and resorbable.[71] The in vitro study was conducted to test the activites of porous silicon sample.[72] The simulated body fluid containing ion concentration , which is similar to the human blood, was used to test the resistaned period of time for the porous silicon exposed to the fluids. It was found that the high porosity layer were completely removed within a day. [73] In the in vitro studies of interaction of cells with porous silicon, the porous silicon has been found to be suitable for cell generation.[74] It also has been found that B50 rat hippocampal cells have clear prefernce for adhesion to porous silicon over untreated surface. [75] Beside the potential applications of porous silicon in cell culturing, the porous silicon has also been investigated in used as framwork for the growth of bone.[76] In the application in drug delivey, , a particular drug can be encapusulated by the porous silicon layer by capillary action because of the porous form of structure. Porous silicon has the advantage in adiministation drugs through various approaches, such as the tablets for oral delivery, patches for delivery througy skin, and micropaticles for injection.

Biodegradable material appears to be on threshold of widespread clinical application. Compared with biodegradable polymers, the key features of porous silicon are that it can be

micromachined, and it is a semiconductor. The micromachinability enables precise macrostructure can be fabricated in porous silicon. The properties of semiconductor for porous silicon contribute to be easily integrated with a microsystem including sensors, actuators and circuits. Furthermore, the porous silicon has potential in a wide variety of applications in different clinical areas due to the controllable porosity.

A prototype of the microneedles with biodegradable tips is shown in Figure 3.3. In order to facilitate their ability for insertion into the skin, the sharp tips were designed to minimize the insertion force needed. According to insertion experiments established to test insertion force, the insertion force dramatically decreases with the decreasing interfaced area. Moreover, the microneedles were designed to puncture to the correct skin depth for transdermal drug delivery. The microneedles must pierce the stratum corneum layer (10-20 μm) and arrive at the epidermis layer (50-100 μm) without access to the dermis layer. Considering that the skin distorts under an applied force applied, the length of the needles was designed to greater than 100 μm and less than 150 μm, as shown in Figure 3.3. The height of the porous silicon tip was designed to be ~ 10-20 μm with the consideration of the limitation of the fabrication. In the design, the radius of tip is less than 1μm and the base width dimension is 100 μm. The tip angle is less than 10 ^{o}. The center-to-center distance between the two single needles is 150 μm. One microneedle array includes 20 by 20 needles.

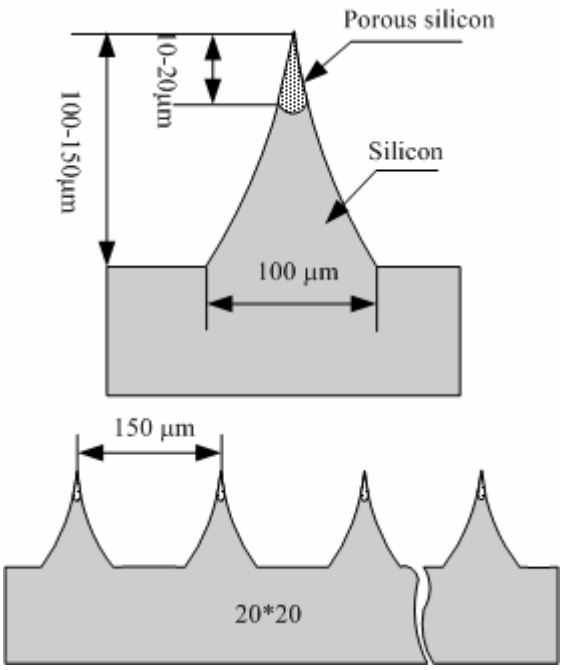

Figure 3.3 Schematic of microneedle array with porous tips

3.2 Experimental Methods

The overall porous tip needle fabrication process is shown in Figure 3.4. Four-inch p-type (100) silicon wafers with resistivity ranging from 1 to 10 Ω·cm, and thickness of 450 μm were used in this study. The fabrication procedure for the pyramidal needle structure is illustrated in Figure 3.4 (a)-(d). The 0.7 μm thermal oxidation layer was grown on the wafers (Figure 3.4 (a)) in a furnace at 1050 ^{o}C. After photolithography, a patterned photoresist (AZ 7220, 1.5 μm) was used as a sacrifice layer. The exposed silicon dioxide was etched away in RIE with CF_4/O_2 gases and formed arrays of squares from 80 × 80 μm^2 to 120 × 120 μm^2 (Figure 3.4 (b)). After removing the residual photoresist, the silicon dioxide square arrays were used as the mask to isotropically etch the silicon using SF_6/O_2 gases in a STS Inductive Coupled Plasma (ICP) etch tool. Etching

was performed until the oxide mask fell off due to the under etching, which generated the pyramidal needle structure (Figure 3.4 (c)). After removing the residual silicon oxide (Figure 3.4 (d)), a 500 nm thick silicon nitride layer was deposited onto the fabricated microneedle surface over 2.5 hours by low pressure chemical vapor deposition (LPCVD) at 530 ^{o}C (Figure 3.4 (e)). Photoresist (AZ9260) was spin-coated twice onto the pyramidal needle structure at a spin speed 1500 rmp (Figure 3.4 (f)), followed by baking of the sample for 15 minutes at 120 ^{o}C. Due to the effect of reflowing, the photoresist covering the tips of the needle became thinner. The photoresist on the tip of the needle was further cleaned by reactive ion etching (RIE) using O_2 (Figure 3.4 (g)). Etching was conducted using 200 W of power and an oxygen gas flow rate of 10 sccm for 15 minutes. After etching of the photoresist, the RIE process was carried out to remove the unprotected silicon nitride from the tip of the needle and backside of the wafer using CF_4/O_2 gas. This process was conducted using RF power of 350 W and CF_4:O_2 flow rates of 8 sccm: 1.4 sccm for 5 minutes. After removal of the photoresist (Figure 3.4 (h)), a gold layer was deposited onto the backside for use as a conductive layer by E-beam evaporator (Figure 3.4 (i)). The remaining silicon nitride layer was used as a protective layer in the subsequent electrochemical porous tip etching, resulting in the final porous tip structure (Figure 3.4 (j)).

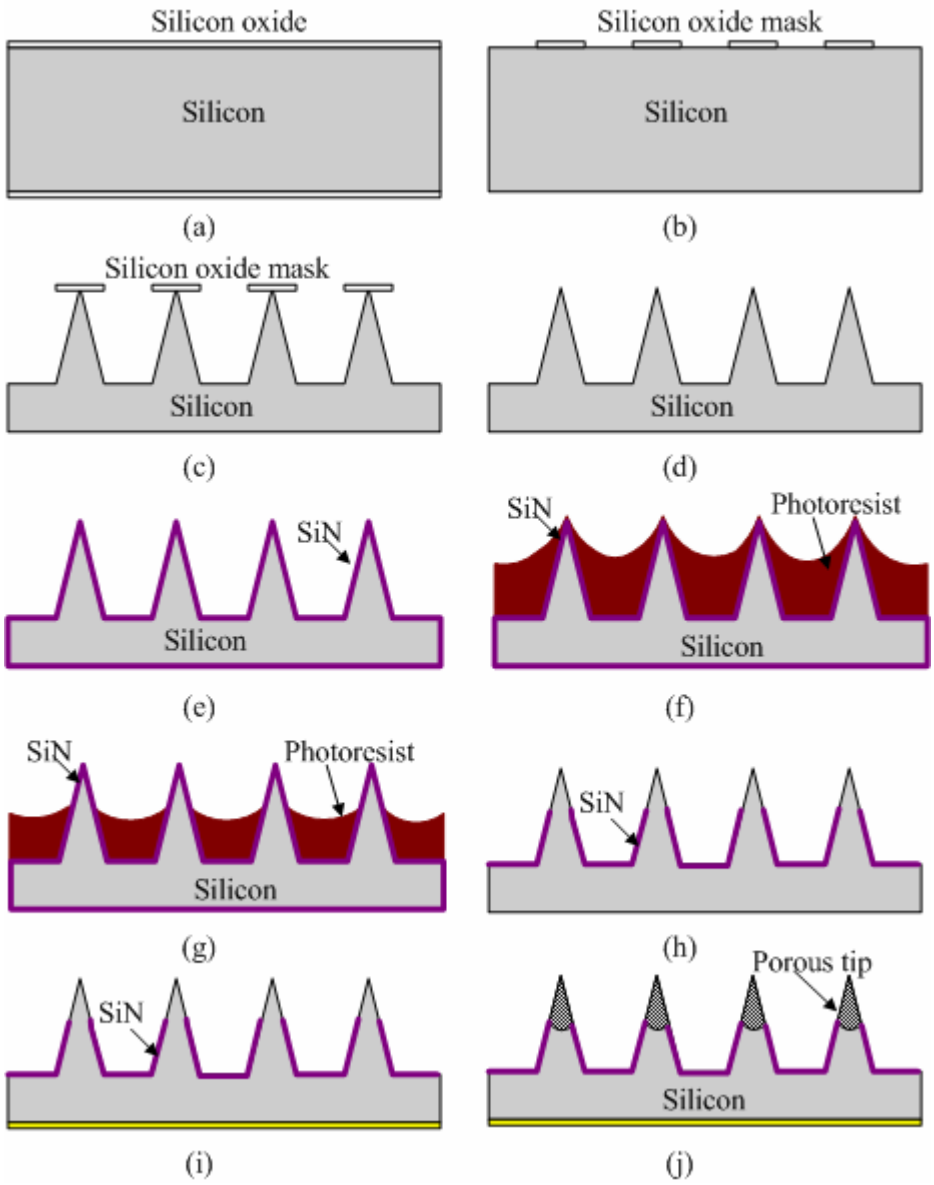

Figure 3.4 Schematic of the fabrication process used in making the needles with porous tips. The process consists of (a) thermal growth of silicon oxide, (b) patterning the silicon oxide mask, (c) pyramid needle structure etching by inductive coupled plasma etching using STS equipment, (d) removal of residual silicon oxide (e) deposition of LPCVD silicon nitride layer, (f) photoresist coating (g) photoresist reflowing and O2 plasma thinning, (h) the tip part and backside silicon nitride etching in RIE and photoresist removal, (i) backside gold layer deposition, and (j) electrochemical etching process to form the porous silicon tips.

3.2.1 Isotropic Etching in Inductively Coupled Plasma (ICP)

The pyramidal structure of microneedle was fabricated by the isotropic plasma etching in inductively coupled plasma (ICP) etcher. [77] The ICP high density plasma etcher is well known to carry out deep reactive ion etching (DRIE), implemented with BOSCH process, which utilizes an etching cycle using SF_6 gas and then switches to a sidewall passivation cycle using C_4F_8 gas [78]. If the passivation cycle is not performed in the silicon etching, isotropic profile, as shown in Figure 3.5, will be obtained in the etching cycle using SF_6 gas. The silicon is primarily etched by the atomic fluorine radicals assisted by ion bombardment. The reaction in the etch cycle is represented in E-3.1 and E-3.2:

SF_6 dissociates:

$$SF_6 + e^- \rightarrow S_xF_y + S_xF_y^{\bullet} + F^{\bullet} + e^- \qquad \text{E- 3.1}$$

Ion-assisted chemical etching:

$$Si + nF^{\bullet} \rightarrow SiF_n \qquad \text{E- 3.2}$$

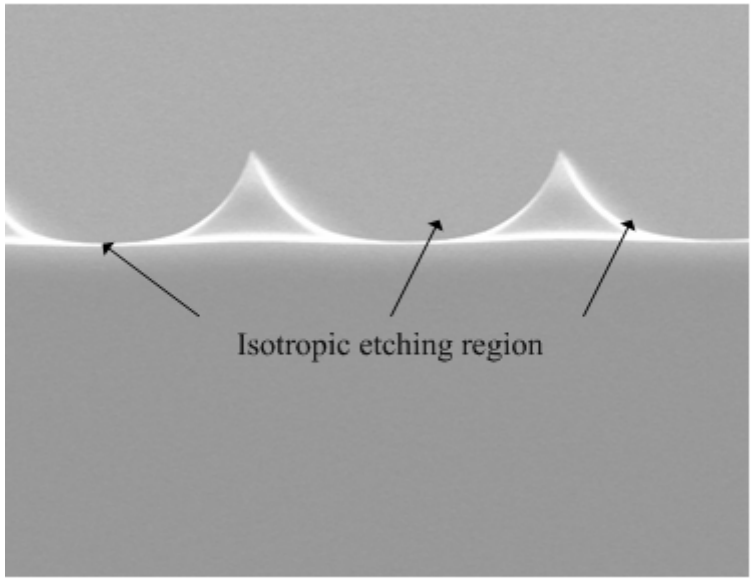

Figure 3.5 Isotropic profile formed in ICP etching cycles

The etched profile could be controlled by adjusting the etching parameters in ICP tools. Figure 3.6 shows the slope achieved at low pressure using SF6 etching. The findings were later used to fabricate microneedles with different slopes by controlling the etching parameters.

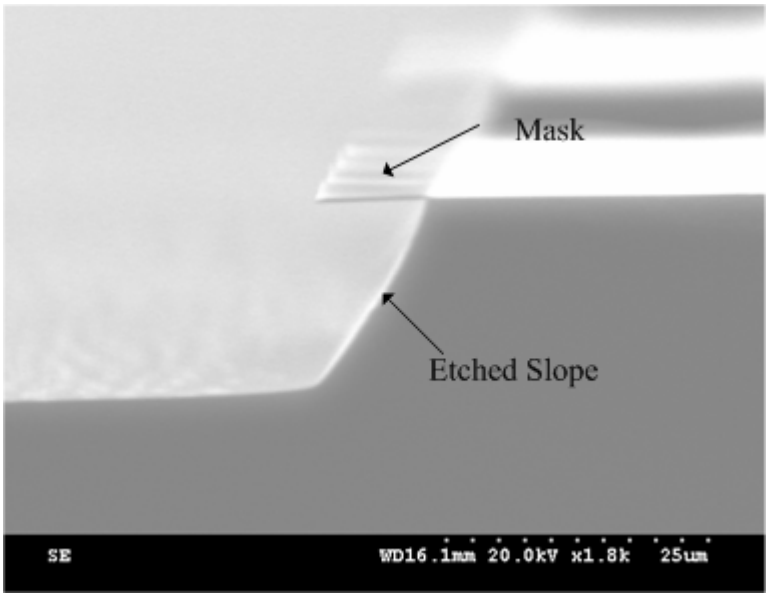

Figure 3.6 SEM picture of etched slope

The isotropic etching behaviors in inductively coupled plasma (ICP) etching tool were investigated to fabricate desired profiles of the microneedles. The obtained results were used in the fabrication of microneedles with certain process parameters. In the experiment, the etch tool was operated only using SF_6 gas without passivation cycle. Figure 3.7 shows the cross section of an ICP etch tool. There are four major process parameters in the etching process: gas flow rate, platen power, coil power, and automatic pressure control valve (APV) position. Because of the complicate ICP etching mechanisms, the effects of process variables on etching results are nonlinear and interdependent. Several statistics methods have been used in plasma process characterization due to the complicated influences of etching variables on etching results [79][80]. The design of experiments (DOE) technique was used in the process characterization to explore the influence of these correlated and interrelated variables on etching results. The effects of multiple variables on output results (responses), including pressure, vertical etching, lateral etching , the ratio of vertical etching to lateral etching, and photoresist etching rate, were investigated to characterize and optimize the etching parameters.

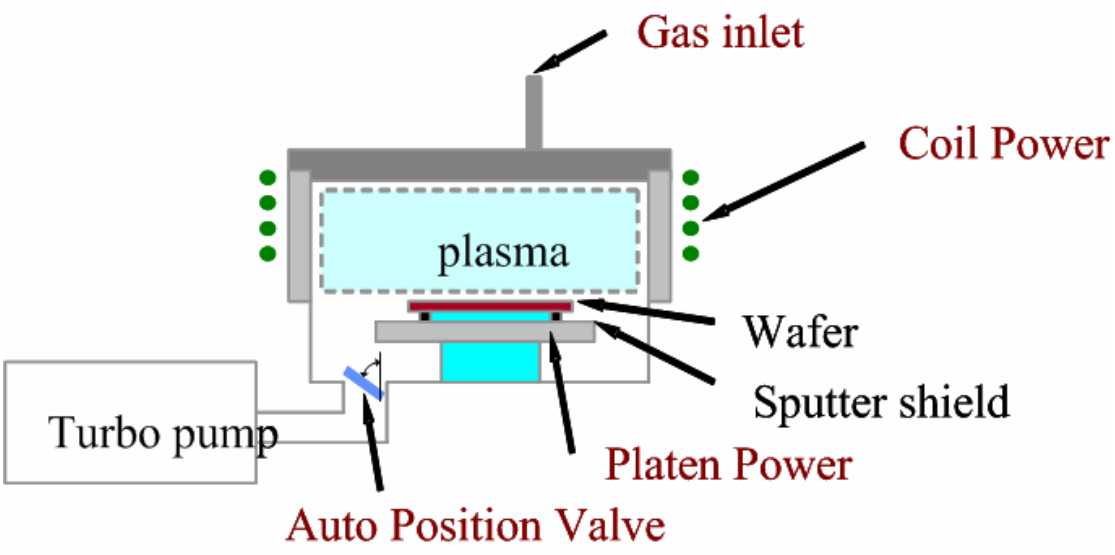

Figure 3.7 Cross-section of ICP etch tool

4-inch p-type silicon wafers, 450-500 μm thick and (100) orientation were used in the ICP parameters characterization experiments. The photoresist (AZ9260) was coated at 4000 rmp (thickness ~3.5 μm). Samples were exposed using a mask aligner, developed in developer (AZ400) and baked at 100 ^{o}C before ICP etching was carried out. The mask layout consisted of patterns with square arrays and dots arrays that exposed 12% of the total wafer surface. The size of the patterns was 80 μm in dimension with a center distance 150 μm. The etching time in trials was 3 minutes. The characterization work was performed using ICP etching tool from Surface Technology Systems (STS), which was used as an isotropic high-density plasma etcher for the passivation cycle was excluded. The four most important variables studied in this part of the experiment were: SF_6 flow rate, automatic pressure control valve (APV) position, platen power and coil power. The ranges explored are presented in Table 3.1. The selected ranges of mass flow and power were based on previous observations made by Ayon *et al* [81][82]. A

surface profiler was used to measure the depth of etched patterns. The etched photoresist thickness was calculated by measurement of depths before etching, after etching, and after photoresist removing for each sample. A microscope integrated with a video camera was used to check topside images of etched samples. Additionally, a scanning electron microscope (SEM) was used to obtain the etched structures under various etching recipes. The commercial software Minitab® was used to create and analyze a matrix of 20 runs of process screening using DOE method. For the 4 factors full factorial design, 16 runs were carried out for the characterization. The experimental design with 4 additional runs was used to verify the etching results. In total, 20 runs were executed to fit the quadratic model.

Table 3.1 Range of explored variables for isotropic etching

Variable	Minimum	Maximum
SF_6 flow rate (sccm)	30	150
APV position (^{o})	30	75
Platen power (W)	1	29
Coil power (W)	300	900

The measured vertical etching depth, lateral etching length, and photoresist etching rate were characterized. The corresponding responses were generated using Minitab®. The ratio of vertical etching depth to lateral etching length (V/L ratio) was calculated. This limits the finial length of the fabricated needle. The main dimension of microneedle fabrication used in this experiment was plotted in Figure 3.8, showing the relevant variables of microneedle profile. V

is Vertical etching depth and L is Lateral etching length. Photoresist etching rate was obtained by the thickness difference of photoresist between before and after etching divided by etching time. In DOE, the effect of a factor, which is the change in response produced by a change in the level of the factor, weights the influence of a factor to responses. The significance of factors in the full factorial experiment can be constructed based on a normal probability plot of the effect estimate. By the factorial analysis in Minitab®, the effects of variables for various responses, such as pressure, vertical etching, lateral etching, ratio of vertical etching to lateral etching and photoresist etching rates, were generated to analyze the process parameters.

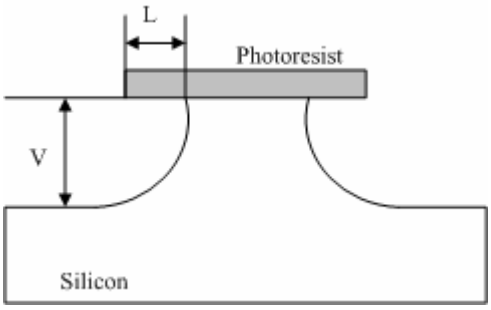

Figure 3.8 The dimension used in microneedle fabrication

The measured data from the experiments are given in Table 3.2. The measured vertical etching depths, lateral etching lengths and photoresist etching rates are presented in the table. The calculated ratio of vertical etching depth to lateral etching length (V/L ratio) and the tip angles were also included in Table 3.2.

Table 3.2 The experimental design for isotropic etching in ICP

Run	A	B	C	D	Pressure	Vertical etching	Lateral Etching	Ratio of V/L	Tip Angle	Photoresist etching rate
	SF_6	APV	Platen Power	Coil Power	(mT)	(μm)	(μm)		2acrtan(L/V)	(nm/min)
1	1	1	1	1	36	22.8896	13.5000	1.69553	1.07	189.75
2	1	1	-1	-1	33	8.1040	5.0000	1.6208	1.11	35.68333
3	1	1	1	-1	33	8.9532	5.0000	1.79064	1.02	98.8
4	-1	1	1	1	13	12.4168	6.6667	1.86252	0.99	285.7667
5	0	0	0	0	14	14.9928	9.6667	1.55098	1.15	190.5333
6	-1	-1	1	1	5	5.3073	2.1667	2.44952	0.78	188
7	1	1	-1	1	50	30.9308	16.3333	1.893723	0.97	82.43333
8	-1	-1	1	-1	4.9	5.9886	2.16667	2.763969	0.69	246.95
9	0	0	0	0	14	14.2574	8.8333	1.61404	1.11	195.7667
10	-1	1	1	-1	11	7.9248	5.0000	1.58496	1.13	151.5333
11	-1	-1	-1	1	5.2	7.6814	4.1667	1.843535	0.99	102.9167
12	0	0	0	0	13	13.795	9.0000	1.532772	1.16	196.55
13	1	-1	1	-1	12	9.3393	5.3333	1.75112	1.04	164.6833
14	-1	1	-1	1	14	12.8522	7.16667	1.793337	1.02	33.81667
15	-1	-1	-1	-1	4.5	5.9427	3.3333	1.78281	1.02	92.18333
16	-1	1	-1	-1	11	7.7414	4.5000	1.720322	1.05	103.5667
17	1	-1	-1	-1	12	8.6088	5.16667	1.66621	1.08	57.81667
18	1	-1	-1	1	16	17.8376	11.3333	1.573906	1.13	43.36667
19	1	-1	1	1	16	17.1832	10.6667	1.61092	1.11	306.6
20	0	0	0	0	13	13.5531	8.5000	1.594482	1.12	184.8167

3.2.1.1 Pressure

In the STS ICP etching tool, the chamber pressure is normally controlled by varying the position of APV or changing the flow rate at the fixed APV position. Higher pressures correspond to higher values of SF_6 flow rate and APC valve positions in degrees (90^oclose; 0^o open), as shown in Table 3.2. Figure 3.9 shows the effects of the four variables on chamber pressure in ICP etcher. The effects of SF_6 flow rate (A), APV position (B) and coil power (D), and the interaction of AB which are marked using squares are significant. SF_6 flow rate (A) and APV position (B) dominate the positive influence on the pressure, because these two variables determine the amount of gas in chamber. Therefore, the higher values of SF_6 flow rate in standard cubic centimeter per minute (sccm) and APV position in degrees correspond to higher pressures in reactor. The coil power (D) also has a positive effect on pressure because the movement of molecules is more active in higher energy level under higher coil power. In addition, the value of effect of platen power (C) is negative, as shown in Figure 3.9. This negative standard effect indicates that the pressure deceases with increasing platen power. This result can be explained by the electrical attraction of the gases by platen power in reactor. The higher platen power causes more ions in plasma to move towards the sample substrate, resulting in lower gas density and chamber pressure. The chamber pressure also increases with higher coil power. In ICP, power is transferred from the electric fields to the plasma electrons near the surface by collisional dissipation and by collisionless heating process [83]. Therefore,

higher coil power may cause higher chamber temperature, which results in higher pressure. The dependence of chamber pressure on SF_6 flow and APV position is clearly illustrated in the surface plot chat (Figure 3.10). The pressure has the highest value (~35mT) at the greatest SF_6 flow and the highest APV position.

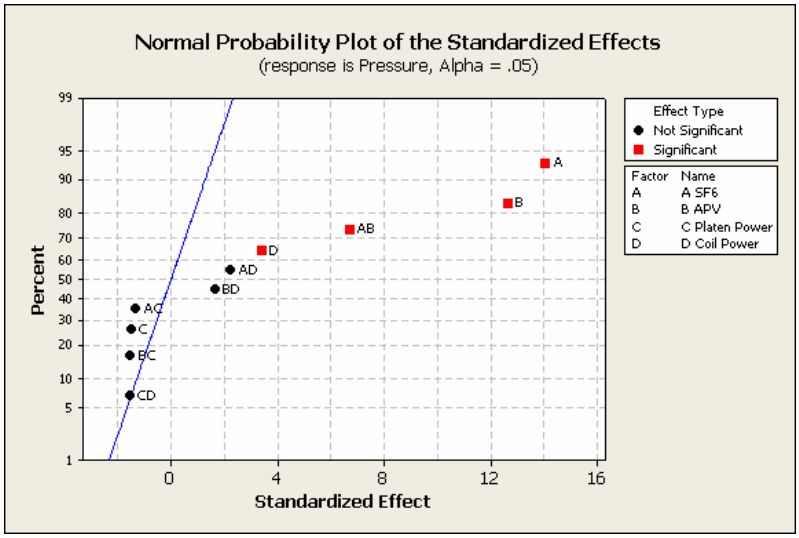

Figure 3.9 Normal probability plot of effects on pressure

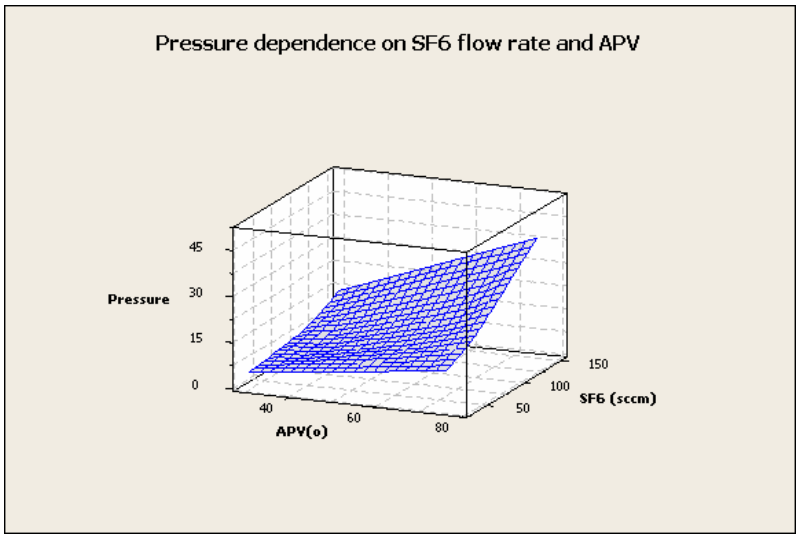

Figure 3.10 Pressure (mTorr) dependence on SF_6 flow rate (sccm) and APV position in degree

3.2.1.2 Vertical etching depth (V)

Figure 3.11 shows the response of the vertical etching depth to the four variables. The weight value of coil power (D) indicates that the coil power has the most significant effect on vertical etching rate. The coil power is the dominant variable because the ion flux reaching the etched silicon surface is determined by the power. The vertical etching rate also increased at higher SF_6 flow rate because a higher setting of this variable helps to remove the byproduct in silicon etching. In addition, increased vertical etching depth was found at higher settings of the APV position, because the residence time of reactive gases is longer at higher pressure. The residence time is proportional to PV/f, where P is the pressure, V is the chamber volume and f is the gas flow rate. On the other hand, platen power has a negative effect on the vertical etching depth. The negative value (-1.3), as shown in Figure 3.11, indicates that the vertical etching rate decreases slightly at higher setting of platen power. This may account for greater energy loss in higher ion collision at the increased ion bombardment under higher platen power. The vertical etching depth dependence on coil power and SF_6 flow rate is illustrated in Figure 3.12. The influence of coil power and SF_6 flow on vertical etching is increasing with the increasing values of coil power and SF_6 flow, respectively. The surface plot of vertical etching dependence on coil power and SF_6 flow matched the effect of co-effect AD on vertical etching. The interaction of AD is the third positive effect on vertical etching as shown in Figure 3.11.

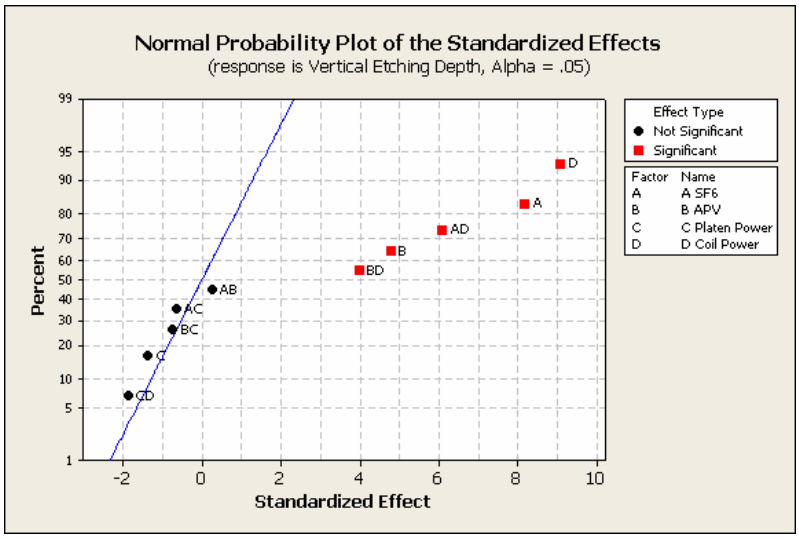

Figure 3.11 Normal probability plot of effects on vertical etching depth

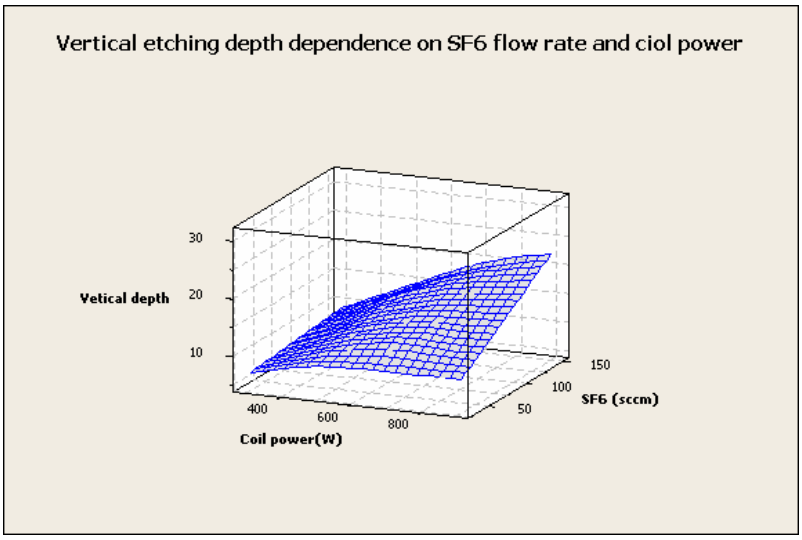

Figure 3.12 Vertical etching depth (μm) dependence on SF_6 flow rate (sccm) and coil power (W)

3.2.1.3 Lateral etching length (L)

Figure 3.13 shows the effects of the variables on the lateral etching length. These effects distributions are similar to the distribution of effects on vertical etching depth because the isotropic profile is obtained using SF_6 gas in the etching. The SF_6 flow rate (A) has the most

significant effect on the lateral etching rate. Larger SF_6 flow rate not only helps the removal of the etching byproducts, but also reduces the concentration of products that would redeposit. Figure 3.13 also illustrates that lateral etching increases with respect to vertical etching when the ion fluxes increase. Compared to the value of vertical etching rate, a lower lateral etching rate was found in the characterization. The variably exposed area of the surface during the etching process may account for the difference between vertical etching and lateral etching. The exposed area in vertical etching is constant; but in lateral etching, the exposed area increases along with the vertical etching depth. The increase of expose area may reduce the lateral etching rate. Figure 3.14 shows the dependence of the lateral etching length on the SF_6 flow and coil power. Compared to the curvature of surface plot for vertical etching depth dependence on the two variables, the curvature of surface plot for lateral etching length is larger. The larger curvature indicates that the interaction AD have more significant influence on lateral etching length.

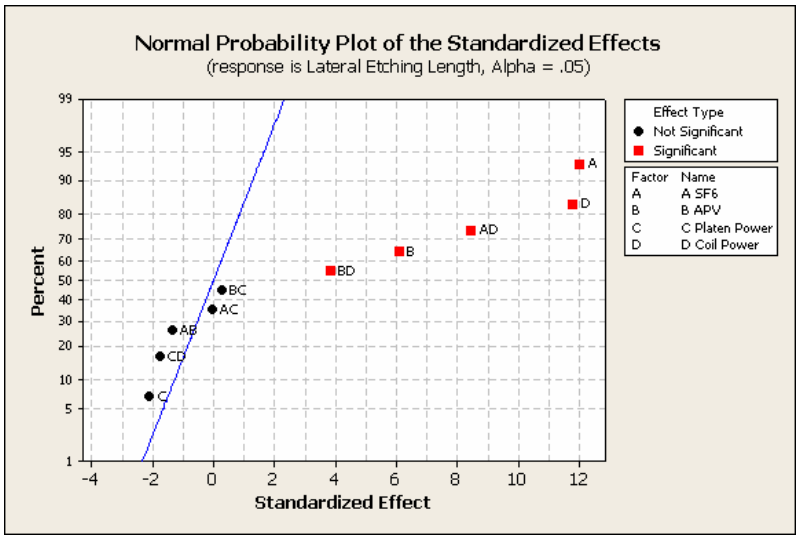

Figure 3.13 Normal probability plot of effects on lateral etching length

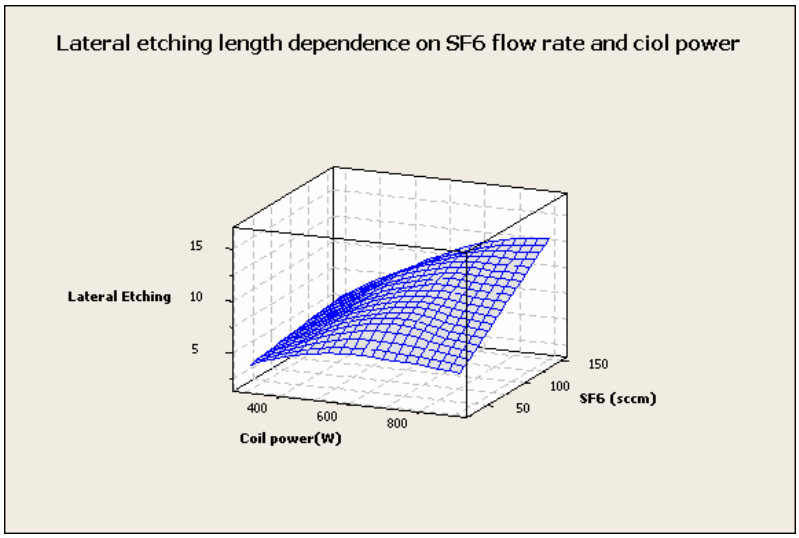

Figure 3.14 Lateral etching length (μm) dependence on SF_6 flow rate (sccm) and coil power (W)

3.2.1.4 Ratio of vertical etching to lateral etching (V/L ratio)

The response of the V/L ratio plays an important role in the height of needle. A longer needle would be fabricated under higher of V/L ratio values. The calculated response on etching conditions is shown in Figure 3.15, which shows that larger values of the V/L ratio would be obtained at higher platen power as well as lower SF_6 flow rates. However, the etch rates will be traded off for the larger values of V/L ratio. The positive influence of platen power (C) on the V/L ratio suggests that the negative effect of platen power on vertical etching is less than the negative effect of platen power on lateral etching. In addition, the interaction AB has the most positive effect on the V/L ratio while the interaction BC has the second-most negative effect on the response as illustrated in Figure 3.15. The V/L ratio dependence on platen power and SF_6 flow rate is presented in Figure 3.16. The positive effect of variable C (platen power) is

weakened by the variable A (SF_6 flow), as illustrated in the surface plot of V/L ratio dependence on SF_6 flow and platen power (Figure 3.16).

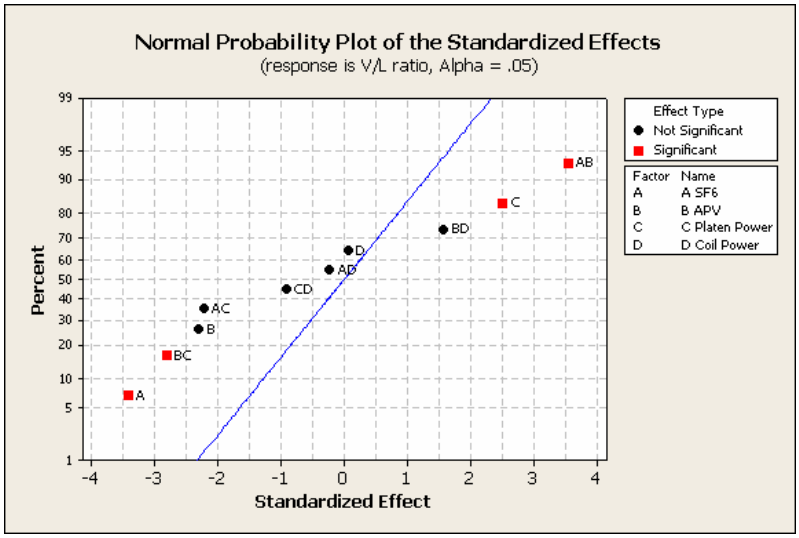

Figure 3.15 Normal probability plot of effects on V/L ratio

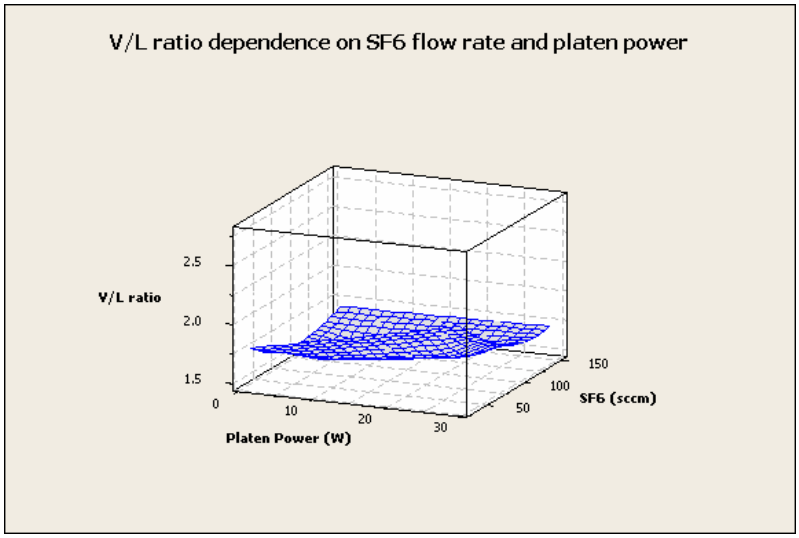

Figure 3.16 V/L ratio dependence on SF_6 flow rate (sccm) and platen power (W)

3.2.1.5 Photoresist etching rate

Figure 3.17 shows the normal probability plot of the effects on the photoresist removal rate. Apparently, it is the effect of platen power that is the most significant, as it falls far from the line passing through the other points. Platen power is the dominant variable because it governs the ion bombardment energy. Therefore, higher platen powers correspond to larger photoresist sputtering rates. Lower photoresist etching rates were obtained at higher SF_6 flow rates and higher APV position settings due to influence of pressure. Higher operating pressures led to lower ion energy that causes lower photoresist etching rates. Figure 3.17 also illustrates that larger SF_6 flow rate and higher APV position contribute to less photoresist etching since these two standardized effects have negative value factors. This is because higher chamber pressure lowers the ion energy. At higher SF_6 flow rate and APV position, higher pressure is achieved, as illustrated in Figure 3.10 presented in the paragraph of parameter effects on pressure.

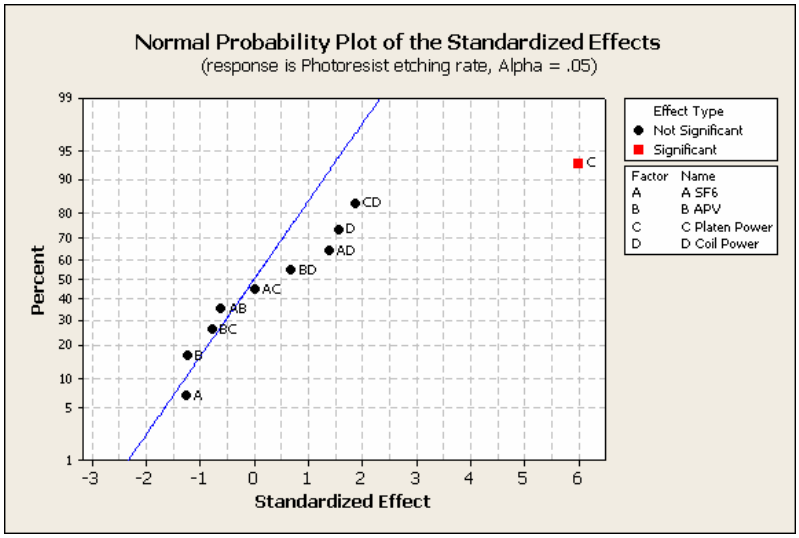

Figure 3.17 Normal probability plot of effects on photoresist etching rate

3.2.2 Photoresist Reflow Process

The reflow of photoresist method was developed to expose the top of the silicon needle after a silicon nitride layer was deposited on to the fabricated silicon microneedles by LPCVD. The reflowed photoresist protected the bottom part of the needles under the reactive ion etching to remove the top part of silicon nitride. Photoresist reflow method was developed utilizing the temperature property of polymer. The photoresist acts like fluid at the temperature higher than its glass transition temperature (T_g). With baking temperature above the glass transition temperature, the excess photoresist from the top of the pyramid structure needle flows to thin the top layer of photoresist and covers the bottom part of silicon nitride.

Reflow method at 120 ^oC was used based on the glass transition temperature (T_g) of photoresist (AZ9260) of ~115 ^oC. The thickness of the photoresist or the length of the exposed tip is related to the spin coating speed. Figure 3.18 shows the microneedles with spin-coated photoresist after the bake in 120 ^oC for 15min. The tips of the microneedle were exposed after the photoresist reflowed from the top; and the surface of photoresist became planar at the space among the array of microneedles. The height of the exposed tip was depended on the spin coating speed. The height of microneedles increases at a larger coating speed. In the experiment, the length of the exposed tip measured was ~35 μm using coating speed of 2000 rmp. There was no obvious effect on the height of exposed tip after the baking time exceeded 20 minutes.

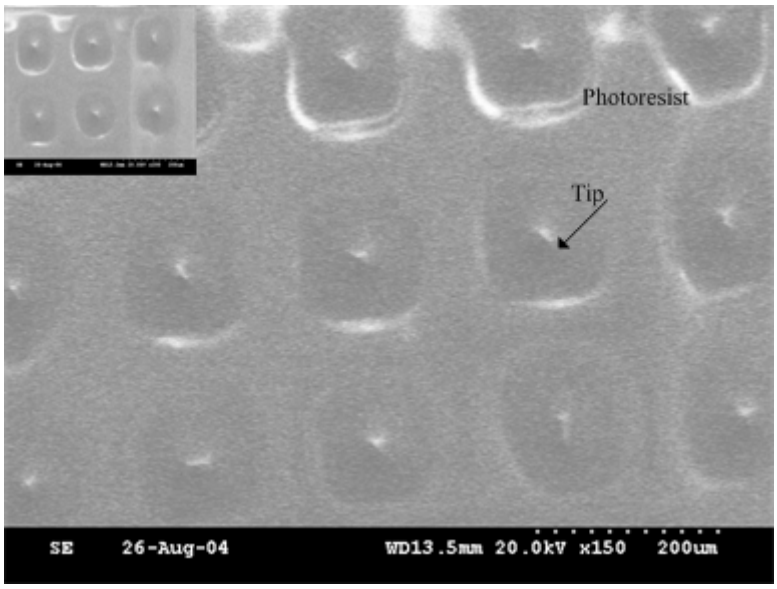

Figure 3.18 SEM Picture of microneedles coved by photoresist (top view)

3.2.3 Anodic Electrochemical Etching

The electrochemical etching of silicon in hydrofluoric acid (HF) electrolyte is the typical technique for the formation of porous silicon. The reaction in the electrolyte can be described by following chemical formula:

$$Si + 2HF + 2H \rightarrow SiF_2 + 4H^+$$
$$SiF_2 + 2H_2O \rightarrow SiO + 2HF + H_2 + O^-$$
$$SiO + 6HF \rightarrow H_2SiF_6 + 2H_2O$$

Depending on the doping types of silicon used in the anodic substrate, different pore morphologies can be achieved, ranging from nanoporous or microporous, to macroporous. Differences in pore size control the release of a drug. Macroporous silicon has attractive potential applications for large molecular drugs release. Additionally, etching macropores in p-type silicon provides better aspect ratios and better stability than in n-type silicon. P-type silicon can supply a porous structure itself without illumination in contrast to n-type silicon,

which simplifies the experimental setup [84]. In the electrochemical etching process, organic solutions, such as ethanol (EtOH), acetonitrile (MeCN), dimethylsulfoxide (DMSO) and dimethylformamide (DMF) with additional HF acid are commonly used to form the macroporous structure of p-type silicon [85][86]. The electrochemical etching parameters, such as the concentration of HF, anodic time and the current density, had influence on the product of porous structure. It was found that the porosity was increased with lower HF concentration and higher current density [87].

Figure 3.19 shows the experimental setup for anodic electrochemical etching used to generate the porous silicon tips. A positive potential was applied to the silicon sample, which formed the anode in the circuit. A thin gold layer was deposited on the backside of the silicon to facilitate a conductive contact layer. The platinum electrode was used as the cathode. A DC power supply (36 V-72 V) was used as the voltage power source. A multimeter was used to measure the voltage and the current in the circuit. A rheostat was applied to keep the circuit current at constant value, ensuring that the charge current density was stable. The electrolyte solution used was typically an organic solution mixed with hydrofluoric acid (HF). Various types of porous silicon could be achieved using various etching conditions including current density, electrolyte and etching time.

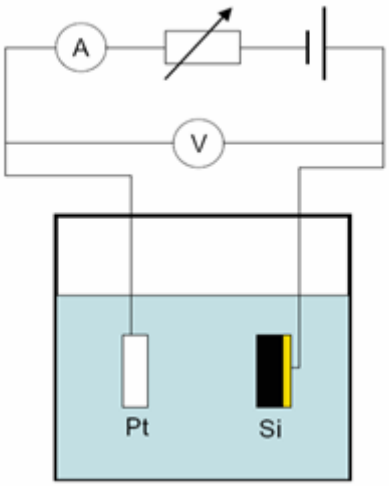

Figure 3.19 Schematic of the equipment set up for porous silicon formation

In the anodic electrochemical etching, p-type with (100) orientation silicon was used to characterize the etching process. The thickness of the wafer between 450 μm and 500 μm and the resistivity was ranged from 1 Ω · cm to 10 Ω · cm. In order to measure the depth of etching, the initial wafers were pattern with channel using silicon nitride mask. Ethanol (EtOH) and acetonitrile (MeCN) were used to investigate the influence of electrolyte on formation of the porous silicon. The components of the electrolyte solution were adjusted to the desired ratio. All the experiments were done at room temperature.

In the beginning, the samples were dipped into concentrated HF to remove the thin oxide layer on the surface. The current in etching process was varied from 4 mA to 20 mA in MeCN based electrolyte and 10 mA to 40 mA in EtOH based electrolyte. Porous silicon microstructures were then investigated by scanning electron microscope (SEM).

3.3 Experimental Results

3.3.1 Isotropic Etched Microneedle Structure

An isotropic etching process was conducted to fabricate microneedles in the STS ICP etch tool. This machine is well known for the application of Advanced Silicon Etching (ASE^{TM}) process for deep reactive ion etching (DRIE). DRIE was widely used in the generation of high aspect ratio silicon micro structures with vertical walls by alternating the plasma etching of silicon and deposition of a fluorocarbon polymer protective layer. However, a steep incline structure is required in the fabrication of microneedles. Therefore, in the experiments, the plasma deposition process was not performed and the plasma ion etching led to the vertical etching and lateral etching simultaneously due to isotropic nature of etching by fluorinated ion [88]. With the DOE investigation of the isotropic etching process, the etching parameters were optimized to achieve high aspect ratio structure with sharp tips and smooth surface. With a square as the mask pattern, the pyramidal structure was fabricated using sulfur hexafluoride/oxygen gases. The additional oxygen was included to ensure the reactant species remain available to interact with the silicon [89]. Figure 3.20 shows the etched microneedles using SF_6 (130 sccm) and SF_6/O_2 (130 sccm /13 sccm), respectively. With oxygen (<10%, by flow rate) added, the effect on the etched profile is negligible. However, the etching rate of silicon is increased with the additional oxygen, due to the competition between the two etchant species of F and O atoms for access to the active sites on the silicon surface [90].

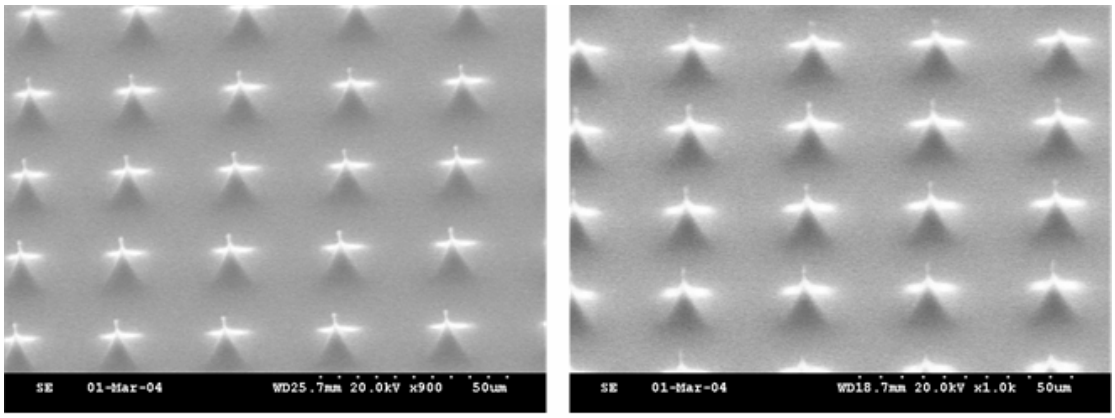

(a) Etched using SF_6 gas (b) Etched using SF_6/O_2 gas

Figure 3.20 SEM pictures of fabricated microneedle in SF_6 gas and SF_6/O_2 gas

The isotropic regime of the etching cycle using SF_6 gas in an ICP high density etcher was investigated in the characterization experiments in Chapter 3.3.1. In the isotropic etching process, a silicon oxide mask is superior to photoresist because the photoresist layer of the pattern can only sustain up to 10 minutes in the plasma environment with additional oxygen as working gas, and without protection by passivation cycle using C_4F_8 gas. By adjusting various etching parameters such as gas flow, pressure, and powers, control of the lateral etching rate and vertical etching rate was achieved. In the characterization experiments of isotropic etching by the DOE method, it was found that pressure has a dominant effect on the lateral etching rate. The etching rate initially increased with increasing pressure due to higher F concentrations but as pressure reached a certain value, the etching rate achieved the maximum then began to decrease. The characterization results were consistent with the post-process experiment, which utilized the SF_6 to etch the buried layer [91]. Figure 3.21 shows the SEM pictures of etched structures under various pressures, which were achieved by adjusting the APV position. The

SEM pictures show that a steep slope is more obvious under the higher pressure while the structures with arc appear with a decreasing in pressure.

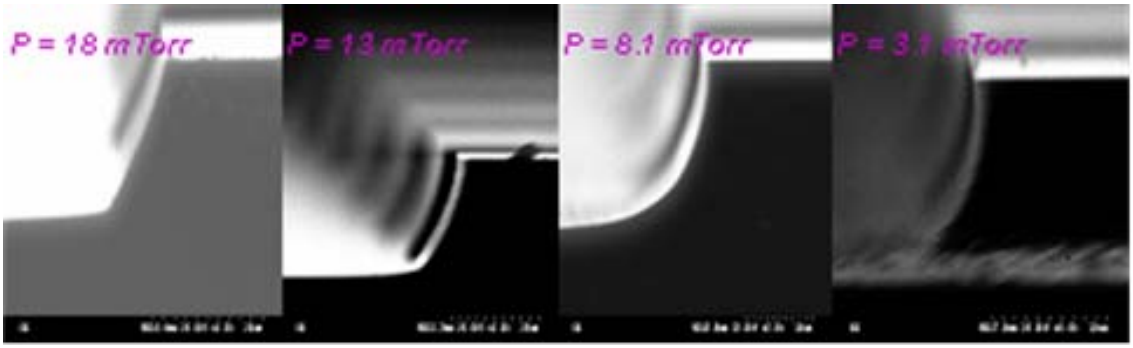

Figure 3.21 SEM photography of profile variation f at different pressures

Figure 3.22 shows the fabricated pyramid structures using SF_6/O_2 gas with the STS ICP system at different etching parameters [92]. The microneedle which is presented in Figure 3.22 (a) was achieved at following etching conditions: 12 W platen power, 600 W coil power, APV position at 60 ^{o}, and 150 sccm/15 sccm SF_6/O_2 flow rate. The microneedle which is presented in Figure 3.22 (b) was achieved at following etching conditions: 12 W platen power, 600 W coil power, APV position at 50 ^{o}, and 150 sccm/15 sccm SF_6/O_2 flow rate. High SF_6 gas flows lead to a fast etching speed with large surface roughness, as shown in the Figure 3.22. Meanwhile, the high platen power would be a reason for the rough surface according to the characterization result. Reducing the gas SF_6/O_2 flow rate to 100 sccm/10 sccm and decreasing the platen power to 10 W, the quality of the etched surface was improved. It was found that the steep slope of the etched structure could be generated at the higher pressures from the characterization results in Chapter 3.3.1. Therefore, the APV position was set at 60 ^{o} rather than 50 ^{o}. Figure 3.23 shows

the SEM picture of fabricated microneedles obtained at following condition: 10 W platen power, 600 W coil power, APV position at 60 ^{o}, and 100 sccm/10 sccm SF_6/O_2 flow rate.

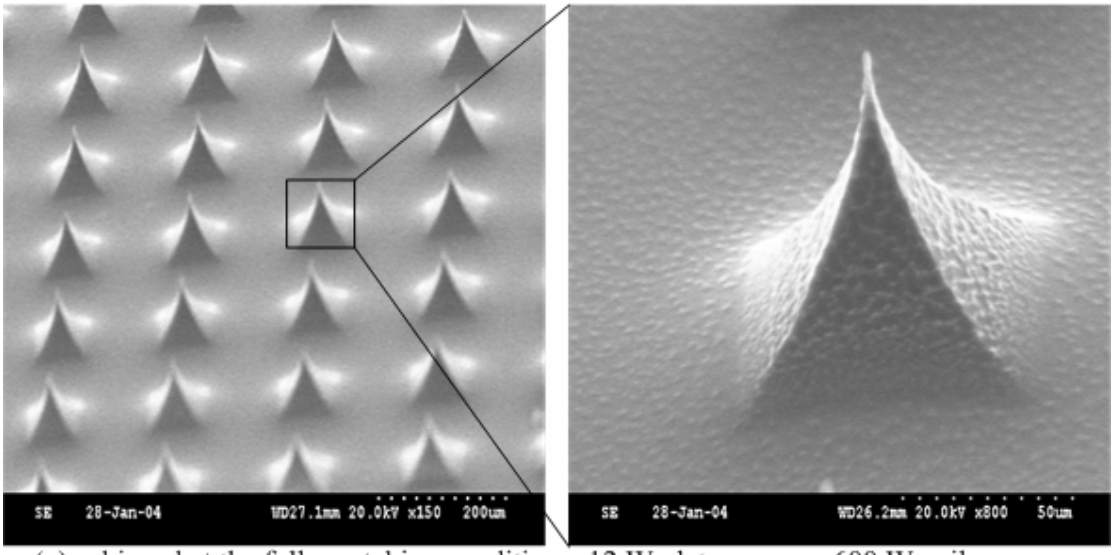

(a) achieved at the follow etching conditions: 12 W platen power, 600 W coil power, APV 60^{o}, 20 mTorr pressure, and 150 sccm/15 sccm SF_6/O_2 flowrate.

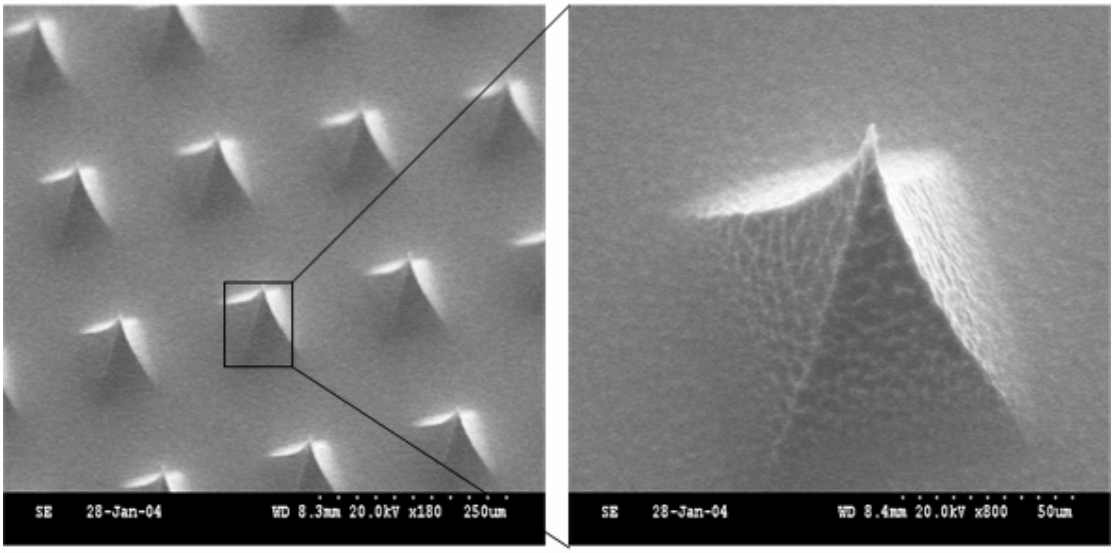

(b) achieved at the follow etching conditions: 12 W platen power, 600 W coil power, APV 50^{o}, 12 mTorr pressure, and 150 sccm/15 sccm SF_6/O_2 flowrate.

Figure 3.22 SEM photos of the needle arrays fabricated by DRIE ICP of STS at the controlled parameters

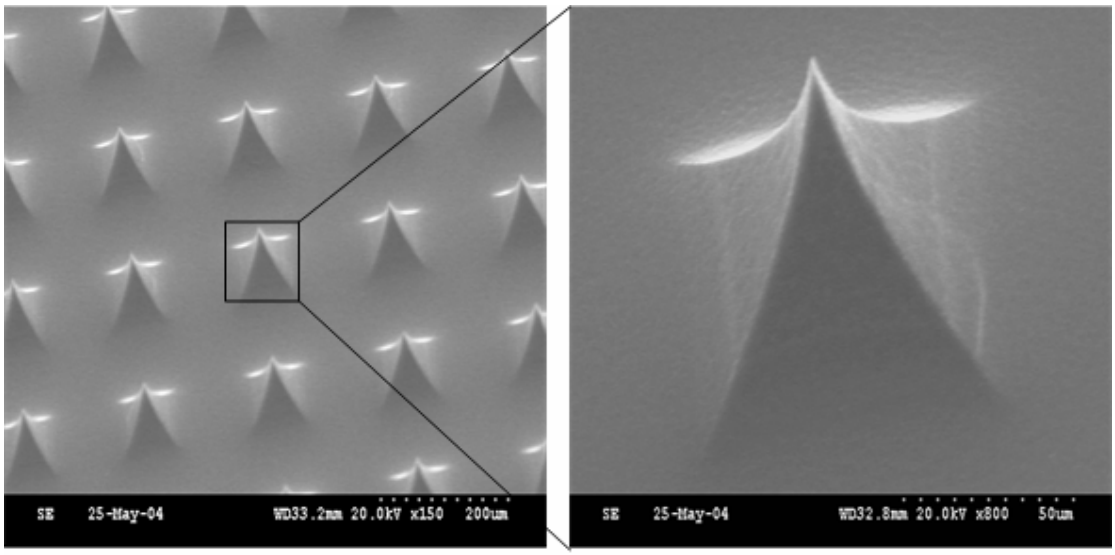

achieved at the follow etching conditions: 10 W platen power, 600 W coil power, APV 60°, 18 mTorr pressure, and 100 sccm/10 sccm SF_6/O_2 flowrate.

Figure 3.23 SEM pictures of microneedle with lower surface roughness

3.3.2 Anodic Electrochemical Etched Structure

The porous silicon layer was fabricated in the electrochemical etching process using HF mixed with organic solution. Figure 3.24 shows the surface of porous silicon etched in the solution of HF mixed with EtOH. The solution for the etching was HF (49%):H_2O: EtOH, 2:1:1 by volume. The etching time was 10 minutes. Figure 3.24 (a) shows the etched surface at a current density of 10 mA/cm^2 while Figure 3.24 (b) shows the etched surface at a current density of 20 mA/cm^2. Figure 3.25 shows the surface of porous silicon etched in the solution of hydrofluoric acid (HF) mixed with acetonitrile (MeCN). The mixture consists of two compounds of MeCN: HF (4 M): H_2O= 92%: 4%: 4% by weight. The 4M HF solution was achieved by diluting concentrated HF (49% wt). Figure 3.25 (a) shows the etched surface at a current density of 5 mA/cm^2 while Figure 3.25 (b) shows the etched surface at a current density of 10 mA/cm^2. It was found that

the porous silicon layer dissolved faster in HF/EtOH solution than in HF/MeCN solution. The formation of the porous silicon in HF/EtOH was not uniform. The porous structure formed in HF/MeCN was more controllable for the fabrication of the microneedle with porous tips.

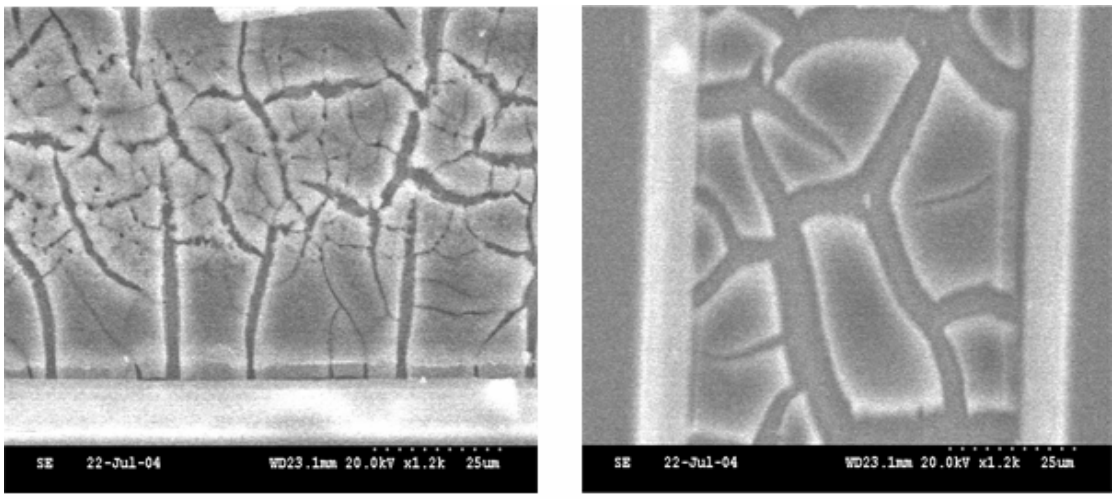

(a) (b)

Figure 3.24 SEM pictures of porous silicon surface achieved in electrolyte using HF/EtOH at different current densities ((a) 10mA/cm^2 (b) 20mA/cm^2)

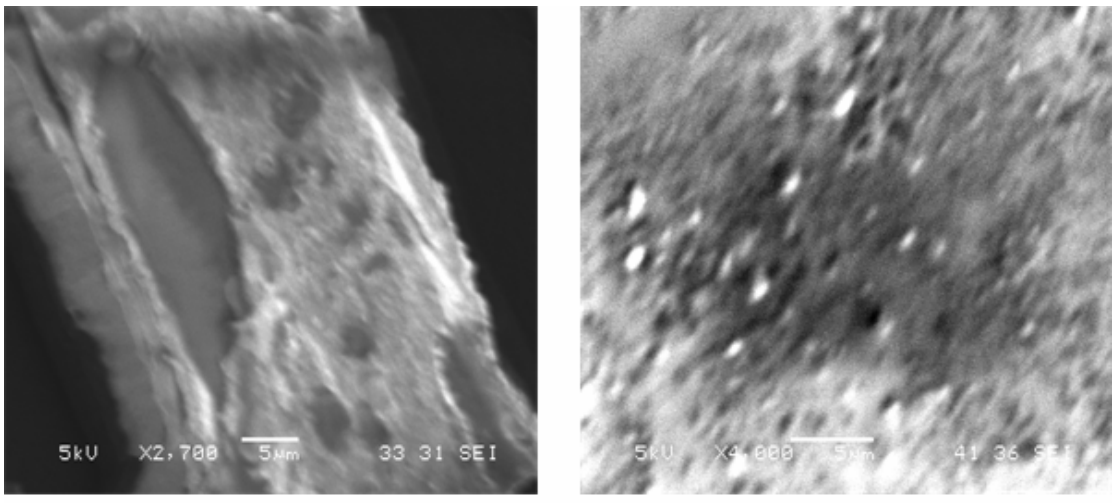

(a) (b)

Figure 3.25 SEM pictures of porous silicon surface achieved in electrolyte using HF/MeCN at different current densities ((a) 5mA/cm^2 (b) 10mA/cm^2)

The porosity of the porous silicon, which is defined as the fraction of void spaces in the structure, was pronounced at the high current density and longer etching time. The different porosity and pore structure is important for the potential drug release. Various porous tips were fabricated under different etching conditions. The porous tips presented in Figure 3.26 were achieved under the following conditions: electrolyte of MeCN: HF (4 M):H_2O= 92%: 4%:4%, current density of 4 mA/cm^2 and etching time of 10 min. A thin layer of porous structure was generated. As shown in Figure 3.26, the sharp tips remained almost intact after the anodic electrochemical etching.

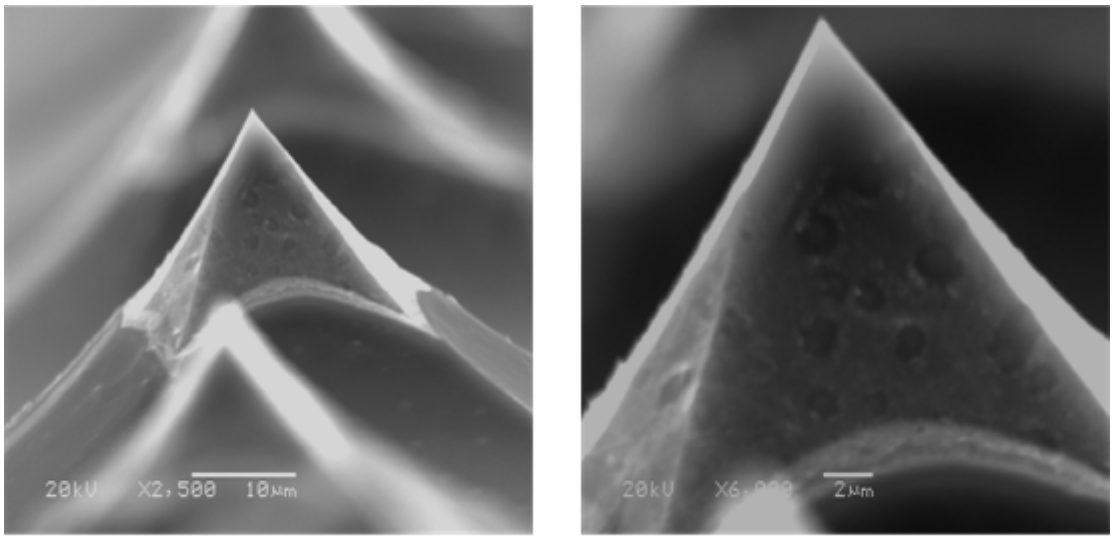

Figure 3.26 SEM photos of porous tips, etched in HF/MeCN, at 4mA/cm^2, 10min

The porosity increased with the increased etching current density and etching time. It is clear to see from the Figure 3.27. The etched structures showed in Figure 3.27 were achieved at

following conditions: electrolyte of MeCN: HF (4 M):H_2O= 92%: 4%:4%, current density of 10 mA/cm^2 and etching time of 30 min.

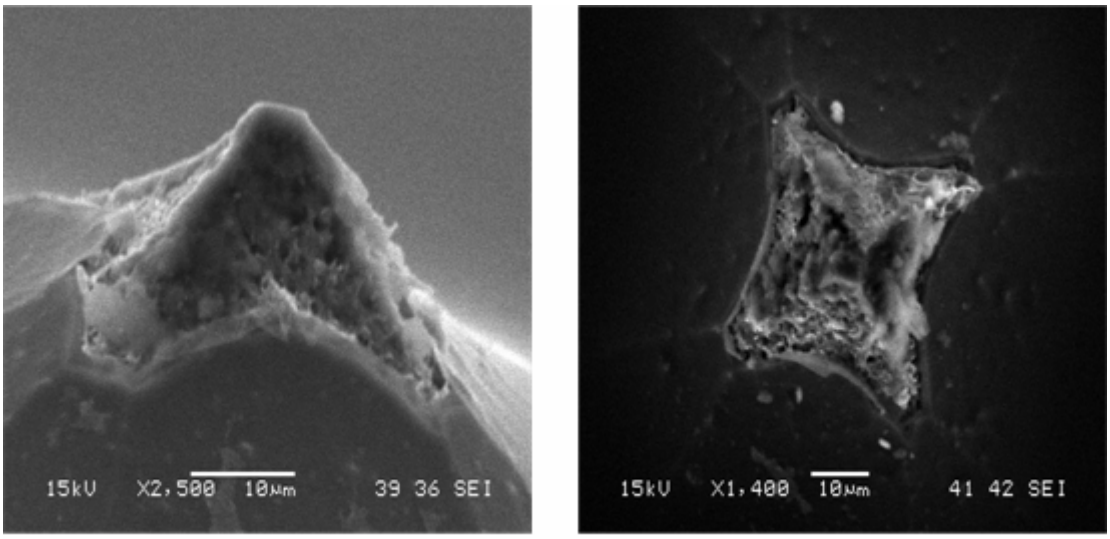

Figure 3.27 SEM photos of porous tips, etched in HF/MeCN, at 10mA/cm^2, 30min

When the etching time was increased to 50min, the exposed tips were further etched, as shown in Figure 3.28. The etched structures shown in Figure 3.28 were achieved under the following conditions: electrolyte of MeCN: HF (4 M):H_2O= 92%: 4%:4%, current density of 10 mA/cm^2 and etching time of 50 min. Figure 3.28 (c) shows the porous structure of the etched tips. It is clear that the porosity increased after long time etching.

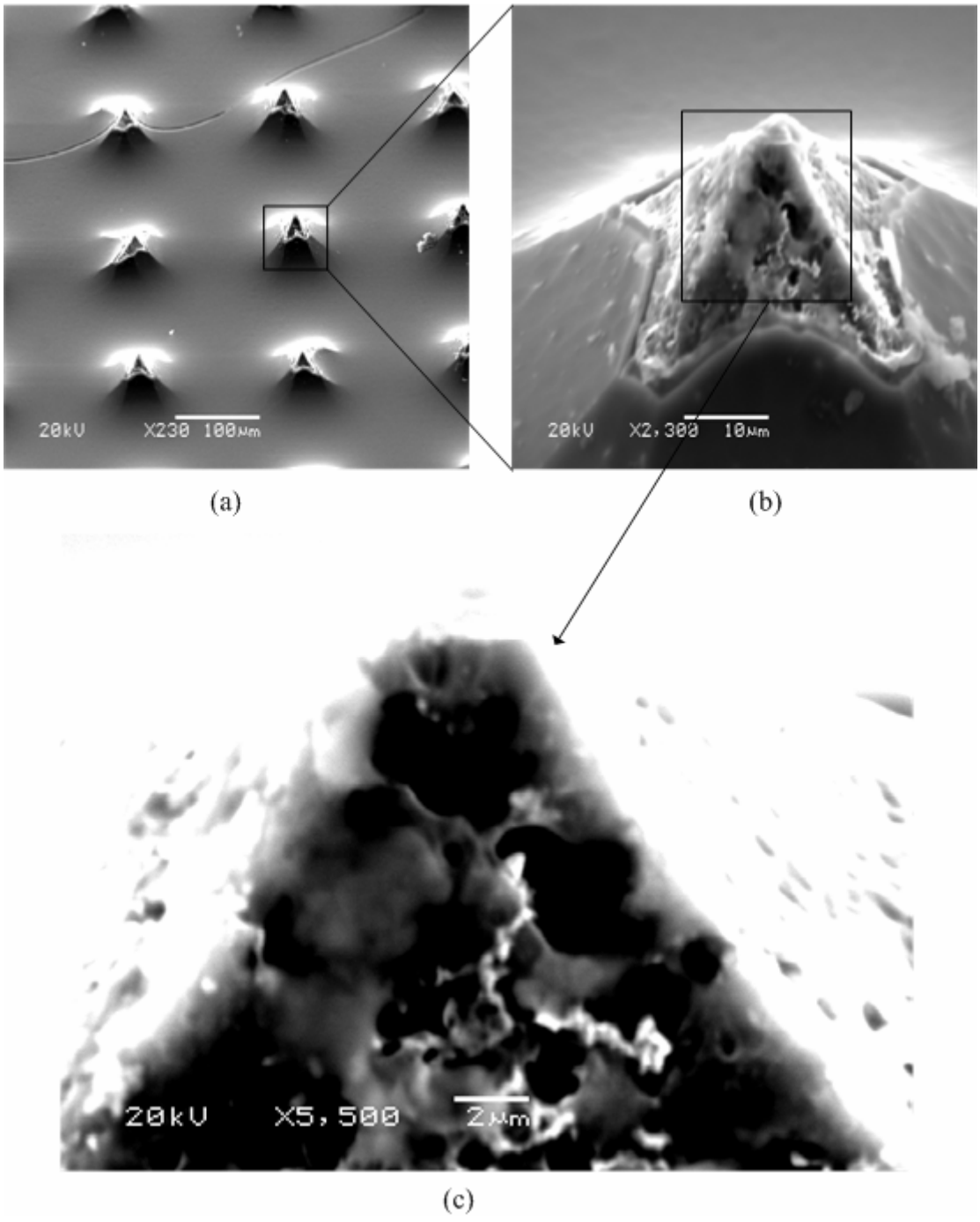

Figure 3.28 SEM photos of porous tips, etched in HF/MeCN, at 10mA/cm^2, 50min

3.4 Discussion

3.4.1 Fabrication of Microneedle Structure

The microneedle with sharp tips was successfully fabricated by the dry etching process using SF_6/O_2 gas in the ICP etcher. The profiles of the microneedle were controllable by adjusting the etching parameters. However, the dry etching process is an expensive process using high density inductive coupled plasma machine. Due to wet eatching's economical process, wet etching could be an alternative method for microneedles fabrication. Thus, anisotropic silicon wet etching in KOH was also investigated to fabricate microneedles in this research. Figure 3.29 shows the anisotropic etched structure using a silicon dioxide mask patterned with arrays of squares, the same as the mask used in isotropic dry etching with the ICP etcher. The blunt tips were generated by KOH wet etching at 80 ^{o}C. In this experiment, it was found that the wet etching process in KOH was difficult to control because of the complicated crystal plane dependent etching of the KOH solution. The three SEM pictures in Figure 3.29 were taken from the same sample after 40 minutes KOH etching. The silicon dioxide mask remained intact in Figure 3.29 (a), while the mask was damaged in Figure 3.29 (b). The top partial part of the microneedle was etched away in Figure 3.29 (c). Compared to the dry etching in SF_6/O_2 gas, the structure fabricated in the KOH wet etching was less controllable. In addition, the microneedles obtained in KOH wet etching were shorter than the microneedles fabricated in SF_6/O_2 isotropic dry etching under the same mask dimension.

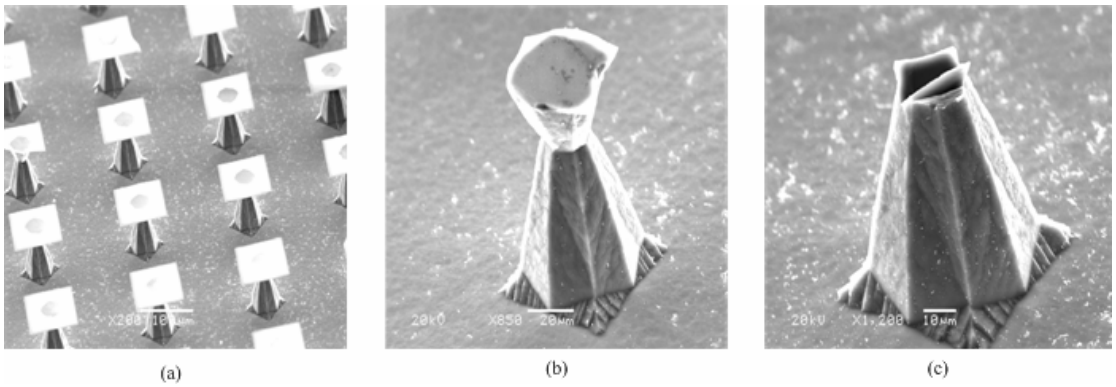

Figure 3.29 SEM pictures of microneedles fabricated in KOH with mask patterned in squares.

In order to fabricate microneedles with sharp tips, a modified pattern was used for KOH wet etch. The square pattern was revised to square with round corners mask. The cone-shaped microneedles were produced after 40 minutes KOH etching. Figure 3.30 shows the KOH etch using the revised mask. The uniformity of the etched structure was improved using the revised mask. The formation of the sharp tips was due to unequal etching rates along the various index planes. The shape of the mask and the position defined on a wafer would influence the fabrication. One solution to this problem would be to build up an etching model to estimate the etched structure in KOH by wet etching simulators. With the aid of KOH etching simulation, the design of the optimal pattern dimension could be predicted to achieve certain height of microneedles.

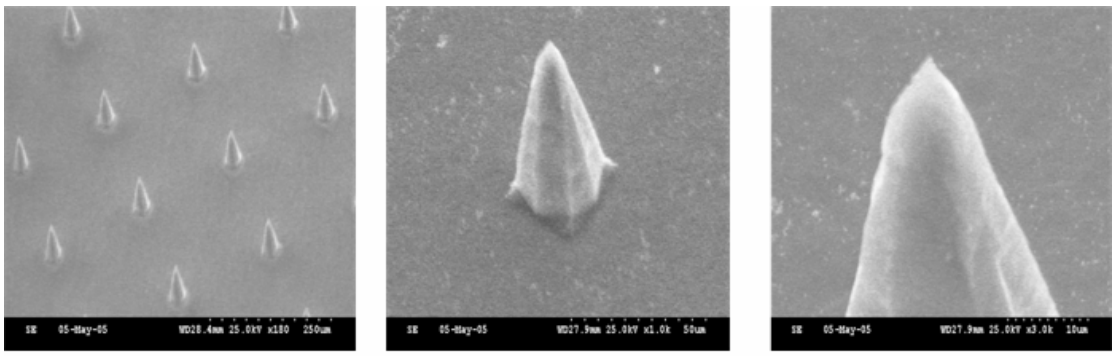

(a) (b) (c)

Figure 3.30 SEM pictures of microneedles fabricated in KOH using modified mask with round corner.

3.4.2 Porous Silicon Formation

Electrochemical etching was conducted to fabricate the porous silicon tips. Nanoporous and macroporous can be produced together during the etching process [93]. Further research need to be carried out to characterize the structural dimensionality of porous silicon on p-type wafer to investigate the structures of etched porous silicon. Additional experiments are necessary to investigate the effects of the resistivity of silicon wafers on the structure of porous silicon.

The porosity of porous silicon was found to be a function of the current density and a function of HF concentration in the electrolyte [94]. Therefore, the current in circuit has to be accurately controlled during the etching process. The resistance of the electrolyte used in this experiment was observed to be unstable. The changing resistance directly effects the formation of the porous silicon. This could be an explanation for the non-uniform macroporous surface obtained

in these experiments. A circuit with a current feedback controller placed in the etching circuit would be a solution for maintaining a constant current during etching.

Chapter 4 Analytical Model and Insertion Test of the Microneedle Array

A fabricated microneedle array with biodegradable tips was designed to deliver drugs across the skin. The mechanical strength of the array must be strong enough to penetrate into the skin without failure. The strength is related to the geometrical and material properties of the microneedles. When an applied load is greater than the yield strength of the material, failure occurs. The geometry of the fabricated needle determines the critical loading. Not all microneedle geometries are able to insert into skin at a reasonable force without breaking. Studies have shown that when the solid silicon needle arrays were inserted into the skin, part of the needles was damaged in the top of 5-10 μm regions [11]. The broken tips of silicon needles were observed during their insertion in the initial study. The biological complication resulting from a broken tip left in the skin could be minimized by using a biodegradable porous tip. However, the needle must be able to withstand the force required to insert the microneedle into the skin. In this chapter, the analytical model of insertion force and fracture force was investigated to predict the critical loadings. In addition, the insertion test was carried out using the tissue sample.

4.1 Theory of Microneedle Insertion into Skin

The structural mechanisms of soft tissue to resist fracture are partially understood by measuring the toughness of tissues, which is defined by the energy required to make unit area of crack [96]. The deformation of tissues was initially defined in a linear elastic manner. A non-linear elastic deformation model was subsequently developed to simulate crack formation in tissues of organism [95]. Initially, the assumption that all the lost energy is paying for crack growth was established to model the crack in soft tissues. However, it was found that the soft tissues show large hysteresis when loaded and unloaded. This phenomena indicates that the all the lost energy does not go into crack production because part of the energy was stored in the soft tissues. Pereira *et al* [96] built up a platform to determine the skin toughness using scissors *in-vitro* based on the theory that crack growth proceeds when the energy available from the release of stored potential strain energy is equal or exceeds the critical value required to create a new fracture surface. A similar approach has been used to model insertion in the skin with microneedle in vitro. The modified theory that the needle can be inserted into the skin when the energy delivered to the skin by the needle exceeds the energy necessary to create a tear in the skin has been postulated to predict the force of insertion to skin [43].

Equation 4.1 describes the fracture occurrence for stable cracking process in the skin using a displacement controlled testing machine.

$$\frac{dW}{dA} \geq \left(\frac{\partial G_c}{\partial A}\right)_U \qquad \text{E- 4.1}$$

Here, dW/dA is the rate of change if toughness with crack area $\left(\partial G_c / \partial A\right)_U$ is the rate of change of strain energy at constant cross-head displacement U, and W is the work of fracture of the material. Gc represents the crack fracture toughness and A reveals the interfacial surface area.

Assuming a controlled and slow (quasi-static) crack in the skin, the roughness G, which is the work required to propagate a crack by unit area, is at the critical values G_c at all time. Hence, the total input work W required to create a new fracture surface is $G_c * \delta A$, is shown in equation 4.2:

$$\delta W = G_c * \delta A \qquad \text{E- 4.2}$$

The relation between the crack fracture toughness (G_c), the total work input to punch the crack (δW) and the surface area of the new fracture (δA) at constant crosshead displacement (U) can be described by Equation 4.3:

$$G_c = \left(\frac{\delta W}{\delta A}\right)_U \qquad \text{E- 4.3}$$

In the case of the microneedles insertion into the skin, the puncture fracture roughness G_p, is used to instead of the crack fracture roughness G_c in equation 4.3. Therefore, the equation for G_p is:

$$G_p = \left(\frac{\delta W}{\delta A}\right)_U \qquad \text{E- 4.4}$$

In the insertion of microneedles, the total input work W is related to the change of potential energy between the unaltered skin and the skin prior to needle penetration. The input energy could be calculated as the area under the load versus displacement curve before fracture, as illustrated in equation 4.5

$$\begin{aligned} \delta W &= F dx \\ W &= \int F dx \\ W &= \int_{x=0}^{x=x_i} F dx \end{aligned} \qquad \text{E- 4.5}$$

Where F is the force applied by the needle, x is the axial position of the needle, xi is the displacement during insertion, and the boundaries of integration are from the point of needle contact with the skin to the point of needle insertion.

Equation 4.4 can be arranged to the followed form:

$$\delta W = G_p * \delta A \qquad \text{E- 4.6}$$

Combining equation 4.5 and equation 4.6, the equation 4.7 was derived to present the insertion mechanism for microneedles.

$$G_p * A = \int_{x=0}^{x=x_i} F dx \qquad \text{E- 4.7}$$

where G_p is the puncture fracture toughness and A is the area of contact between the needle and skin, which is equal to the size of he top of tip. The left side of the equation 4.7 is the work required to initiate a puncture in the skin, and the right side of equation is the summation of work applied to the skin during the deformation.

It was found that the data of insertion force and displacement in the testing fit well with the exponential relationship between force and displacement of skin. The empirical equation derived from these experiments has the following form:

$$F = \theta * Exp(\tau x) \qquad \text{E- 4.8}$$

where θ is the pre-exponential constant and τ is the exponential constant [97][98]. The variables θ and τ are determined by fitting the measured experiment data. When the equation 4.8 was substituted to equation 4.7, the equation, $G_p * A = \int_{x=0}^{x=x_i} F dx$ can be rewritten as follows:

$$G_p * A = \int_{x=0}^{x=x_i} \theta * Exp(\tau x) dx \qquad \text{E- 4.9}$$

Finally, the equation 4.9 was solved the fit value of insertion force.

$$\frac{\theta e^{\tau x_i}}{\tau} - \frac{\theta}{\tau} = G_p * A$$

$$F = \tau * G_p * A + \theta \qquad \text{E- 4.10}$$

where F is the insertion force. Equation 4.10 predicts that insertion force linearly depend on the area of needle tips. Moreover, the puncture toughness G_p is determined using the slope of a graph of insertion force versus area of needle tips. Davis *et al* [43] reported that the insertion force is a linear function related to the inertial area of the needle tip. It was found that the insertion force, which was assumed to be perpendicular to the skin, was ~1.3 N at the interfacial area (10000 μm^2) based on the puncture toughness of skin, 30.1+0.6 kJ/m^2.

4.2 Analytical Model of Fracture Forces

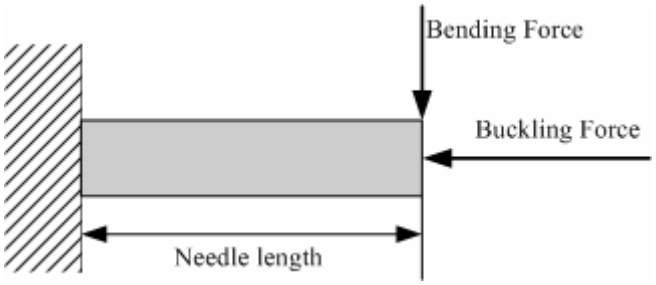

Figure 4.1 Modelling for microneedle

A needle is typically modeled as a cantilever, as shown in the Figure 4.1 [99]. The bending force ($F_{Bending}$) will cause deflection of the tip. The bending force has a critical effect on fracture of silicon needles structure because of silicon's brittleness. When the strain of the tip is close to the material yield strain, the structure fracture occurs. In addition, when the needle has been inserted into the skin, it may not be perpendicular to the surface. The insertion force can be divided into the bending force ($F_{Bending}$) and the buckling force ($F_{Buckling}$).The fracture of a microneedle is due to stresses in the structure exceeding the ultimate stress of the constituent material or buckling caused by elastic instability of the structure. The microneedle fracture force can be predicted by analytical method or finite element method using the geometry model of microneedles. The porous tip deflection and critical buckling force are also related with the Young's modulus of fabricated porous structure.

The fabricated microneedle is the pyramidal-like structures, which has been presented in Chapter 3. Therefore, the microneedle is assumed as the perfect pyramidal structure and its schematic is shown in Figure 4.2. During the microneedle insertion into the skin, there are two

possible failures: yield failure and critical buckling. The loading force (P) can be decomposed to the bending force (P_t) and buckling force (P_{cr}), as shown in Figure 4.2 (a). The bending force may cause structural failure when the maximum normal stress caused by shear momentum is greater than the yield stress. Since microneedles are typically high aspect ratio structures, the failure may occur because of buckling. The sketch of pyramidal structure is presented in Figure 4.2 (b). The pyramidal structure is with a structure height L, a length of bottom side b, a length of top side a. The tapering angle α is $\tan^{-1}((b-a)/2L)$.

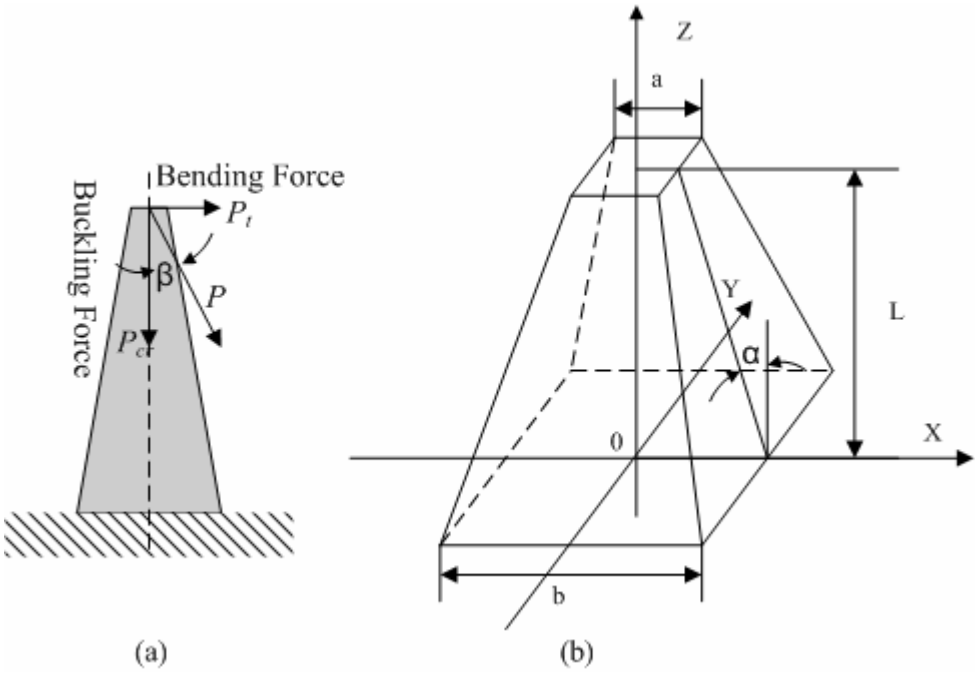

Figure 4.2 Model for the analytic solution of critical loadings: (a) bending and buckling model of microneedle, (b) schematic diagram of the square pyramid column.

4.2.1 Analysis of Bending Force

To estimate the fracture under bending force, it is necessary to calculate the absolute maximum normal stress in the needle using the flexure formula [100]:

$$\sigma(z) = \frac{M(z)}{S(z)} \qquad \text{E- 4.11}$$

where M(z) is the bending moment and S(z) is the section modulus, which is represented by I(z)/c. I(z) is the needle moment of inertia; and c is the perpendicular distance from the neutral axis to the point farthest away from the neutral axis. The flexure formula (E-4.11) is meant for a prismatic member, but it can also be used for a member of slight taper (taper angle within 15^{o}). For the case of a square based pyramidal structure with bottom length b, top length a and height L, the length of the cross-section H(z) at any position z can be expressed as:

$$H(z) = b - \frac{(b-a)}{L} z \qquad \text{E- 4.12}$$

The area moment of inertia at any position z is,

$$I(z) = \frac{H^4(z)}{12} \qquad \text{E- 4.13}$$

By applying the flexure formula, the stress along the axis z was written as:

$$\sigma(z) = \frac{P_t(L-z) * (H(z)/2)}{H^4(z)/12} = \frac{6P_tL^3(L-z)}{(bL-(b-a)z)^3} \qquad \text{E- 4.14}$$

To determine the position z which has the maximum normal stress, we take the derivative of σ with respect to z and set it to zero, which gives:

$$\frac{d\sigma(z)}{dz} = \frac{18P_tL^4(b-a) - 6P_tL^3(bL-(b-a)z + 3z(b-a)}{(bL-(b-a)z)^4} = 0$$

Thus

$$\begin{aligned} z &= \frac{2b-3a}{2(b-a)}L \\ &= L - \frac{a}{4\tan\alpha} \end{aligned} \qquad \text{E- 4.15}$$

Substituting into Equation E-4.14, the absolute maximum normal stress caused by bending stress is:

$$\begin{aligned} \sigma_{\max} &= \frac{2P_tL}{(b-a)a^2} \\ &= \frac{P_t}{a^2\tan\alpha} \end{aligned} \qquad \text{E- 4.16}$$

The silicon and porous silicon are brittle materials; therefore their fracture stress should be approximately equal to the yield stress. It was found that with larger topside length and taper angle of the needle, the critical loading of the bending force increases. For a single porous tip needle with 30 μm height, a 5 μm length of top side, and a 20 μm length of bottom side, the maximum normal stress under bending moment occurs at the position z of 15 μm. Based on the yield strength of porous silicon of 100 MPa [101], the bending force which reaches the yield

strength at the tip of the porous needle was found to be 0.6 mN. Due to the design of a 20 by 20 microneedle array, the critical bending force for the fabricated needle array was 0.24 N, 400 times more than a single needle endures. Bending force exists when the needle is not perpendicular to the skin. With the inclined angle (β) presented in Figure 4.2(a), the limited bending force in insertion is 1.3*tan (β) N. Since the angle β is small (<5^{o}) in experiment, the bending force at the required insertion force (~1.3 N) is 0.11 N. Therefore, the critical bending force 0.24 N for the fabricated microneedle array is larger than the insertion limit.

The facture loading limitation of bending force is clearly represented using the charts shown in Figure 4.3. The critical bending force under the insertion required force was plotted with the variation in the width dimension for single microneedle. The inset limitation is calculated as 0.284 mN (1.3*tan (β) /400 N) for a single needle. When the top length (a) is less than 2 μm, the fracture will occur during the insertion at any base length. In the case of small base length, for example 10 μm, the fracture also will occur.

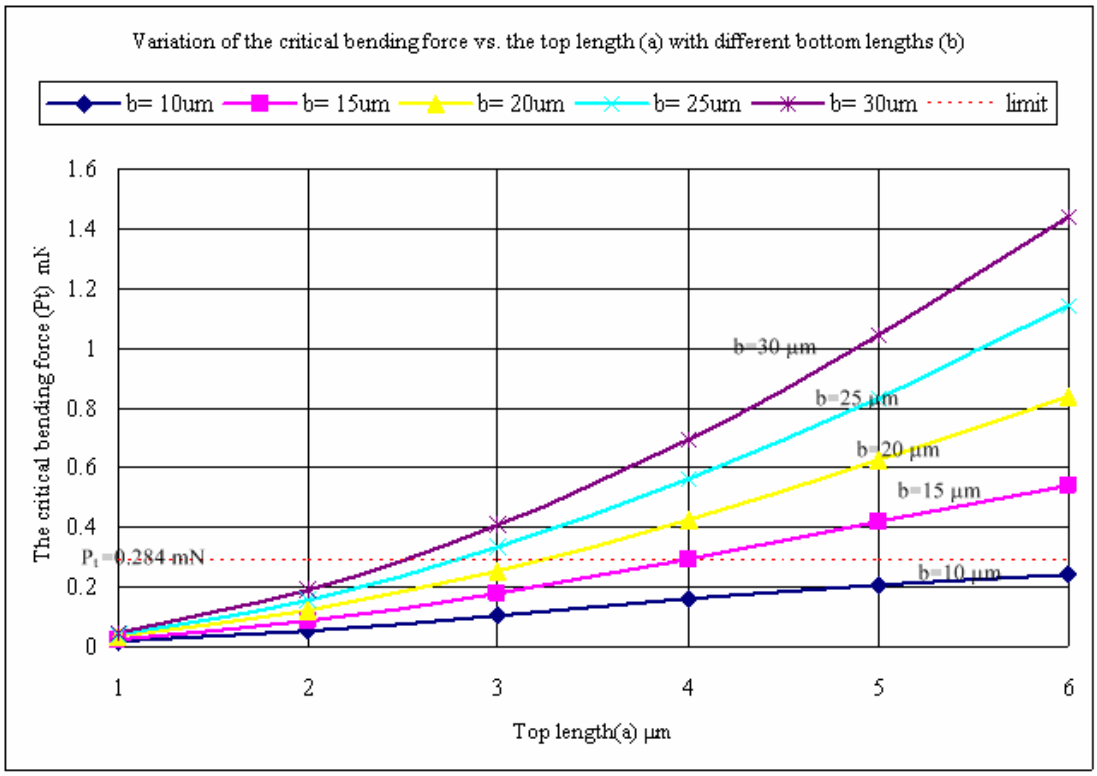

Figure 4.3 The critical bending forces and the insert limitation as a function of the top length for five different base length cases.

4.2.2 Analysis of Buckling Force

The prediction of the load that leads to the buckling of pyramid column is based on the following equation [100]:

$$EI(z)\frac{d^2y(z)}{dz^2}+M(z)=0 \qquad \text{E- 4.17}$$

with the appropriate boundary conditions, where E is the Young's modulus of the material, I(z) is the moment of inertia about the centroid, y(z) is the assumed deflected shape and M(z) is the bending moment distribution. In our analysis, the pyramidal column is fixed at the bottom (z=0)

thus there is no deflection at the bottom. It is free at the top (z=L). Using the energy method, Smith [102] solved the critical buckling load of the fixed-free column. The assumptions are that the deflected shape accounts for first mode buckling and satisfies the boundary condition for a fixed –free column. The critical buckling load (Pc_r) is:

$$P_{cr} = \frac{\pi^2 E}{2L^3}\int_0^L I(z)\cos^2(\frac{\pi z}{2L})dz \qquad \text{E- 4.18}$$

Equation E-4.18 can be applied to any columnar structure by expressing the area moment of inertia as a polynomial of z ($I(z) = \sum_{i=0}^{n} k_i z^i$). Kim *et al* [102] used it to determine the critical buckling for a hollow truncated cone column for microneedle made of the electroplated nickel. Substitution of Equation E-4.13 into Equation E-4.18, the critical buckling load for the needle can be determined as follows:

$$P_{cr} = \frac{E}{240\pi^2 L^2}\begin{bmatrix} \pi^4(b^4 + b^3a + b^2a^2 + ba^3 + a^4) \\ +20\pi^2(b-a)(a^3+b^3) \\ -120(a+b)(b-a)^3 \end{bmatrix} \qquad \text{E- 4.19}$$

For a single porous tip of a needle with 30μm in height, 5 μm in length at top side, 20 μm in length at bottom side, the critical buckling force is found to be 39 mN based on the Young's modulus of the porous silicon of 2.4 GPa [103][104]. Due to the 20 by 20 array of the microneedles, and with the assumption of uniform external stress, both yield strength and buckling force limit will be 400 times greater than for a single microneedle. The critical buckling force for the fabricated needle array is 16 N, which is much larger than the force

(~1.3N) required for insertion into the skin. Compared to the critical loading for a truncated cone with a structural height L, a bottom diameter b and a top diameter a, the loading for a square pyramid is 1.7 times greater, because the ratio of the area moment of inertia for a square pyramid to a truncated cone is $\frac{1}{12}:\frac{\pi}{64}=1.7$.

The facture loading limitation of buckling force is clearly represented using the charts as shown Figure 4.4, which illustrates the critical buckling force under the required insertion force with the variation in width dimension for a single microneedle. The insert limitation is set as 3.25 mN (1.3/400 N) for a single needle. It is clearly found that the small value of base length (b, 10 μm) is below the insertion limitation.

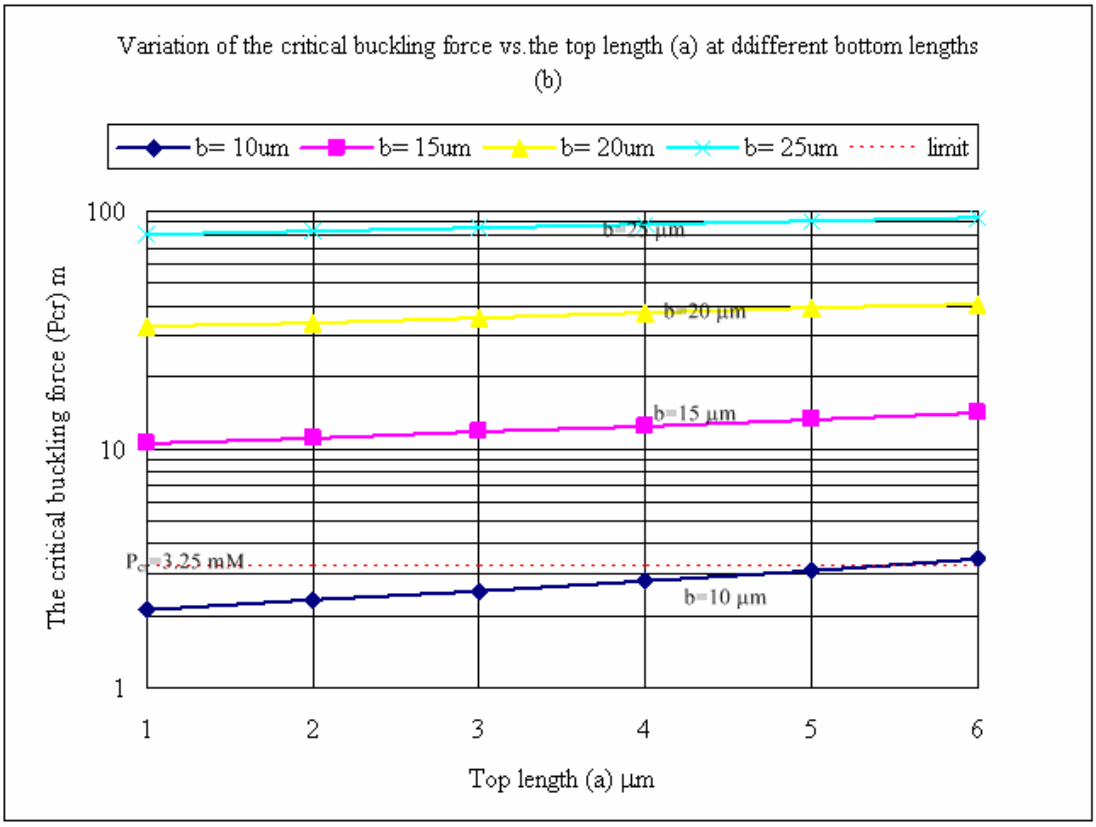

Figure 4.4 The critical buckling forces and the insert limitation as a function of the top length for five different base length cases.

4.3 Testing of Fabricated Microneedles

The microneedles were inserted into skin from chicken leg and then removed to test the feasibility of fabricated microneedles to pierce tissues. The fat under the skin was first cut off; and then the skin was cleaned with isopropyl alcohol. The microneedles were dipped into red dye before they were inserted into the model tissue. Figure 4.5 shows the experiment set up for the insertion. To prevent the microneedle touching with the surface of support part, the skin was fixed on a plate by tape. The applied force ranged from100 g to 500 g, (0.98 N ~ 4.9 N). Solid

microneedle array and microneedle arrays with various porous tips were used in the insertion test. Three types of porous tips, which were discussed at Chapter 3.3.2, were used in the insertion into the sample model.

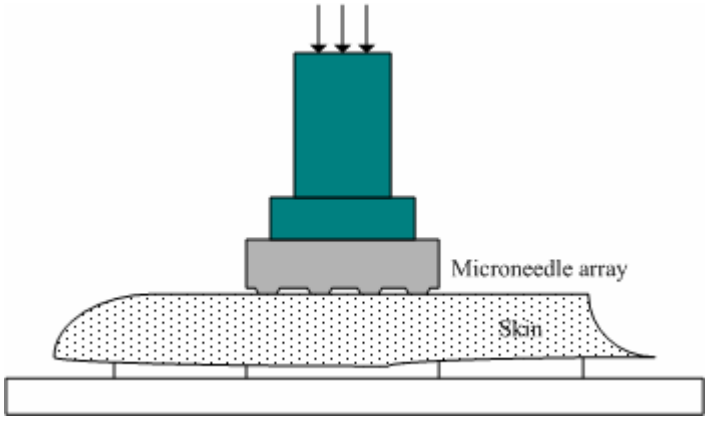

Figure 4.5 Schematic drawing of insertion set up for microneedles

In the skin test experiment, solid microneedle array was easily insertion into the skin because of the small interfere area of tips, which lead the high insertion pressure. Figure 4.6 shows the microneedle array before insertion. The dye was deposited on the tips.

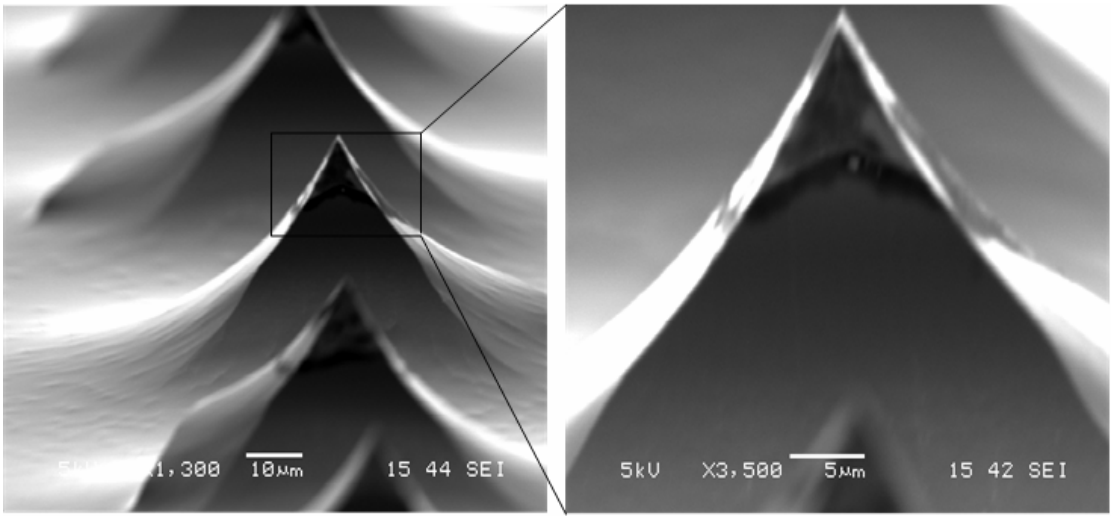

Figure 4.6 SEM pictures of solid microneedle array before insertion

No obvious damage of tips was observed after insertion. Figure 4.7 shows the tips after insertion. It was found that the pyramidal microneedle structure easily pierced the sample model, creating a microhole on the skin.

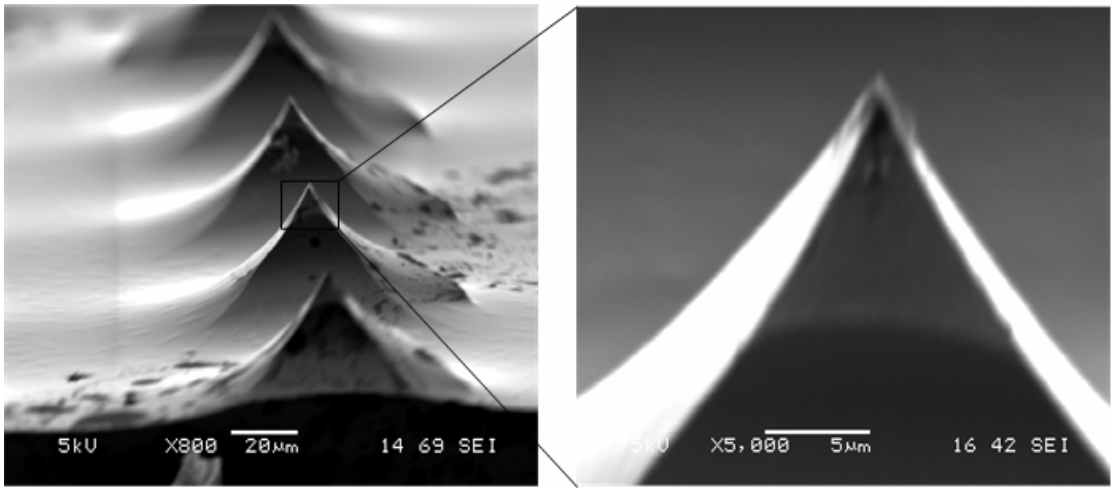

Figure 4.7 SEM pictures of solid microneedle array after insertion

The insertion force needed for the insertion test of the microneedle array with porous tips, which were etched at 4 mA/cm^2 current density and 10 minutes etch time was also less than 0.98N. The porous tips were blunt during the insertion. The deposition of dye was obvious in the SEM picture of the microneedle after insertion. It confirmed that the porous structure has the potential application for loading drugs. After the microneedle array was removed, the skin was observed staining with red dye using a microscopy. Figure 4.9 shows the holes left by the microneedles. The red dye was clearly observed on the skin.

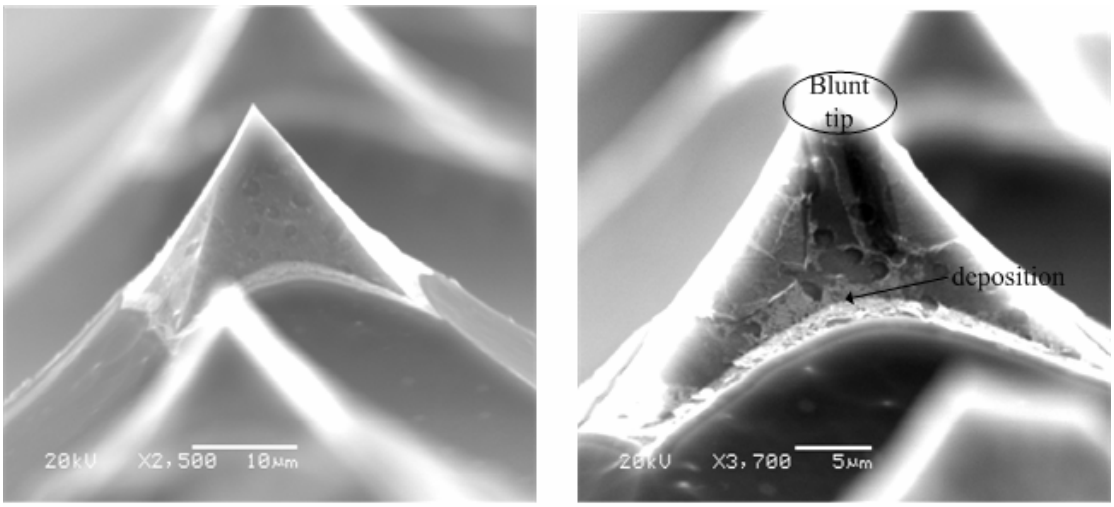

Figure 4.8 SEM pictures of microneedle array before and after insertion

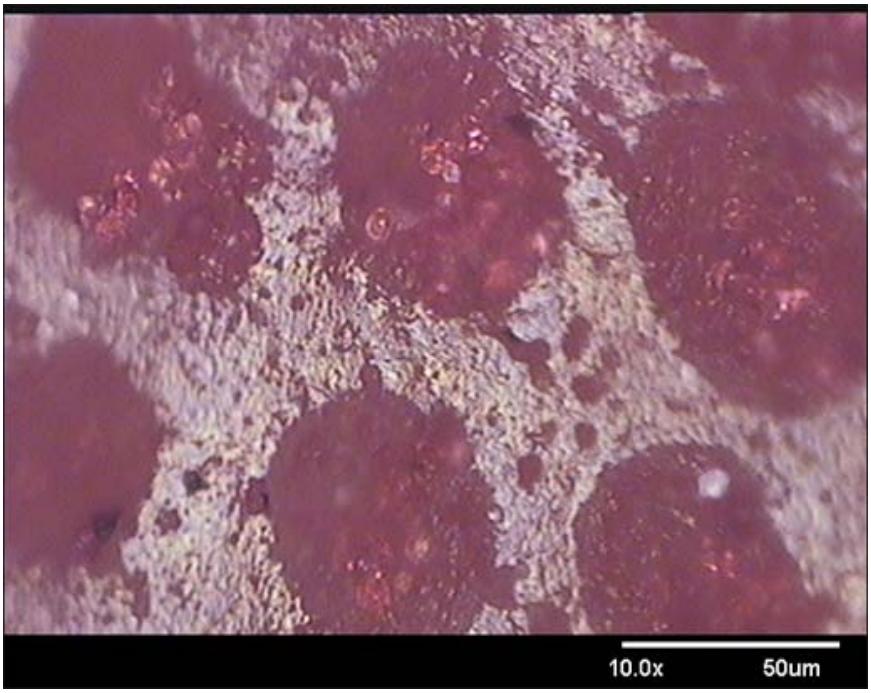

Figure 4.9 Photomicrograph of sample skin after microneedles were inserted and removed

The insertion force increased (~1.96 N- 2.94N) for the insertion test of the microneedle array with porous tips, which were etched at 10 mA/cm^2 current density and 30 minutes etch time. The increased insertion force is due to the increased area of the tips. The porous tips were imperfect after insertion. Figure 4.10 shows a SEM picture of porous tip after insertion. One side of porous layer was removed in the insertion because of friction. However, pathways were created in the skin when the microneedle array was inserted into the tissues, as shown in Figure 4.11. The SEM pictures were taken from the backside of the skin. These results indicate that the microneedles with porous tips are potentially useful for transdermal drug delivery.

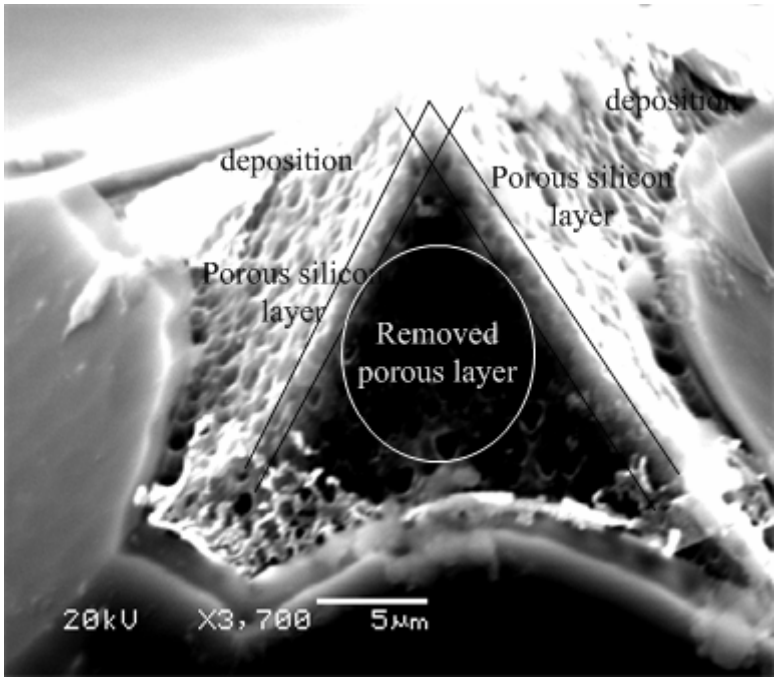

Figure 4.10 SEM pictures of microneedle array after insertion

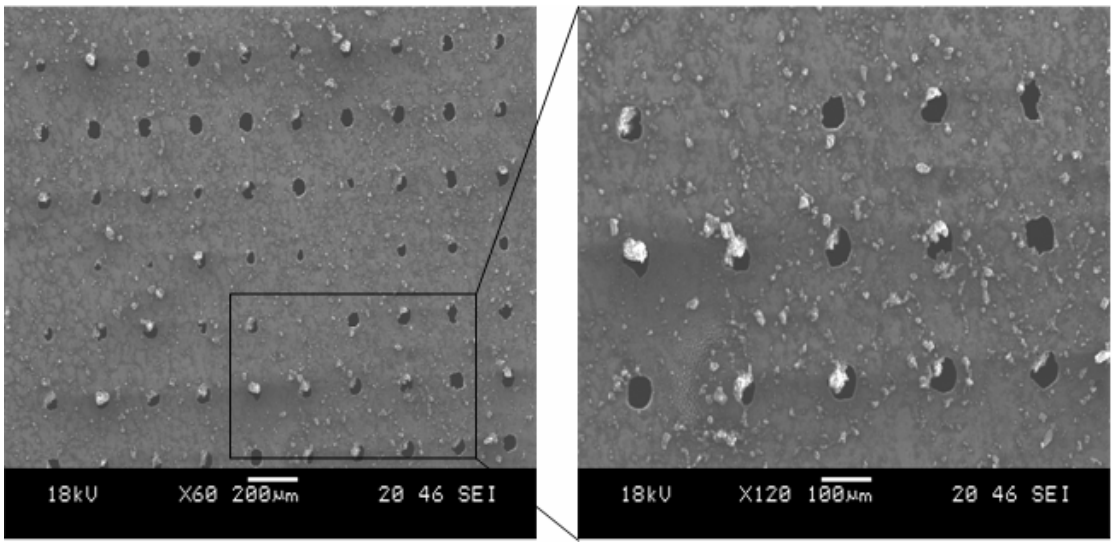

Figure 4.11 Picture of sample skin after piercing with microneedles

Few of the microneedle arrays with porous tips, which were etched at 10 mA/cm^2 current density and 50 minutes etch time, successfully created microholes on the sample skin model in the insertion test. Figure 4.12 shows that some tips are broken in the surface. The insertion force was increased to the range of 1.96 N ~ 4.9N. Several microneedles failed under the force 4.9 N, but there was no obvious pathway onto the skin model. Therefore, the porous structure with high porosity may not fulfill the requirement for insertion into skin.

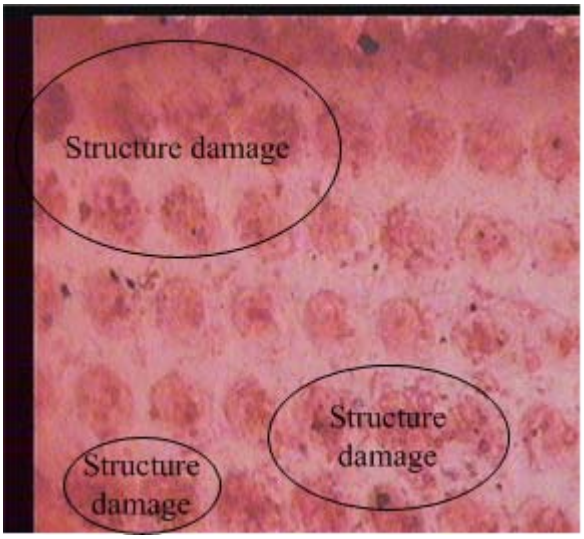

Figure 4.12 Photomicrograph of sample skin after microneedles were inserted and removed

4.4 Discussion

The theory of microneedle insertion into skin was established based on the theory of energy balance in this chapter. The analytical model for the critical loadings was built up based on the structure of fabricated microneedles. The analytical analysis of the bending force and the critical loading for a square-based pyramidal structure was derived. The variations of the square cross-section were expressed as a function of their axial coordinate to analyze the bending normal stress and critical buckling loading. This analytical method can also be used for other microneedle structures with different cross-sections. Moreover, the quantitative analytical results indicated that a needle with a porous tip can be inserted into the skin at a reasonable force.

The insertion testing confirmed the prediction in the analytical model. The microneedle arrays with low porosity successfully pierced into the skin. The biodegradable porous tips will not cause the inflammation even the tip was broken into the tissues. Therefore, the fabricated microneedles have the ability to created microholes in the skin for enhancement of skin permeability in drug delivery. The characterization of skin permeability and in vivo testing of drug delivery need further be carried out to realize the clinical applications of the microneedle array.

The mechanics of microneedle insertion into the skin are not well understood because the skin properties are difficult to obtain with current data model of materials. Therefore, there are some issues in the prediction of insertion force that only depending on the needle geometry. With the further investigation on skin properties, the mechanics of microneedle insertion could be explained more explicitly.

Chapter 5 Design and Fabrication of Microsystem for Injection

5.1 Design Specification

A microsystem was designed for the application of liquid injection to target tissues in precise controlled doses. It contains a hollow microneedle array where individual microneedles have an outer diameter less than 80 μm , an inner diameter less than 30 μm, and a length of 200-300 μm, a glass reservoir and a valve, fluid channel, a pressure cavity, two piezoelectric (PZT) discs, and an inlet aperture. The silicon hollow microneedle array was designed to inject drugs into specific targets, such as embryo of drosophila, cells, and localized tissues. The actuation components including the pressure cavity, fluid channels, and the actuator were designed to pump the micro-volume liquid out of the reservoir into tissues.

The microsystem to precisely deliver liquid drugs consists of three major modules: injection, valve, and reservoir modules, as shown in Figure 5.1. The injection module is designed to change the pressure in the pressure chamber and drive the medicine into target tissues through the microneedle array. In order to achieve a controllable and precise fashion in the injection, a PZT actuator, PZT-1 in Figure 5.1, is used and attached to the bottom of the glass chamber, the glass membrane. Deformations of the glass membrane are precisely controlled by voltages applied to PZT-1. As it deforms upwards, the glass membrane is able to push the medicine in

the pressure chamber through the microneedle array to reach the tissues. The valve module is designed to control on/off of the medicine flowing into the pressure chamber. The module consists of a PZT actuator, PZT-2 in Figure 5.1, and a glass membrane attached to PZT-2. As PZT-2 deforms downwards, the membrane opens the path of the flow and allows the medicine fill up the pressure chamber. The membrane is also able to block the flow when PZT-2 deforms upwards. The reservoir module is designed to store the medicine to be injected and apply a constant pressure to the liquid medicine. The module has a syringe and tubing connected to the inlet aperture. It not only provides the medicine needed by the microsystem and also drives the medicine towards the pressure chamber.

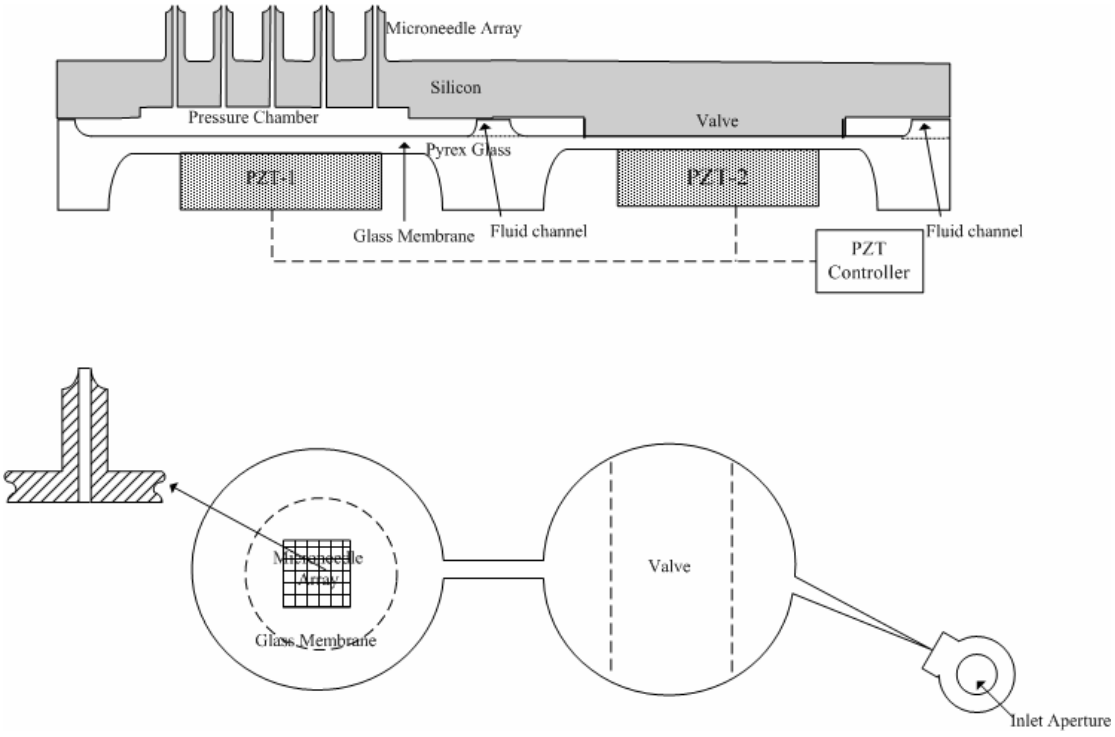

Figure 5.1 Schematic drawing of a microchip for drug injection

The curved tip part of hollow microneedle array was designed to have less interfacial area during the insertion. Less interfacial area reduces the required insertion force for tissues. The number of microneedles in an array and the diameter of the inner microchannel would be determined by specific delivery requirements. The glass, Pyrex 7740, was used to fabricate reservoirs and membrane. The thermal extension of Pyrex 7740 is similar to silicon. Therefore, this type of glass was chosen to bond with silicon microneedle array to reduce boning stress in the microsystem. Due to the transparent property, glass is a proper choice for easy observation. Moreover, the glass components in microsystems have the potential to enable the optical applications in biological area. Glass with the properties of chemical inertness and thermal stability enable it to be an idea material in medial and biological applications. The microsystem needs be actuated in a controlled way in order to deliver a desired mount of drug. PZT actuator was designed to actuate a glass membrane for drug injection purpose. A PZT-glass membrane has been used in the micropump for precise droplet control. Utilize the PZT-glass actuation technique, femtoliter droplets can be delivered for DNA mass spectrometry [105]. The working temperature of a drug delivery system has a limitation because high temperature can influence the properties of certain drugs. Hence, the thermal driven actuation may not fulfill the requirements of the drug delivery system.

5.1.1 Design of Flow

The design of fluid requirement was specified for delivery *m* μL of a liquid dose in *t* seconds. To achieve the delivery specification, the fluid flow and actuation mechanism were taken into consideration for design of the microsystem.

Figure 5.2 shows the fluid flow at a volumetric flow rate *Q* through a microneedle cavity of circular cross section with the diameter *D* and length *L* ,causing the pressure drop $\Delta p = p_1 - p_2$. p_1, the actuation pressure, is the pressure created by pumping mechanism. The output pressure, p_2, is the average resistance offered by the tissues under injection in terms of pressure. The resistance to flow is due to the viscous drag on the walls of the microneedle. The actuation mechanism has to overcome this viscous drag in order to deliver drug. Because of the viscous drag, the velocity profile of the injected fluid is not uniform through out the cross-section microneedles.

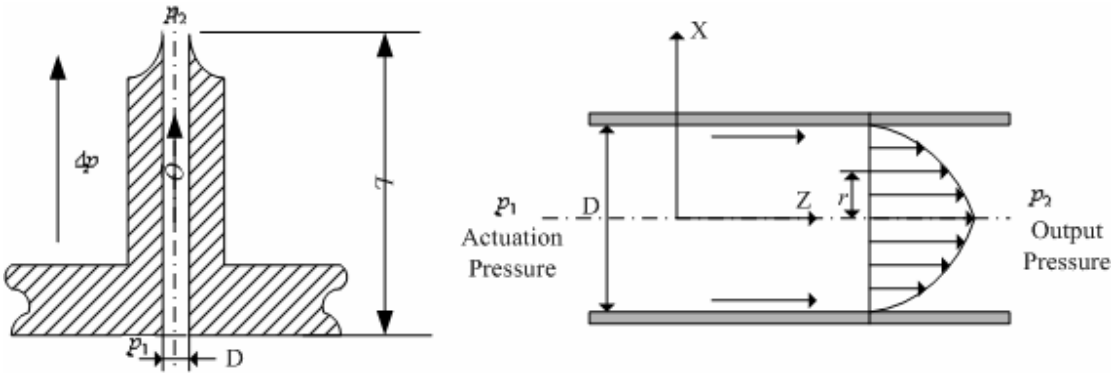

Figure 5.2 Schematic channel cross section of the microneedle.

The liquid can be considered to be continuous even in very small devices and geometries. Hence, well-established continuum approaches for fluid mechanics would be used in the flow analysis of the microneedles. Three primary conservation laws which are used to model thermofluid dynamics problems are conservation of mass, momentum, and energy. The fluid in the microneedle channel is considered as an incompressible, Newtonian, isotropic, and Fourier conducting material. Under these conditions, the generalized Navier-Strokes equation [106] was applied for the flow analysis to derive the press drop in the microchannel.

$$\rho\left(\frac{\partial V_z}{\partial t}+V_x\frac{\partial V_z}{\partial x}+V_y\frac{\partial V_z}{\partial y}+V_z\frac{\partial V_z}{\partial z}\right)=\rho F_z-\frac{\partial p}{\partial z}+\mu\left(\frac{\partial^2 V_z}{\partial x^2}+\frac{\partial^2 V_z}{\partial y^2}+\frac{\partial^2 V_z}{\partial z^2}\right) \qquad \text{E- 5.1}$$

where V_x, V_y and V_z are the velocity of the fluid in x ,y and z direction, p is pressure, μ is the viscosity, ρ is the density, and F_z is the body force. At large length scales, F_z is often taken to be gravity. Because of the cube-square scaling, the effect of gravity in small systems is usually negligible. To simplify the analysis, the flow in the microneedle was approximated to be isothermal flow of incompressible, isotropic, Newtonian, and laminar flow through a channel of a constant circular cross section, as shown in Figure 5.2. The boundary conditions were set to be no-slip at the wall in the direction parallel to the flow (z) and no penetration through the wall in the directions normal to the flow (x,y). Under these assumptions, the Equation 5.1 can be simplified to:

$$0=-\frac{\partial p}{\partial z}+\mu\left(\frac{\partial^2 V_z}{\partial x^2}+\frac{\partial^2 V_z}{\partial y^2}\right) \qquad \text{E- 5.2}$$

Changing Equation 5.2 from a rectilinear to a cylindrical coordinate system, with the relation function: $r^2 = x^2 + y^2$, the equation 5.2 can be re-written as:

$$\frac{d^2V}{dr^2} + \frac{1}{r}\left(\frac{dV}{dr}\right) = \frac{1}{\mu}\frac{dp}{dz} \qquad \text{E- 5.3}$$

Integrating the both side of equation 5.3, the solution is

$$V(r) = \frac{(D/2)^2 - r^2}{4\mu}\left(-\frac{dp}{dz}\right) \qquad \text{E- 5.4}$$

By integrating velocity (*V(r)*) over the area, flow rate can be derived as:

$$Q = \int_{x^2+y^2=\frac{\pi D^2}{4}} V(r) * \pi r^2 = \frac{\pi D^4}{128\mu}\left(-\frac{dp}{dz}\right) \qquad \text{E- 5.5}$$

The pressure gradient is assumed to be linear along the length of the microneedle. Therefore, the pressure drop could be written as:

$$\Delta p = Q * \left(\frac{128\mu}{\pi D^4}\right) * L \qquad \text{E- 5.6}$$

The flow rate Q is equal to m/t μL/sec according to the design requirement of delivery m μL of a liquid dose in t seconds. Hence the pressure drop would be represented as:

$$\Delta p = \frac{m}{t} * \left(\frac{128\mu}{\pi D^4}\right) * L \qquad \text{E- 5.7}$$

The cavity dimension of the microneedle is closely related to the amount of drug delivery. In order to accurately control the amount of drug delivered, the diameter of the inner channel has to be dealt with in the design. Due to the similar microfluidic properties of most of drug and water, water properties were used for the design of the microneedle diameters. The density of

water is 1000 Kg/m^3, and the viscosity of water is 1.002e-3 N*s/m^2 at room temperature. The microsystem was required to be able to deliver 100 μL in 60 seconds. The length of inner channel of the microneedle was assumed to be 400 μm. The number of microneedle N in an array is 100 (10 by 10). Equation 5.8 presents that diameter (D) of the microneedle as a function of flow rate (Q).

$$D = \left(\frac{128 * \mu * Q * L}{\pi * \Delta p * N} \right)^{0.25} \qquad \text{E- 5.8}$$

Figure 5.3 shows the plot as a function of diameter and flow rate with the assumptions. The curves of diameters vs. pressure drop are saturated after the drop of pressure reaches a certain level. The diameter of lumen increased with the increased flow rate at certain values of pressure drop. The curves in Figure 5.3 are becoming flat with the increasing of the pressure drop. The region of flattened lines illustrates that the diameter is not very sensitive to the variation of the high pressure drop. The smaller diameter is required for the bigger pressure drop at the desired flow rate.

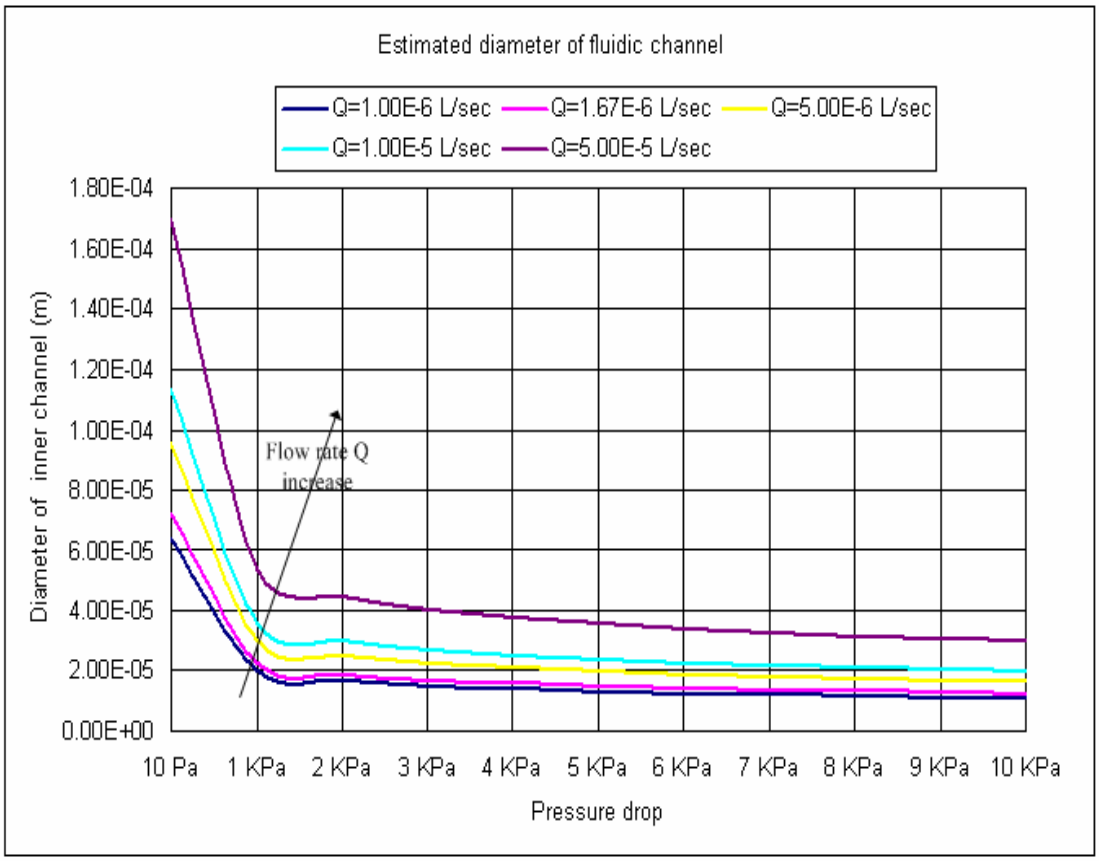

Figure 5.3 Estimation of inner channel diameter of the microneedle with the variation of pressure drop at different flow rates

The designed diameters of the microneedles can be determined at the saturated region of diameter vs. pressure drop curves. The slope of the diameter vs. pressure drop curve presents the variation of the diameter with pressure drop. After the pressure drop reaches certain value, the variation of diameter with pressure drop is negligible. The value of the pressure drop was defined as the saturation pressure drop. In the calculation, the condition for saturation of the diameter vs. pressure drop curve was defined as the value of the variation of diameter per pressure drop less than 10^{-3} μm/Pa. The value of the diameter necessary for meeting these criteria can be calculated by equation 5.9:

$$\left|\frac{\partial D}{\partial \Delta p}\right| \le 10^{-9}(m/Pa)$$

$$\frac{\partial D}{\partial \Delta p} = -0.25 * \left(\frac{128 * \mu * Q * L}{\pi * N}\right)^{0.25} \Delta p^{-1.25}$$

$$0.25 * \left(\frac{128 * \mu * Q * L}{\pi * N}\right)^{0.25} \Delta p^{-1.25} \le 10^{-9} \qquad \text{E- 5.9}$$

$$\log(\Delta p) \ge \frac{\left(9 + \log\left(0.25 * \left(\frac{128 * \mu * Q * L}{\pi * N}\right)^{0.25}\right)\right)}{1.25}$$

Figure 5.4 shows the saturated pressures at different delivery flow rates under the condition of $\left|\partial D / \partial \Delta p\right| \le 10^{-9}$. The saturated pressure drop is at 4023 Pa corresponding to the desired flow rate at 1.67 μL/sec. Increased saturated value of pressure drop was obtained at increased desired flow rate.

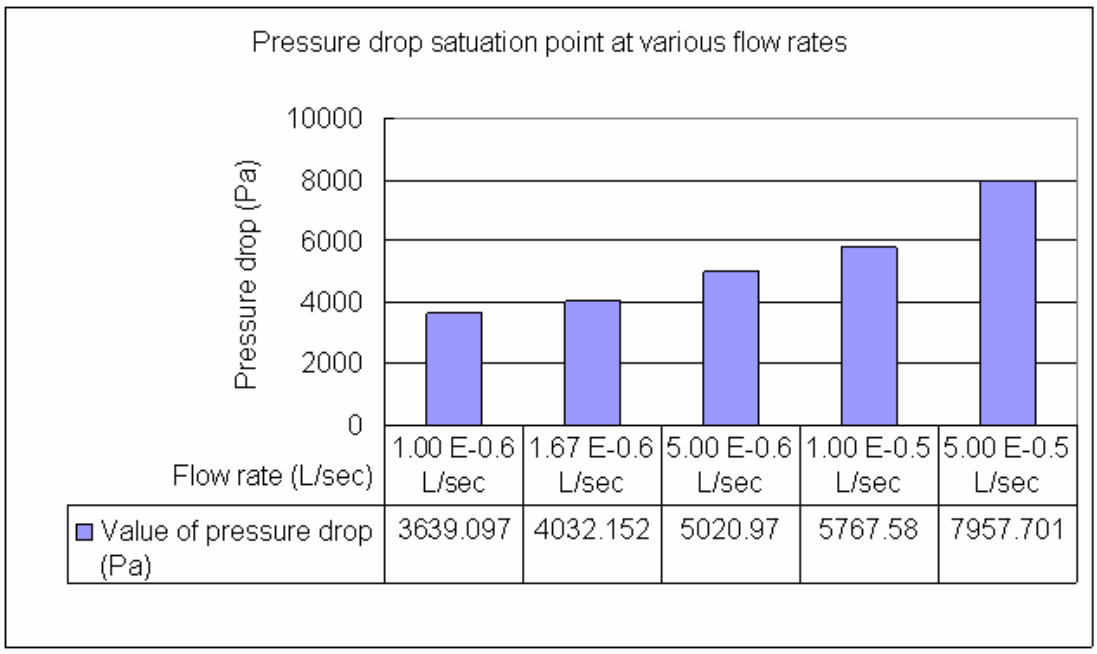

Figure 5.4 Saturated values of pressure drop for different flow rates

The diameter of inner channel is determined by the desired flow rate and the saturated pressure drop, as shown in Figure 5.5. The bottom-right region which is defined by the desired flow rate and the saturated pressure drop are satisfied with the delivery requirement. With the assumption of constant value for output pressure, the flow rate will be linearly related to the actuation pressure. From the Figure 5.5, it was found that those diameters with values less than 16 μm met the designed flow rate at 1.67 μL/sec under the region of the saturated pressure drop. However, higher actuation pressures which are greater than 10 KPa are required for the microneedles with diameters less then 12 μm. Higher actuation pressures will accompanied with additional issues of membrane broken and leakage. Therefore, the reasonable designed diameters should be in the range of 14 μm to 16 μm.

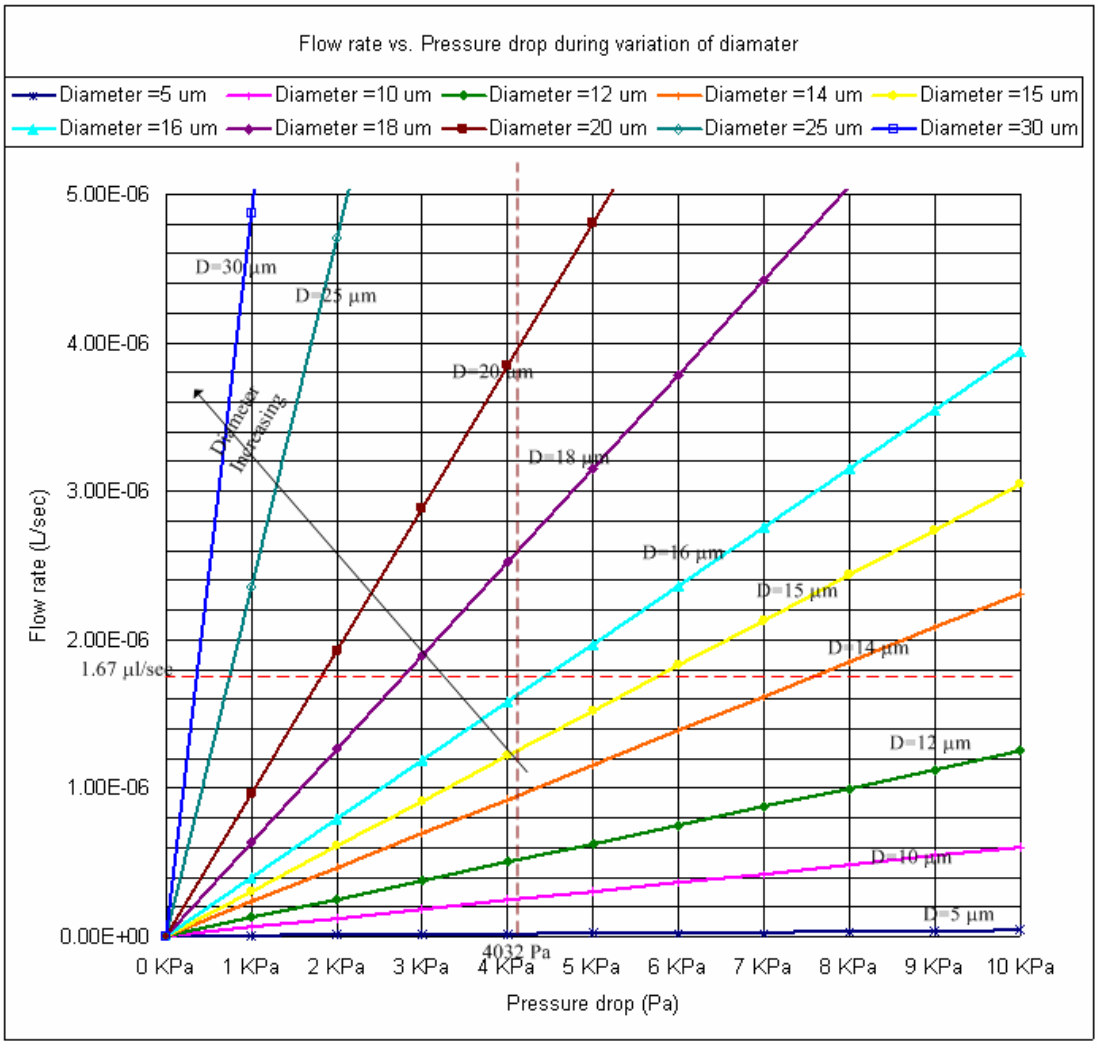

Figure 5.5 Variation of diameters at various pressure drops for the desired flow rate

The calculated diameter for the designed flow rate 1.67 µl/sec using array with 100 microneedles when the value of pressure drop was set at 5 KPa is 15.2 µm. The curve of the estimated diameter of inner channel vs. flow rate at a pressure drop 5 KPa was plotted in Figure 5.6. This figure shows that the estimated diameter increases with the flow rate. The value of the diameter corresponds to the results in Figure 5.3. The figures of flow analysis illustrate that the diameter must have certain value at certain actuation pressure for the desired flow rate. Hence,

the actuation pressure is additional parameter which will eventually affect the design of the diameter.

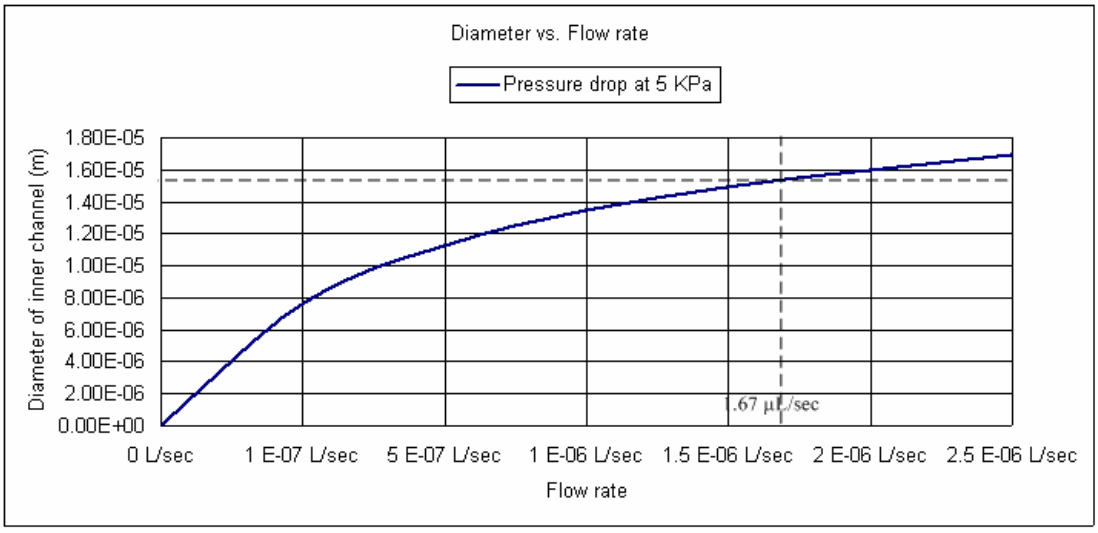

Figure 5.6 Estimation of inner channel diameter with the variation of flow rate at pressure drop at 5 KPa

5.1.2 Design of Actuation Mechanism

The pumping elements are important for the control of delivery amount in the microsystem. To keep high pressure in the chamber, the design of the fluidic channel from inlet to valve was based on the diffuser/nozzle principles [107]. The design geometry of fluid channel was shown in Figure 5.7, where L_d is the diffuser length, γ is the divergence angle, and W_1, W_2 are the neck width for inlet and outlet respectively. The geometric dimension of the channels has the valve of 3 mm for L_d, 60 μm for W_1, 380 μm for W_2, and 6^o for γ. The designed flat-wall geometry of fluid feed channel allows increasing the pressure in the cavity during the injection because the expanding duct has a lower pressure than the straight duct and a converging duct for the same velocity [108][109][110][111].

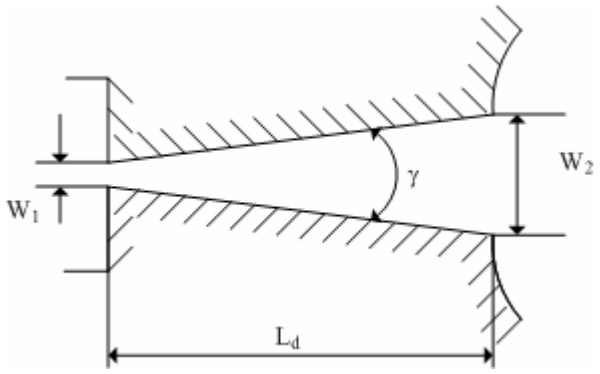

Figure 5.7 Schematic drawing of the channel geometry

The displacement micropumps are typically used to deliver the fluid with the flow rates between 10 μL/min and several milliliters per minute. For flow rates less than 10 μL/min, alternative dynamic pumps or nonmechanical pumps are needed [99]. In this research, the dynamic delivery of fluid was done with PZT deflection in order to fulfill the flow rate requirement of 100 μL/min. In order to deliver the accurate amount fluid, the two PZT discs were designed to work simultaneously, as shown in Figure 5.8. The inlet aperture is connected with a syringe, which is applied adjustable pressure to maintain the flow toward the microneedle. In the middle chamber, a valve is designed to forbid the back-flow of the drug through microneedle.

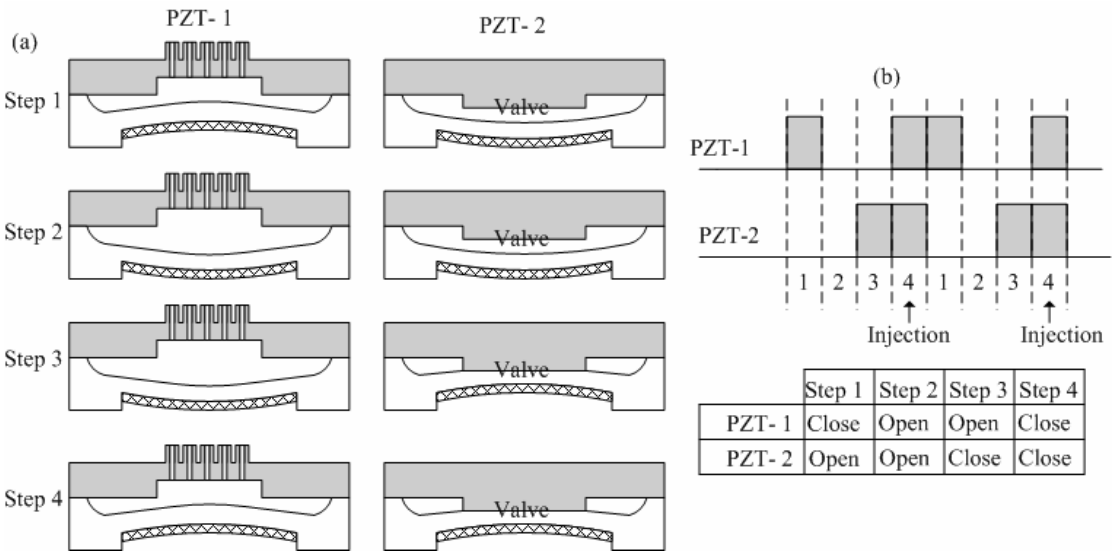

	Step 1	Step 2	Step 3	Step 4
PZT- 1	Close	Open	Open	Close
PZT- 2	Open	Open	Close	Close

Figure 5.8 Schematic of cycle of PZT actuation

Since the fluid is driven by the external syringe into the pressure chamber and finally injected into targeted tissues, two PZT actuators have to be synchronized to work collaboratively in order to inject dose precisely. As indicated in Figure 5.8 (a), a cycle of injection consists of four steps. In Step 1, PZT-2 deforms downward and opens the valve. Due to the external pressure generated by the syringe, the medicine could flow through the valve and fills up the pressure chamber. In Step 2, PZT-1 deforms downwards to allow more doses flowing into the pressure chamber, as the valve keeps open. During Step 3, the valve closes as PZT-2 deform upwards and block the flowing channel. In the last step, the glass membrane deforms upwards and injects the medicine into tissues. Due to the close valve, the drugs can only be injected and would not flow backwards into the syringe. The synchronization of the PZTs is demonstrated in Figure 5.8 (b). It is worth noting that, in Step 2, due to the PZT-1 downwards deformation and consequent pressure drop in the pressure chamber, the medicine already injected into tissues

would have flow back into the pressure chamber if there was not external syringe. The external syringe applies a constant pressure and only allows the medicine to flow in the direction of the injection, when the valve is open.

The exact volume of flow in the chamber would be pumped out corresponding to the deflection of glass membrane caused by the deflection of the PZT from an applied voltage. The membrane displacement distance could be measured by a Michelson interferometer [112][114]. Figure 5.9 shows the deflection of the PZT and glass membrane. The stroke volume would be estimated with the analysis of the deflection.

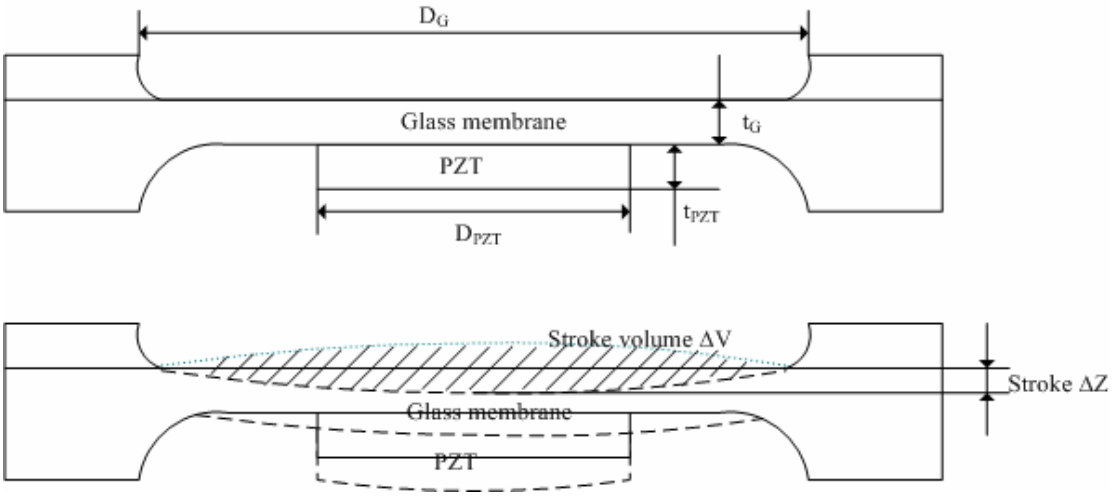

Figure 5.9 Schematic drawing of PZT and glass membrane deflection

The membrane deflection is assumed to follow the deflection function of a thin circular plate. Figure 5.10 shows the membrane deflection.

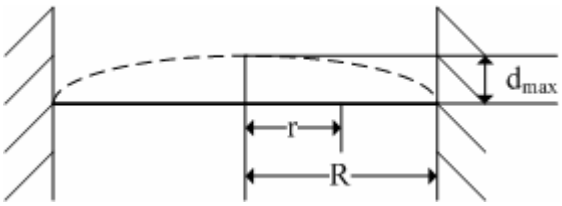

Figure 5.10 Schematic drawing of membrane deflection

The deflection function is presented in the equation as follow:

$$d(r) = d_{\max}\left[1-\left(\frac{r}{R}\right)^2\right]^2 \qquad \text{E- 5.10}$$

The volume of flow in every stroke was approximately calculated by the deflection in equation E-5.10. According to the deflection schematic in Figure 5.9, the approximate stroke volume would be presented in the equation as follow:

$$\Delta V = 2\times\int_0^{2\pi}\int_0^{R} d_{\max}\left[1-\left(\frac{r}{R}\right)^2\right]^2 r\,dr\,d\varphi = \frac{2\pi}{3}d_{\max}R^2 = \frac{\pi}{6}\Delta Z * {D_G}^2 \qquad \text{E- 5.11}$$

where ΔV is the volume flow per stroke, ΔZ is the deflection in a stroke, D_G is the diameter of glass member. The diameter of glass membrane was designed at 6 mm. The thickness of glass membrane was designed at 200 μm. At low frequency of *f*, the flow rate *Q* could be estimated by the equation: $\Delta V * f$.

The stroke deflection ΔZ is caused by the deflection of PZT, which is linearly dependent on the applied voltage U. For the circular shape with vibration along perpendicular axis, the deflection of stroke ΔZ can be approximately estimated as the deflection of PZT [115] . Equation 5.12 reveals the deflection under the applied voltage.

$$\Delta Z \approx \frac{d_{31} * U * D_{PZT}^2}{8 * t_{PZT}^2} \qquad \text{E- 5.12}$$

where d_{31} is the piezoelectric constant, D_{PZT} is the diameter of PZT, and t_{PZT} is the thickness of PZT. Equation 5.11 was rewritten by substituting ΔZ using equation 5.12. Hence, the volume flow per stroke can be estimated using the fluid pumped out by the deflection of PZT and glass membrane.

$$\Delta V \approx \frac{\pi d_{31} * U * D_{PZT}^2 * D_G^2}{48 * t_{PZT}^2} \qquad \text{E- 5.13}$$

Table 5.1 lists the parameters of the actuator design. A PZT with high piezoelectric constant is typically used in pumping systems to achieve sufficient deflection in the membrane. In order to estimate the volume flow per stroke, the parameters of properties for a PZT disc were selected from common applied materials, as list in Table 5.2. The piezoelectric constant was selected at 250E-12 C/N.

Table 5.1 Design of the actuator

Material of membrane	glass
Material of actuator	PZT
Membrane diameter D_G (mm)	6
Membrane thickness t_G (mm)	0.1
PZT Disc Diameter D_{PZT} (mm)	3
PZT Disc thickness t_{PZT} (mm)	0.2
Operation voltage Range U (V)	$\pm$100

Table 5.2 Properties of common PZT [99]

Material	d_{31} (10^{-12}C/N)	d_{33} (10^{-12}C/N)	Relative Permittivity ε_τ
PZT	-60~-270	380-590	1700

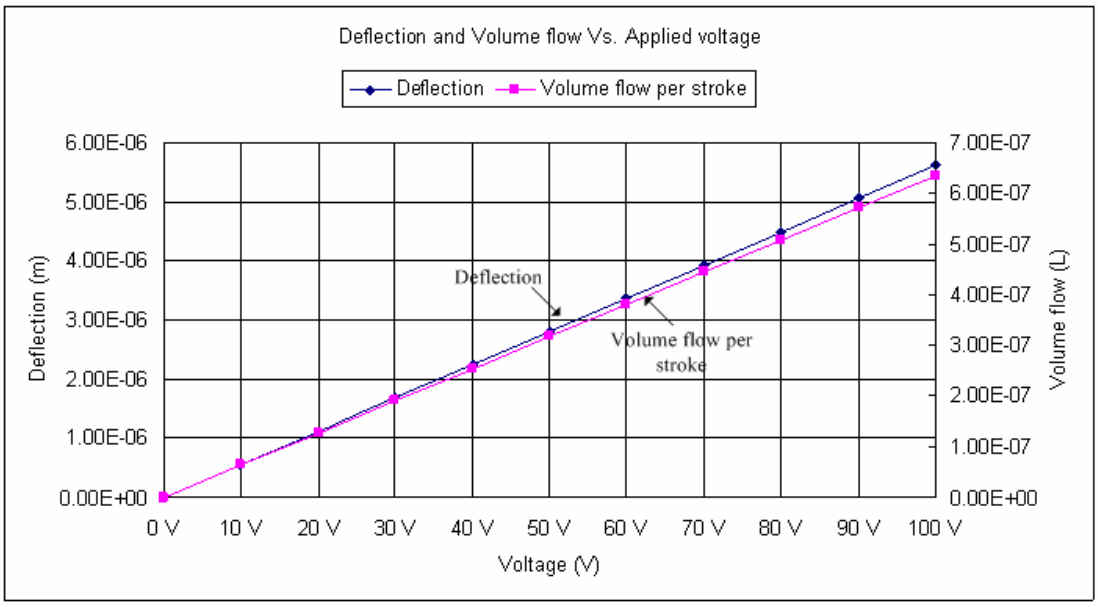

Figure 5.11 Estimated membrane deflection and flow rate per stroke

The deflection of membrane and the volume flow are both linearly dependent on the applied voltage. Figure 5.11 shows the qualitative values of the volume flow and deflection vs. applied voltage. The estimated maximum deflection of the membrane is 5.6 μm. The value is reasonable for the designed dimensions of the actuator. The maximum deflection of a membrane is required to be less than one percent of the PZT thickness for a PZT pumping system [99].

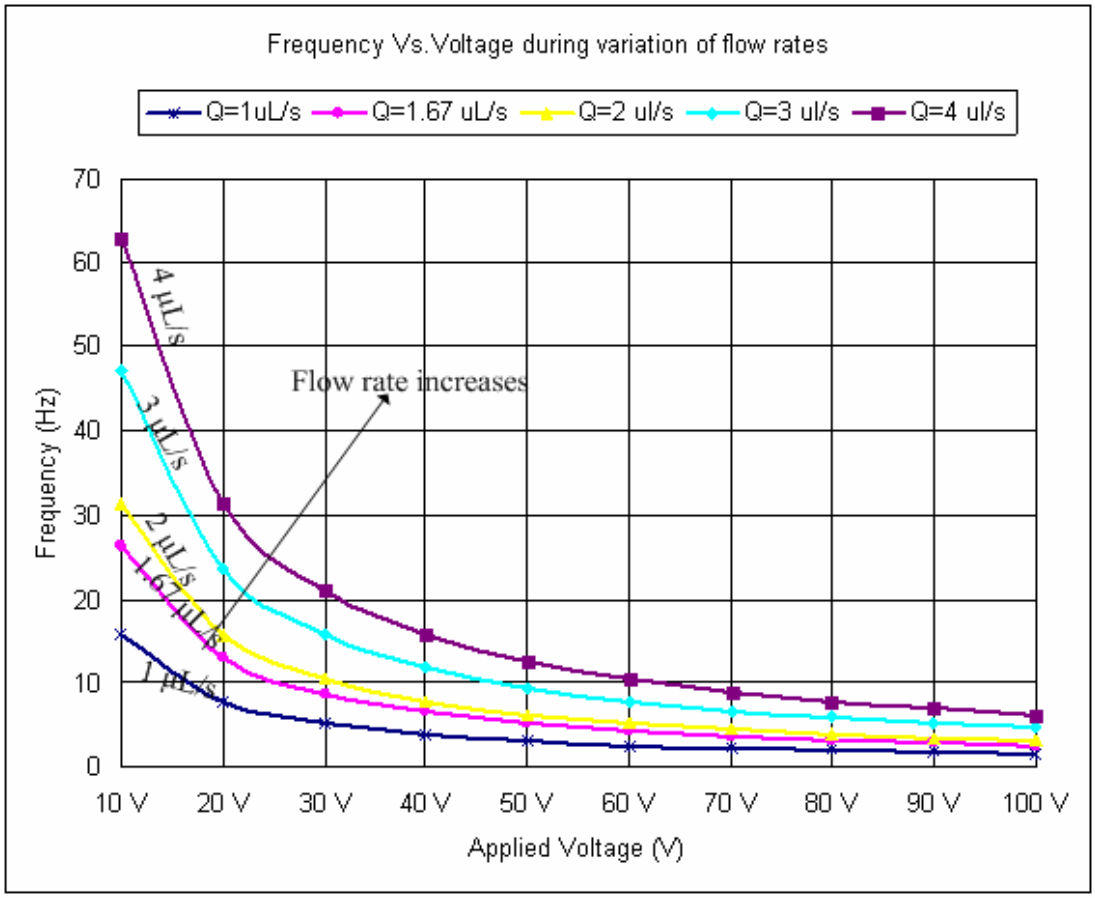

Figure 5.12 Actuated frequencies vs. applied voltages during the variation of flow rate

To obtain the designed flow rate using the microneedle array, the volume flow per stroke (ΔV) , pumping frequency (f) and flow rate (Q) need to satisfy the relation: Q=ΔV*f. There are innumerable solutions of this equation. Figure 5.12 shows the variation of the frequency along the applied voltage. For example, when the applied voltage was set at 50 V, the volume flow per stroke was 2.18 E-7 L at the designed flow rate 1.67 µL/s. Corresponding to this voltage and the volume flow per stroke, the frequency needed to be set at 5 Hz. The frequency dramatically decreases with the increased voltage, as shown in Figure 5.12. The PZT may not work properly

at a low applied voltage because a high frequency could cause an incomplete deflection of a membrane [112].

5.2 Experimental Methods

The microsystem consists of two parts, a hollow microneedle array fabricated on a silicon wafer and a reservoir and channels etched in a Pyrex glass wafer. Each part was fabricated individually, and the two components were bonded together using anodic bonding.

5.2.1 Microfabrication Process of Hollow Microneedle Array

The isotropic etching in inductive coupled plasma (ICP) etcher and DRIE were combined to achieve arrays of microneedles with high aspect ratio structures. The isotropic etching process with SF_6/O_2 gases in high density plasma etching was conducted in silicon etching to form the structure of needle tips. With the combination of isotropic and anisotropic dry processes, hollow microneedle arrays with high density and relatively minor base dimension was achieved.

The overall hollow needle fabrication process is shown in Figure 5.13. Four-inch p-type double-side polished silicon wafers with 450~500 μm thickness and (100) orientation were used in the microneedle array fabrication. The fabrication procedure for the hollow needle array is illustrated in Figure 5.13 (a) - (s). Isotropic silicon etching was conducted using SF_6/O_2 gases

in the STS inductively coupled plasma (ICP) etch tool with a photoresist mask patterned in standard photolithography process (Figure 5.13 (a)-(c)). A silicon oxide layer with thickness of 2 μm was thermally grown on the wafers (Figure 5.13 (d)) in a thermal oxidation furnace at 1050 ^{o}C after the removal of photoresist from the isotropic etching structure. A photoresist layer (AZ9260, 1500 rmp) was coated onto the structural surface (Figure 5.13 (e)), and arrays of dots were patterned aligning with the former isotropically etched structure (Figure 5.13 (f)). The patterned photoresist layer was used as a sacrificial layer to pattern the silicon oxide layer which was etched away in RIE with CF_4/O_2 gases (Figure 5.13 (g)). The patterned photoresist was then removed in acetone and rinsed in DI water.(Figure 5.13 (h)) Silicon dioxide layer on the backside of wafer was patterned with the exposed squares area in standard photolithography with alignment to the topside array of dots(Figure 5.13 (i)-(k)). Subsequently, another photolithography process was carried out to define inner holes beginning at the coating of thick photoresist (AZ 9260, 1000 rmp) in the front surface. Both the photoresist and silicon oxide layers were patterned in this photolithography process (Figure 5.13 (l)-(m)). With the double layer masks consisting of photoresist and silicon oxide layer, the DRIE was carried out to etch lumen in silicon substrate using BOSCH process (Figure 5.13 (n)). The photoresist mask was removed when the desired depth of the lumen was reached ~300 μm (Figure 5.13 (o)). Therefore, the outside shape and lumen were etched simultaneously with the only oxide mask in the DRIE process, resulting in the formation of hollow needle arrays (Figure 5.13 (p)). Finally, the reservoir was etched using the BOSCH process with a blank wafer glued onto the

side of fabricated needle as a support substrate in the STS ICP etcher (Figure 5.13 (r)). After removing the residual silicon oxide in HF, the fabricated hollow needle array with reservoir was complete (Figure 5.13 (s)).

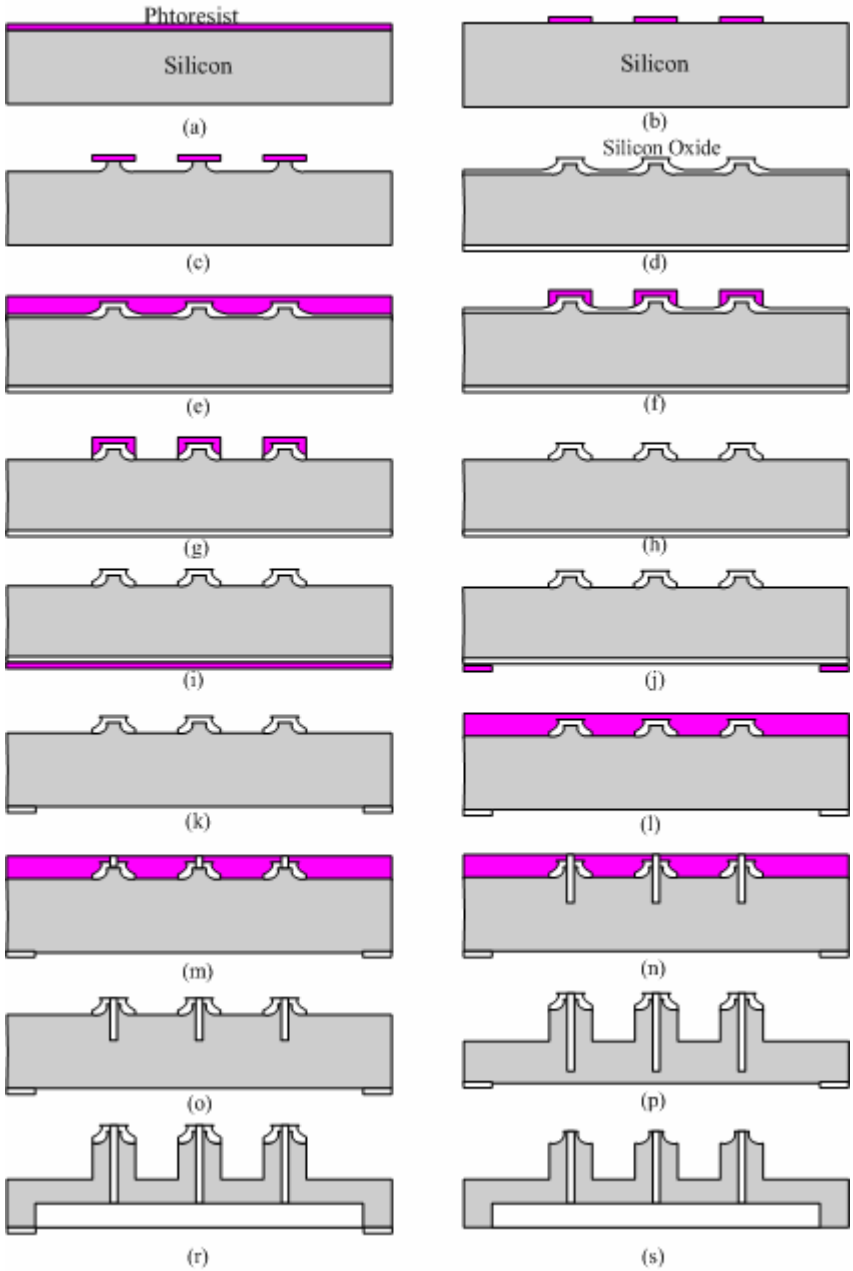

Figure 5.13 A schematic draw of fabrication process used in making the hollow microneedle array. The process consists of (a) spin-coating of photoresist (b) patterning in the photolithography (c) isotropic etching of outside shape for needle tips by STS ICP

equipment with mask patterned in photolithography (d) thermal growth of a silicon oxide layer after removal of photoresist mask (e) spin-coating of thick photoresist (f) patterning of the photoresist layer (g) patterning of top silicon oxide layer in outside shape of needle in RIE (h) remove of photoresist in acetone (i) spin-coating on the backside of silicon wafer (j)pattern the photoresist in squares (k) etching back oxide layer for fabrication of reservoirs (l) coating of a photoresist (m) pattering of the inner channel on the photoresist and oxide layer (n) lumen etching by DRIE (o) removal of photoresist (p) outside shape of needle and lumen etching by DRIE after removal of photoresist (r) backside reservoir etching by DRIE (s) removal the oxide layer resulting in the fabricated hollow needle array.

5.2.2 Microfabrication Process of Glass

A 500 μm thick Pyrex glass wafer was used to fabricate microchannels and the pressure chamber. The glass wafer was isotropically etched in concentrated HF solution to fabricate structures on the substrate. A differential double-side etching technique was applied in the process to etch both side of wafer with different depths. The outlet and inlet apertures were drilled after the fluidic channels and pressure chambers have been etched in the glass. The fabrication procedure for the glass structure is illustrated in Figure 5.14 (a) - (h). A 500 nm thick polysilicon was deposited onto the glass surface by LPCVD. (Figure 5.14 (a)) The standard photolithography was then carried out and the pattern in mask was transferred to the photoresist layer. (Figure 5.14 (b)) Reactive ion etching was conducted to etch the top polysilicon layer using CF_4/O_2 (Figure 5.14 (c)) followed by the wet etching of glass in concentrated HF solution to fabricate the membrane (Figure 5.14 (d)). Wet etching continued until a depth ~300 μm was reached. Subsequently, the wafer was rinsed and baked in a pressure chamber and fluidic channels were etched from the backside of the glass wafer using polysilicon as the mask layer.

The patterns of chamber and channels were transferred onto the photoresist layer in photolithography (Figure 5.14 (e)). The polysilicon layer was then etched with RIE (Figure 5.14 (f)). After the polysilicon mask was patterned, the HF wet etched was carried out to etch double side opening areas including the pressure chamber, fluidic channel and the membrane until the depth of the etched chamber was 50 μm (Figure 5.14 (g)). Finally, the polysilicon layer was removed in KOH solution, resulting in the fabricated glass component (Figure 5.14 (h)).

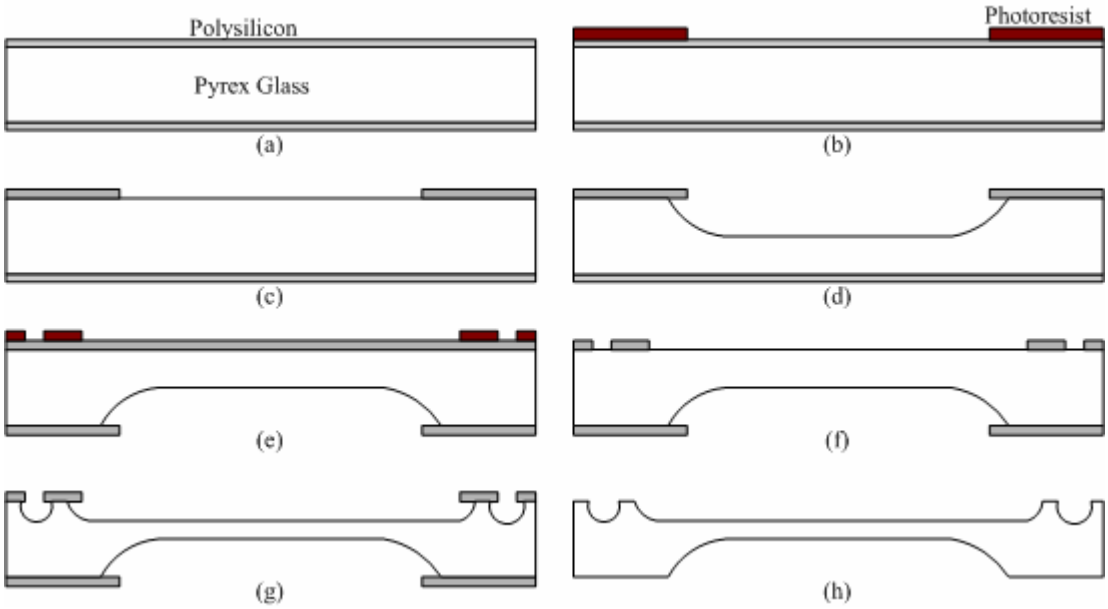

Figure 5.14 A schematic draw of fabrication process used in etching Pyrex glass (a) deposition of polysilicon (b) pattern of photoresist (c) RIE etching the polysilicon layer (d) HF wet etching of glass (e) pattern of photoresist on the backside of wafer (f) pattern the polysilicon layer (g) HF wet etching of glass channel and pressure chamber (h) removal of polysilicon in KOH.

5.2.3 Combination Process of Isotropic Etching and Deep Etching

In Chapter 3, the SF_6/O_2 isotropic etching was conducted to fabricate solid silicon microneedles. The height of the isotropically etched microneedle highly depends on the pattern dimension of a

mask and the etching parameters. In the experiments of characterization, the maximum height of microneedles is ~120 μm under the square mask with the dimension of 80 μm. To achieve high aspect ratio microneedle structure, the process which combined isotropic etching and anisotropic etching was developed to fabricate microneedles. The shapes of the needle tips were generated using isotropic etching with SF_6/O_2 gases excluding the passivation step in STS ICP etcher. The BOSCH process was used to fabricate the erratic structure of needles. The microneedles with high aspect ratio were fabricated with the combination of isotropic etching and anisotropic etching in the STS ICP etching tool. A microneedle with ~ 300μm in height was achieved using a mask of 80 μm in diameter [116]. Figure 5.15 shows the fabricated microneedle arrays using the combined process. The depth of the deep etching process determined the height of microneedles. The depth of anisotropic etching in BOSCH process was controlled by the etching time. Figure 5.15 (a) and (b) show the SEM pictures of microneedle structure fabricated in combination process with different deep etching time. The time of deep etching was 40 minutes and 100 minutes in Figure 5.15 (a) and in Figure 5.15 (b) respectively. The height of isotropic etched tips was ~50 μm.

A silicon oxide layer instead of photoresist layer was used as mask in the fabrication because of the isotropic etching would etch away the photoresist layer as well. Theoretically, the BOSCH process etch depth is limited by the wafer layer. However, a small percentage of microneedles was etched off when the etch depth exceed 400 μm, and the oxide masking layer was found

partially pilled off during the deep etching. Therefore, etching depth of the microneedle was designed as 300 μm at maximum. With the isotropic etched tips, the microneedles would require less insertion force than the pillars fabricated in BOSCH process during insertion.

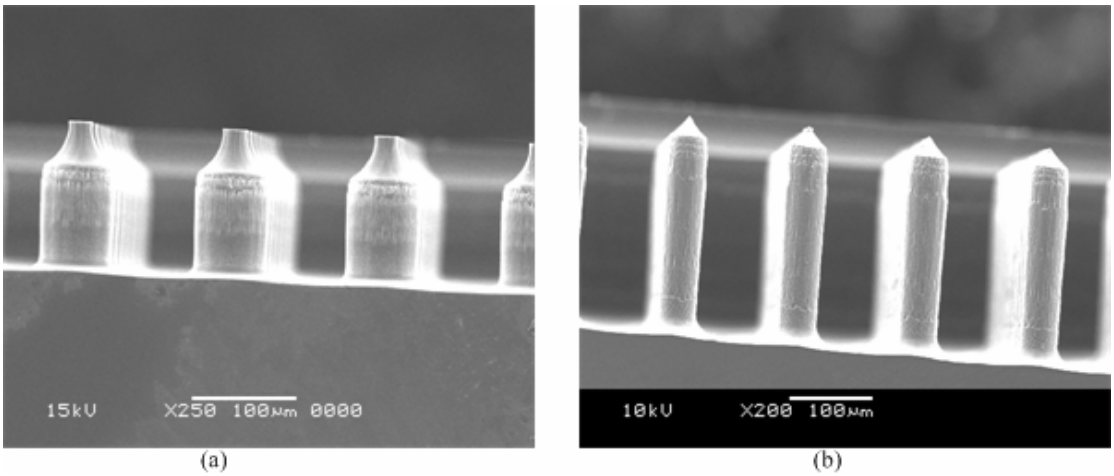

Figure 5.15 SEM micrograph of microneedle array fabricated in combined process

5.2.4 Glass Deep Wet Etching

The glass deep wet etching was investigated to fabricate glass component of the microchip. The etching conditions including etchant and mask layers, and etching results (including etching rate and surface roughness) were characterized in these experiments. 4-inch Pyrex glass (Corning 7740) and soda lime glass wafers were used in these experiments for the characterization of etchants. The initial value of surface roughness for the tested glass wafers was less than 1.5 nm. The wafers were cleaned in piranha solution (H_2SO_4: H_2O_2 2:1) at 120 ^oC for 20 minutes. After rinsing in DI water and spin-drying, the wafers were baked in an oven, at 120 ^oC, in a N_2 environment for 30 minutes. The highly concentrated HF (49%) and HCl (37%)

were used for glass etching with photoresist (AZ9260), Cr/Au, PECVD amorphous silicon, and LPCVD polysilicon masks, respectively. The wet etching process was performed in a Teflon container using magnetic stirrer. The roughness of the surface was analyzed using a profilometer (Alfa-step KLA Tencor) and AFM (PSIA XE-100).

Four types of etchants including concentrated HF and HF mixed with HCl at the volume ratio of 10:0.5, 10:1 and 10:1.5, were investigated in these experiments. Two types of glasses (Pyrex Corning 7740 and Soda Lime), which are widely used in MEMS field, were used. Glass is a mixture of oxides with various types and percentages. The main properties of glass are mostly decided by the added the oxide components. Table 5.3 shows the composition of the Pyrex 7740 and soda lime glass. The concentration HF etchant is typically used for glass etching. Some oxides such as CaO, MgO or Al_2O_3 generate insoluble products in HF solution during the etching.

$$CaF_2 \leftrightarrows Ca^{2+} + 2F^-,\ MgF_2 \leftrightarrows Mg^{2+} + 2F^-,\ AlF_3 \leftrightarrows Al^{3+} + 3F^-,$$

These insoluble products would be deposited on the generated surfaces and act like a masking layer. As a result, after etching, the surface became non-planar with a lot of defects. By adding HCl, the insoluble products would become soluble products:

$$CaF_2 \rightarrow CaCl_2,\ MgF_2 \rightarrow MgCl_2,\ AlF_3 \rightarrow AlCl_3$$

Theoretically, by adding HCl, the quality of etching process can be improved. Therefore the etchants, HF solution with different amount HCl, was mixed to investigate the surface property and etch quality of glass.

Table 5.3 Composition of Pyrex Corning 7740 and Soda lime

Glass	Composition
Pyrex 7740	SiO_2 81%, B_2O_3 13%, Na_2O 4%, *Al_2O_3 2%*
Soda lime	SiO_2 72.3%, Na_2O 13.7%, *CaO 8.8%, MgO 4%,* Fe_2O_3 0.12%, *Al_2O_3 0.1%*

The masking layer is a big issue in deep glass etching because the defects such as pinhole and mouse bit often occur in the HF wet etching. Certain masking layers could not resist long exposures to concentrated HF etchant. Four masking layers were tested in the etchants for glass deep wet etching in the experiments for characterization of etching time. The masking layers were photoresist (AZ9260), Cr/Au, PECVD amorphous silicon, and LPCVD polysilicon. Channels and cavity were patterned to characterize the etching time and quality. Thick photoresist AZ9260 (from Clariant) was used as masking layer. The thickness of the layer was 7.5 μm. A Cr/Au layer with thickness of 50 nm/800 nm was deposited by E-beam evaporator (CHA). The PECVD amorphous silicon layer was deposited on the PECVD-Technics equipment at 300 ^oC, RF power 60 W, using SiH_4/Ar gas. The thickness of the amorphous layer was 0.7 μm. The layer was annealed 4 hours at 400 ^oC for reduction of the residual stress. The polysilicon layer was deposited in a Tystar furnace at 530 ^oC, for 2.5 hours in the LPCVD process. The thickness of the polysilicon layer was 400 nm.

5.3 Experimental Results

5.3.1 Fabricated Hollow Microneedle Array

Microneedle arrays with a lumen diameter of 30 μm, height of ~250 μm, and center-to-center distance of 150 μm were fabricated using a previously developed process [117]. Figure 5.16 shows the SEM picture of fabricated microneedle array taken at different positions. The step of isotropic etching was ~ 15μm, which was clearly shown in the Figure 5.16 (c). The height of the isotropic etching was limited to the second photoresist coating on the structural surface. (Figure 5.16 (e)) In order to carry out the next pattern of inner holes, the photoresist was thick enough to cover the edge of the isotropic etched structure. However, the thickness of photoresist layer coating in drop and spin approach was limited by the rotating velocity and the viscosity of used photoresist. In the experiment, the photoresist used was AZ9260; and coating speed was set as 1000rmp. The thickness of photoresist at the condition was achieved ~ 18 μm on the etched surface.

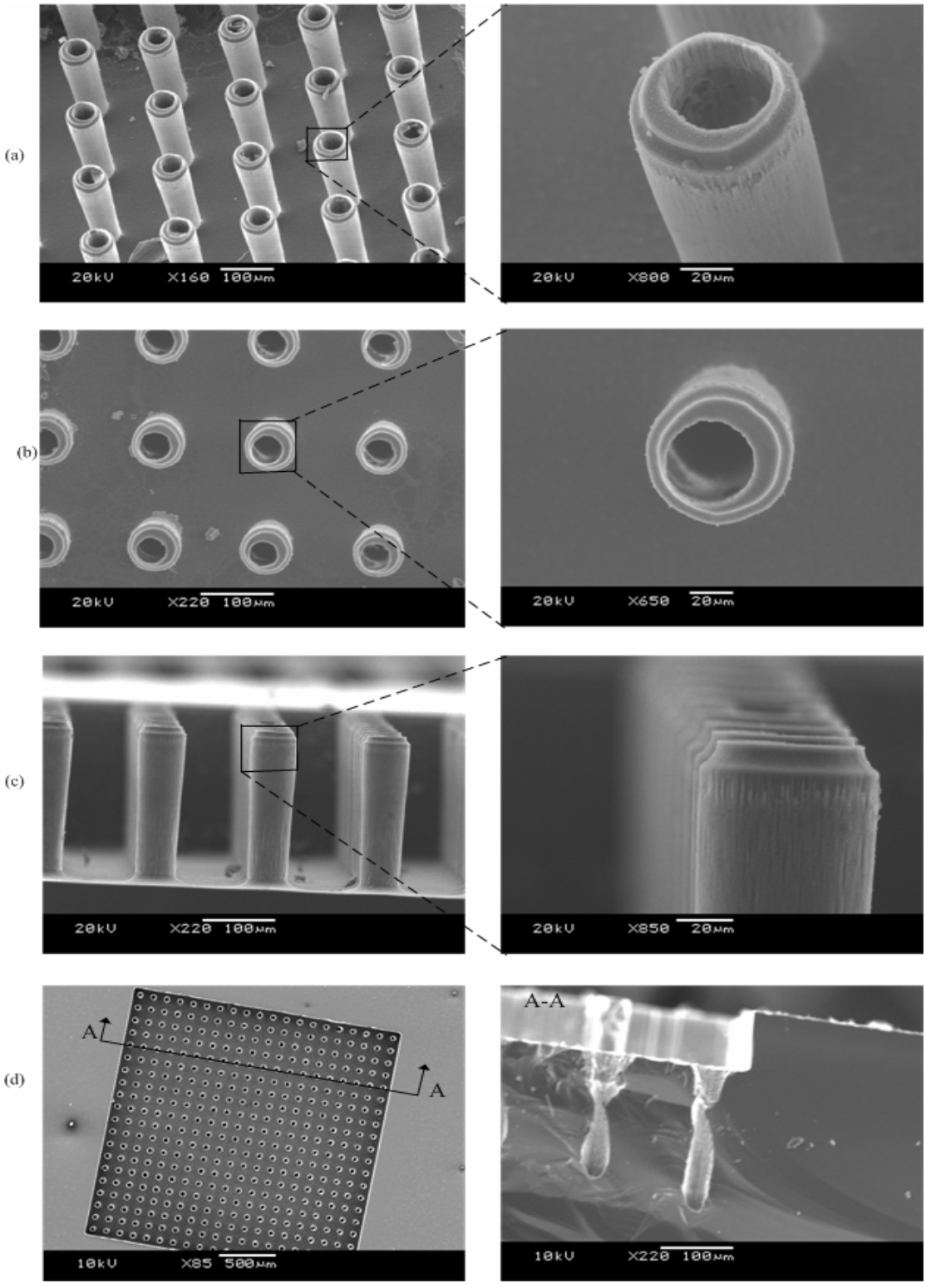

Figure 5.16 SEM photos of a microneedle array: (a) a hollow microneedle array (b) plane view of microneedle array (c) side view of microneedle array (d) backside view of chamber

5.3.2 Glass Deep Wet Etch Results

The characteristics of microflow in microchannel are significantly different to conventional channels at large scale. It was found that the surface roughness of channel has high effect on the earlier transition of laminar to turbulent flow than the predictions by the conventional theory [118]. Additionally, it has been found that the surface roughness has influence on the properties of flow friction and heat transfer in microchannels.[119][120] Therefore, researches on 2-D and 3-D simulation have been carried out to investigate the various effects of surface roughness on liquid in microchannel.[121][122] Those simulation results confirmed that the smooth surface has high agreement with predictions through conventional theory.

The surface roughness of glass sample after etching was measured to study the influence of etchants on the quality of the etched surface. The four etchants, concentrated HF, and HF and HCl with ratios at 10:0.5, 10:1, and 10:1.5, were set up for the etching of Pyrex 7740 and Soda Lime glass. The etching time for all the samples tested was 15 minutes. The smallest value of roughness for both etched Pyrex 7740 and Soda Lime glass was obtained using the etchant HF: HCl with the ratio10:1 [123].

Figure 5.17 shows the different roughness of the etched Corning 7740 and Soda Lime glass in four etchants. The observed range of roughness value ranged from 2 to 8 nm for the Pyrex 7740 glass in four etchants. The lowest value of roughness for the etched Soda Lime glass was

achieved in the solution HF:HCl with the ratio10:1. The surface roughness of the etched Soda Lime glass in concentrated HF solution was 5 times greater than the surface roughness of the etched Corning 7740 glass. The highest value of surface roughness was generated in wet etching using concentrated HF; and the lowest value of surface roughness was achieved in the optimal solution HF: HCl with the ratio10:1. The value of surface roughness for Soda Lime glass etched in concentrated HF was as great as 34 nm, while the value of the surface roughness is only 8 nm in the etchant HF:HCl with ratio 10:1. It was observed that a rougher surface was generated at the Soda Lime glass than the glass of Corning 7740. By adding amount of HCl solution into concentrated HF, the value of surface decreased.

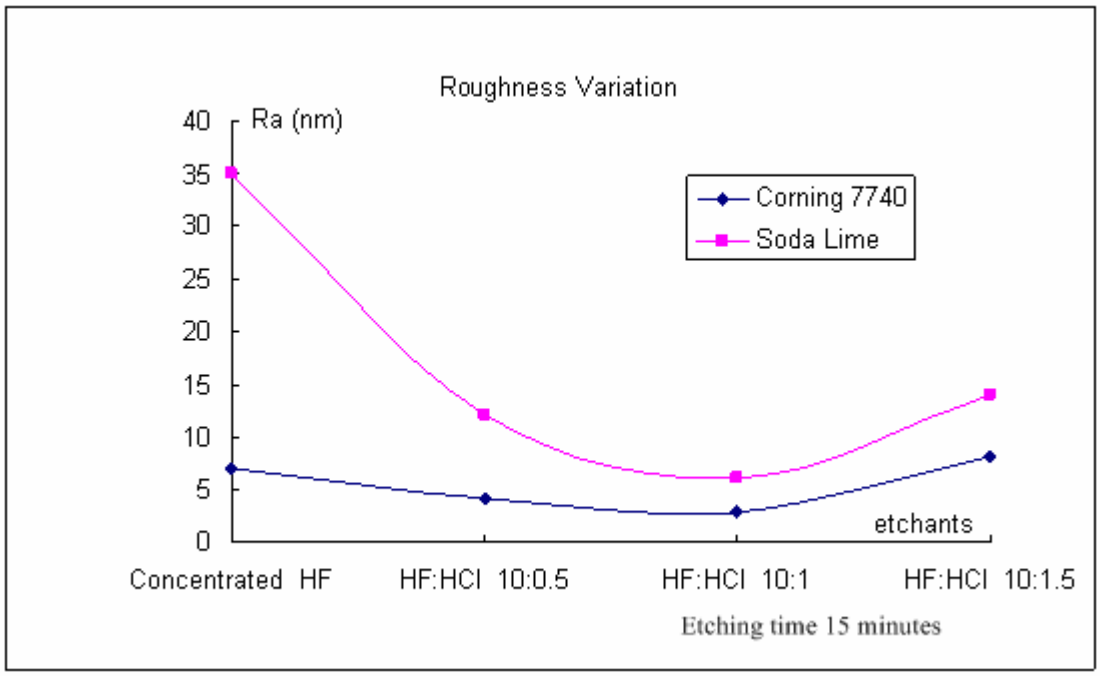

Figure 5.17 Roughness (Ra) variations in the four types of etchant

Figure 5.18 shows the etching rates of the Coning 7740 and Soda Lime glass in four etchants. It was observed that the etching rate in the solution of HF with additional HCL decreased up to 7-8% of that in concentrated HF for the etching of Corning 7740 glass. The etching rate was insignificantly affected (variation less than 3%) by adding amount of HCl for the Soda Lime glass. The etching rate of Soda Lime glass was greater than the rate of Coning 7740 in every etchant.

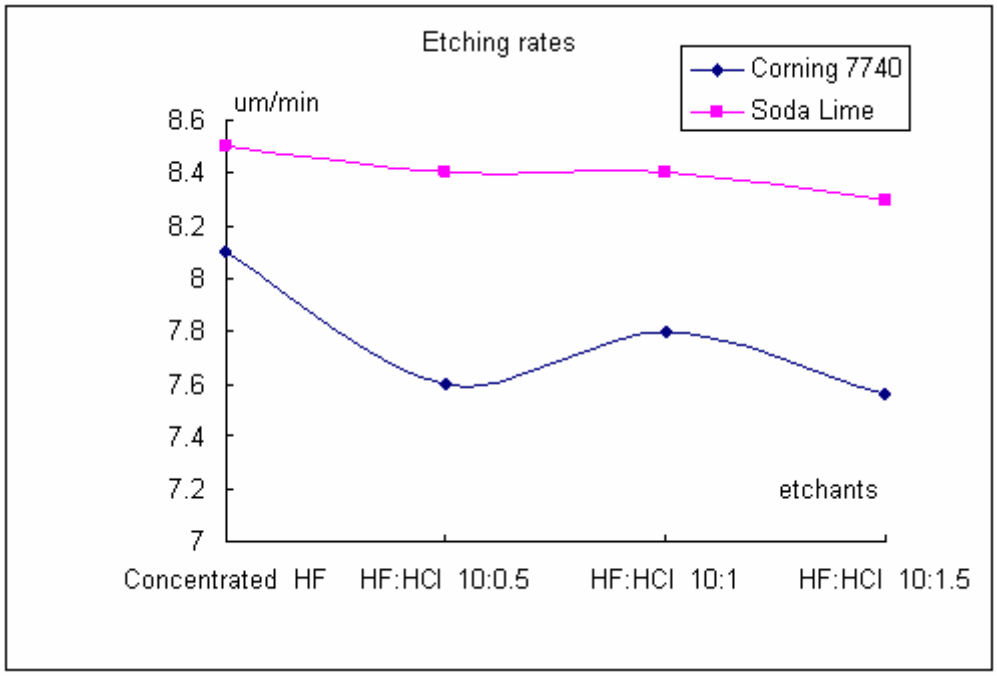

Figure 5.18 Variation of etching rates in four etchants

The variation of roughness in time is another important issue for wet polishing and deep wet etching of channels. Figure 5.19 shows the variation of roughness for glasses (Corning 7740 and Soda Lime) versus time for concentrated HF and solution of HF: HCl with ratio 10:1. It was found that the relationship between roughness and time was approximately linear in both

solutions. With the increased etching time, the surface roughness of both two glasses in the two solutions increased proportionally. The influence of HCl is more significant on the generated surface of Soda Lime glass than the surface of Corning 7740. The surface roughness (Ra) reached 70 nm using the concentrated HF at 40 minutes for Soda Lime glass, while the roughness decreased to only 20 nm using the improved etchant HF: HCl with ratio 10:1.

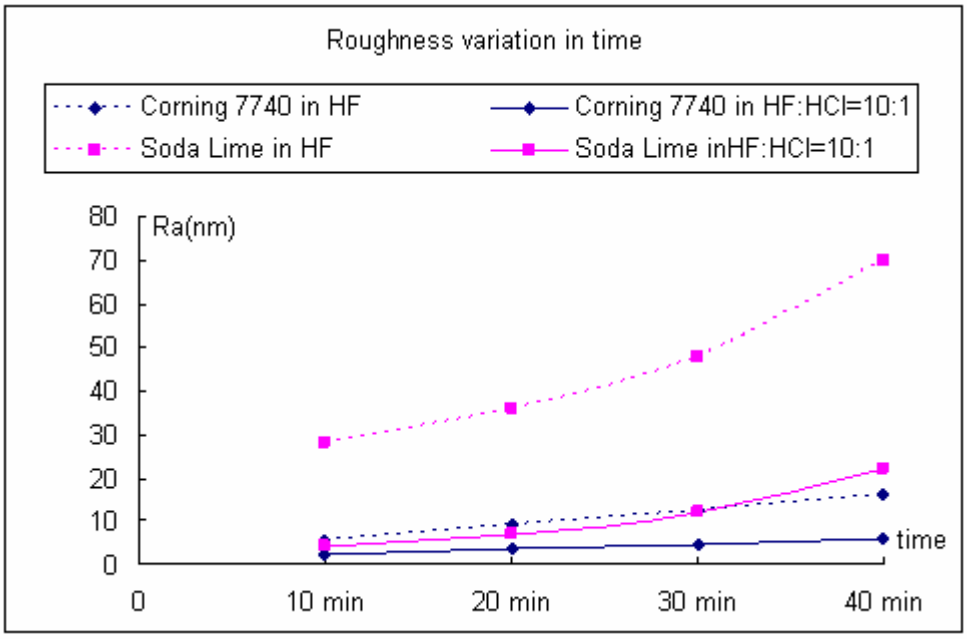

Figure 5.19 Variation of roughness with time

Atomic force microscopy (AFM) was used to investigate the surface characters of etched glass. The images of the Corning 7740 glass surface after wet etching in concentrated HF and in solution of HF: HCl with ratio 10:1 are shown in Figure 5.20 (a) and Figure 5.20 (b) respectively. The scan area of these AFM images was 10 μm by 10 μm. It was found the surface of Corning 7740 glass generated in the solution HF: HCl with ratio 10:1 was smoother than the

surface generated in concentrated HF, as shown in the topography pictures of etched glass surface.

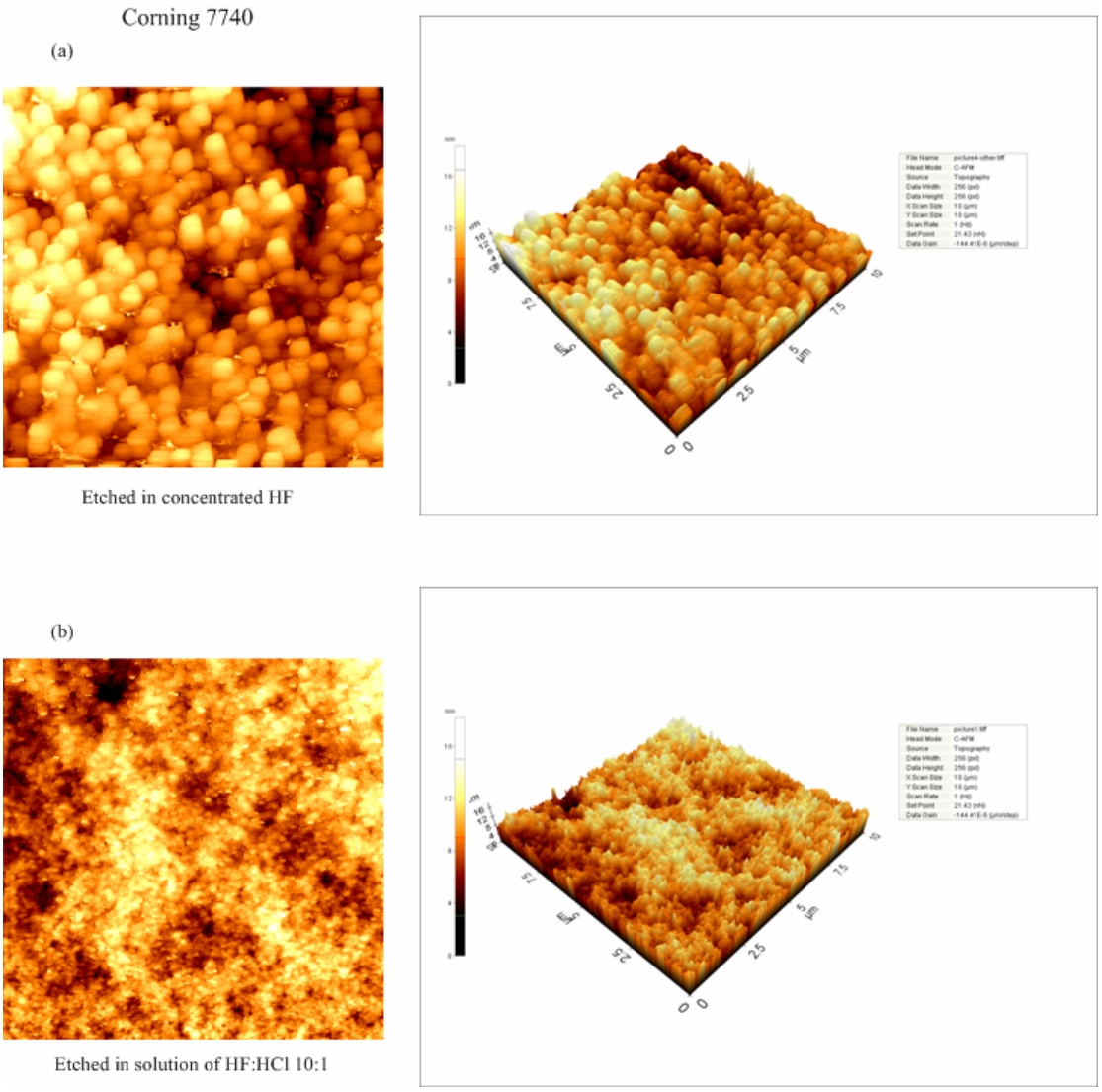

Figure 5.20 AFM images of generated surface of Corning 7740 ((a) etched in concentrated HF and (b) etched in the solution of HF: HCl with ratio10:1)

Figure 5.21 shows the AFM images of etched Soda Lime glass surface in the concentrated HF and solution of HF: HCl with ratio 10:1. The obvious improvement of surface quality was presented from the typography images. Certain compositions such as CaO and MgO was

removed in the chemical reaction, leaving holes in the surface, while the insoluble products, for example, CaF and MgF, were deposited onto the surface forming in bulgy areas. Figure 5.21 (a) clearly shows the jagged surface generated in concentrated HF. By adding certain amounts of HCl, the mass of insoluble products would be reduced, resulting in less deposition onto the surface. The bulgy areas of deposited by insoluble products would disappear, as shown in Figure 5.21 (b). The microholes left with removal of oxide composition in etching remained on the surface, while the areas of deposition by insoluble products decreased. These AFM topography images show that a smooth surface can be generated with the removal of insoluble products.

The investigation of surface roughness and the etched surface topography indicated that the quality of etched Soda Lime glass is not as good as that of surface of Corning 7740. The composition of two types of glasses could be an explanation of the different etching quality. There is only one oxide composition (Al_2O_3) with a small percentage 2% in Corning 7740 glass to form insoluble product during the HF wet etch. Small amount of oxide which produces insoluble product in HF could explain the diminutive variation of surface roughness when HCl was added in etching solution. In addition, small amount of the oxide would be a reason for the smooth surface was achieved even though long time HF etching was carried out to fabricate the structure in Corning 7740. The Soda Lime glass contains a lot of oxides, such as CaO, MgO and Al_2O_3, which generate insoluble products in HF with a total percentage weight of 12.9%. It was

found that the generated surface was highly dependent on the addition of HCl in the etchant. Based on above analysis, it is found that the composition of glass is an important factor for achieving a smooth generated surface. The solution HF: HCl with ratio 10:1 is recommended for Corning 7740 and Soda Lime glasses to improve the quality of surface after etching. The optimal composition of the etchant must be experimentally verified for the other type of glasses.

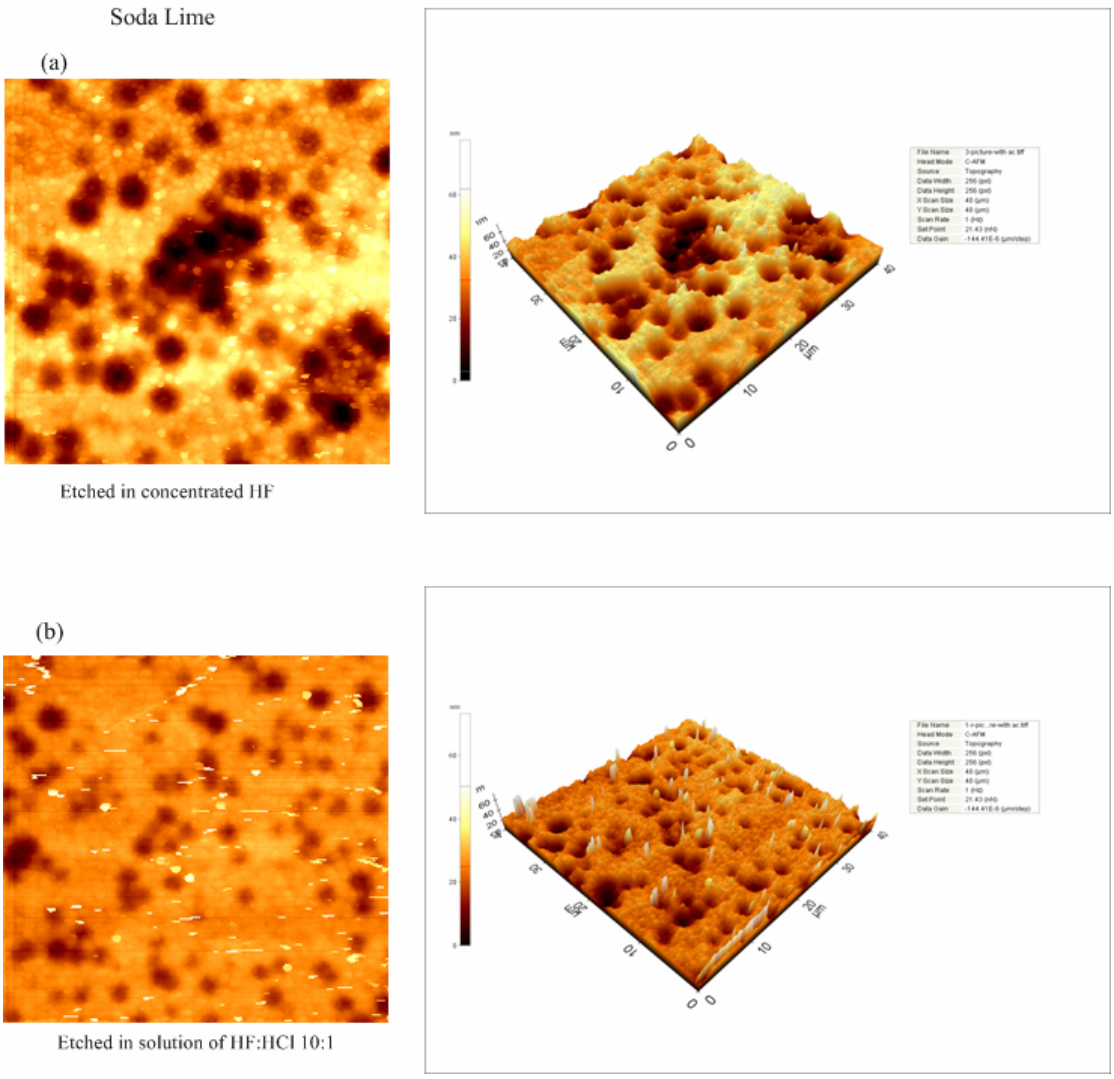

Figure 5.21 AFM images of generated surface of Soda Lime ((a) etched in concentrated HF and (b) etched in the solution of HF: HCl with ratio10:1)

There were no significant changes of the properties of main masking layers including Cr/Au, PECVD amorphous silicon and LPCVD polysilicon layers. It was found that the resistant time of photoresist reduced to 30 seconds in HF: HCl (10:1) solution as compared to the concentrated HF. The characterization of resistant time of masking layers in the two etchants HF(49%) and HF(49%):HCl (37%) with ratio10:1 is shown in Table 5.4.

Table 5.4 Resistant time of masking layers in two etchants

Masking layers	Concentrated HF	HF:HCl 10 :1
Photoresist (AZ9260)	3min	2.5min
Cr/Au(50 nm/800 nm)	13-14min	13-14min
PECVD amorphous silicon (700 nm)	>30min	>30min
LPCVD polysilicon(400 nm)	>50min	>50min

5.4 Discussion

5.4.1 Microneedle Based Microsystem

The design of a microsystem allows delivery of an accurate amount of liquid into tissue in a controlled manner. The optimal diameter of the needle inner channel was determined by the analysis of flow. The completely analytical flow modeling was established in design of the microneedle array and glass membrane. The actuation mechanism of a PZT was investigated to set up the necessary conditions of pumping at the desired flow rate. With the assumption that the glass membrane has the same deflection as PZT, the deflection of membrane has the linear relationship with the applied voltage. However, the real time deflection would be complicated in the dynamic vibration. A Michelson interferometer may be constructed to monitor the

membrane deflection by measuring the intensity variation of light caused by the displacement of membrane.

The designed microsystem with the combination of a microneedle array and actuation components has advantages in terms of the device packaging, because the microchip has the internal delivery system instead of external pumping components. The precise delivery of drug could be obtained using the accurate pumping control by the PZT. The PZT actuator provides the dynamic mode to investigate the delivery behaviors of the designed microchip. The designed inlet and outlet apertures would provide an alternative approach to operate the microchip in the static mode by the variation of the hydrostatic pressure in the chamber using a syringe.

5.4.2 Structure Improvement of the Hollow Microneedle

High aspect ration microneedle structure will fracture at the bottom of the needle during insertion. Figure 5.22 shows the SEM picture of a fracture microneedle and an intact microneedle. The long beam structure caused the fracture to occur at the bottom of microneedle where the tensile stress is at its maximum value. In order to enhance the strength of the microneedle, one approach is to deposit dielectric layers or coat thin films onto the silicon surface. The alternate approach is to design support part for the microneedle to enhance the structure strength. Figure 5.23 shows the design sketch for the support part.

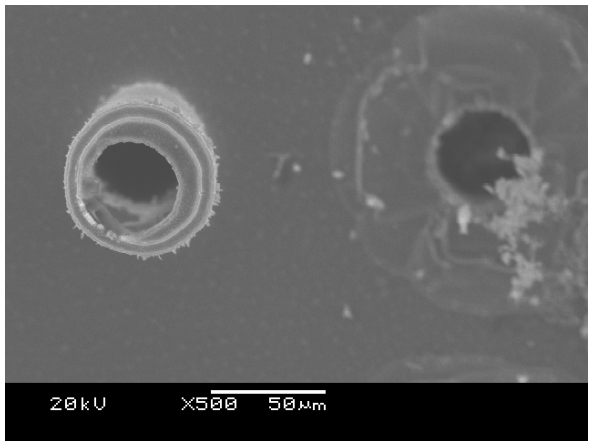

Figure 5.22 SEM photo of fracture needle after insertion (an intact needle at left and chip off needle at right left the etched inner hole. Fracture occurs at the bottom of the needle.)

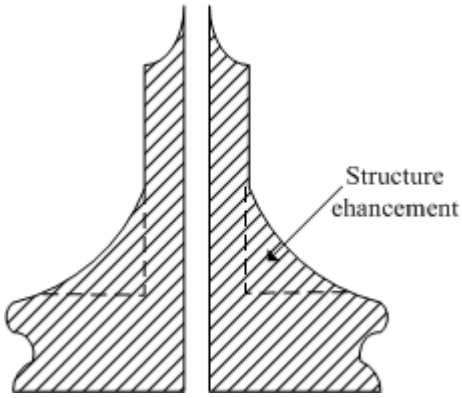

Figure 5.23 Sketch of the microneedle design with strength enhancement component

The reaction ion etching lag (RIE-lag) was applied in the fabrication of the designed microneedles with enhancement structure. RIE-lag in silicon DRIE was due to different etching rates, which are related to mask open areas, pattern size and pattern geometry [124]. New methods were developed to fabricated high density, out-of-plane, hollow microneedle array with strength enhancement utilizing RIE-lag in deep silicon etching. The fabrication

process involves a combination of photolithography, isotropic etching, deep reactive ion etching and thermal oxidation. SiDeox (silicon deep etching and oxidation) process was used in this fabrication [125]. Figure 5.24 illustrates the fabrication procedure. First, a circular mask was isotropic underetched (Figure 5.24 (a)). Second, different etching depths were achieved in deep silicon etching because of the RIE-lag effect (Figure 5.24 (c)). Third, the thermal oxidation process was carried out to grow silicon oxide on silicon wafer (Figure 5.24 (e)). The oxidation layer was subsequently removed, resulting in the microneedles with a curved profile (Figure 5.24 (f)).

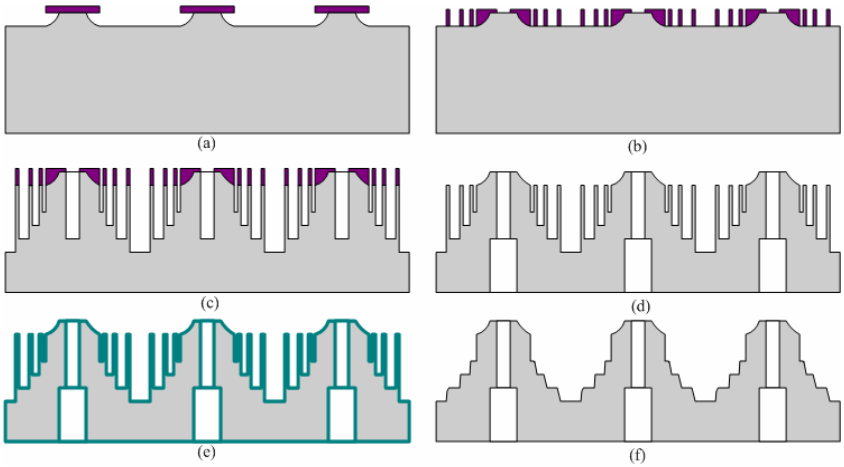

Figure 5.24 Fabrication process for microneedles with curved structure

Concentric donuts with different feature sizes were designed for fabrication of microneedles with curved profiles. Figure 5.25 shows the designed patterns on mask. The widths of three open donuts areas are marked in t_1, t_2, t_3, respectively. Variable t_1 is less than t_2; and t_2 is less than t_3. Therefore, the open areas, A_1, A_2 and A_3 have the relationship as $A_1 < A_2 <$ A3. Because of the

RIE-lag effect in deep silicon etching, the etch depths d_1, d_2 and d_3 corresponding to A_1, A_2, and A_3 would have the relation $d_1<d_2<d_3$. These uneven etch depths caused by different open areas were utilized to achieve curved profiles in the fabrication of microneedles. Characterization of the RIE-lag effect that determined the formation of curved structure was performed using different feature dimensions of donuts in STS ICP etcher. An etching model was established to present the variation of etching depths corresponding to different open areas in designed patterns. The measurement data of etched depths were used to fit the etching model in donuts etching. Many studies of RIE-lag have been done on trench etching of silicon. Jansen *et al* found that the ion angular distribution was the most important mechanism to explain RIE-lag in deep etching of trench [126]. This etching model, based on ion shadowing, may adequately account for RIE-lag effect on the donuts etching of silicon.

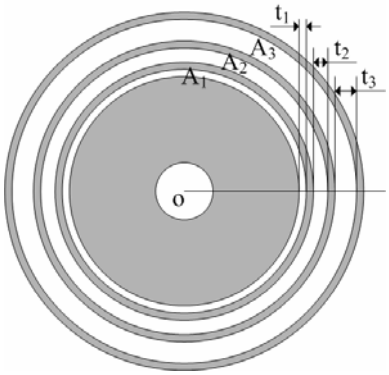

Figure 5.25 The schematic mask pattern for microneedles fabrication. ($t_1<t_2<t_3$)

Figure 5.26 shows the SEM picture of the fabricated microneedles. The microneedles with curved profile, as shown in Figure 5.26 (b), were obtained by the developed process as shown

in Figure 5.24. Furthermore, characterization and analysis of RIE-lag in designed patterns need to be carried out to obtain the improvement of the profiles for microneedle fabrication.

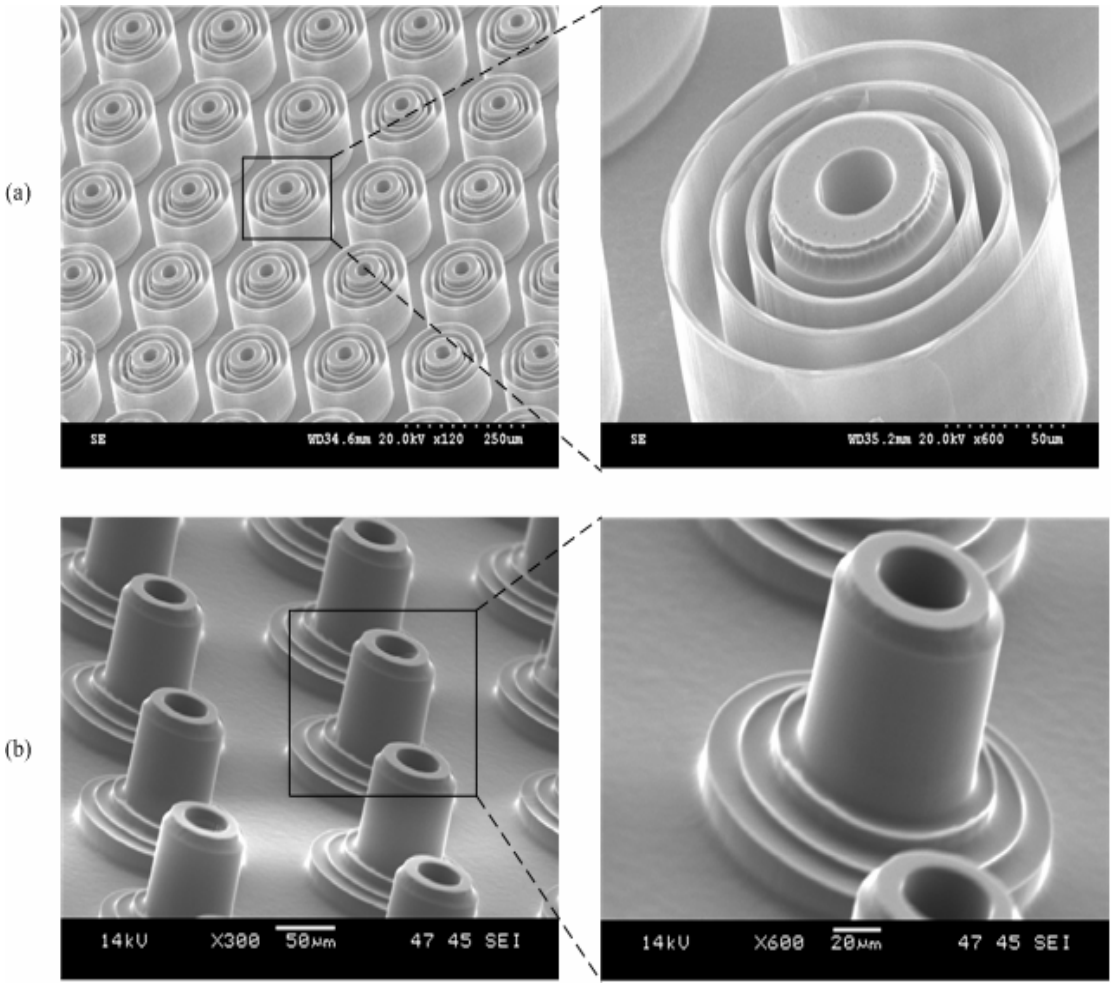

Figure 5.26 SEM pictures of fabricated microneedles with strength enhancement design ((a) after DRIE, (b) after removal of oxidation)

Chapter 6 Conclusions and Future Work

This thesis describes the concept, theory, fabrication process, insertion mechanics and flow design for microneedles in drug delivery. With the purpose of developing novel microneedles by advanced microfabrication technologies for controlled drug delivery, microneedle with biodegradable tips was fabricated for transdermal drug delivery, and a hollow microneedles based microsystem was designed and fabricated to deliver drugs at desired flow rate into tissues.

6.1 Summary of Results

With the developed isotropic dry etching in ICP etcher, microneedles with the sharp tips of radius ~500 nm were fabricated using SF_6/O_2 gases. A silicon microneedle array with biodegradable porous tips was subsequently fabricated based on the former isotropic etched microneedles. The method of photoresist reflow was developed for exposes the top part of tip; and the parameters of anodic electrochemical etching were investigated and characterized to achieve various porosity tips.

The full factorial factors design method was used in the characterization for isotropic etching process in ICP etcher. The influence and co-efficiency of etching parameters were clearly interpreted by their weights of standard effects in the DOE model. This may explain why that

the random, out-of-order properties of this statistical design method fit the analysis of the process with correlated and interactional variables.

An analytical model for analysis of the critical loadings based on the square-based pyramidal structure was derived in the thesis. The analytical model provides quantitatively calculated results of the loadings on the specific microneedle structure to predict whether the microneedle could be inserted into tissues without damage.

The results of insertion testing of microneedle into skin confirmed the prediction from the analytical model. The fabricated microneedles were successfully inserted into the skin with very few damage in the transdermal testing experiments. The dye was found in the upper dermis layer after removal of the microneedles. The microneedle with porous tips would load more particles in the delivery. It is possible to speculate that the porous structure provided a novel loading method for drug adhesion to the porous tips because of their capillary property.

The microsystem including hollow microneedle array, glass chamber and actuation components was designed and fabricated. The analysis model of flow design and actuator mechanics was built to estimate the diameter of inner channel and the work conditions of PZT actuator. The high aspect ratio microneedle structure was achieved using the combination of isotropic etching and DRIE process. A hollow microneedle array was fabricated using DRIE,

SF_6/O_2 isotropic etching and a series of photolithography processes. Compared to the microneedle tube fabricated in BOSCH process, the developed microneedle with isotropic etching tips required a small insertion force. Glass with pressure chamber, fluidic channel was etched in the improvement etchant. The deep wet etching of glass was carried out in the improved etchant to generate low roughness surface. The surfaces of etched glass samples were characterized and compared by analysis of AFM topography images.

6.2 Major Contributions

The major contributions of this thesis are summarized as follow:

- *Development of the microneedle with porous tips for drug delivery*

The biodegradable material properties of macroporous silicon in the microneedles developed in this study are of considerable importance in drug delivery since they suggest that drug could be released in a controlled way accompanying with the dissolution of porous tips. The biodegradable tips would overcome the inflammation caused by breakage issues of microneedle insertion. The porous silicon could provide an approach for drug loadings. In addition, the electrochemical etching results of porous tip formation could be used to achieve certain pore size and layer depth for fabrication of the other structures such as trench and holes.

- *Application of DOE model in process characterization*

The findings on the use of DOE method in characterization suggests the DOE method is adaptable to analysis of the process whose parameters have co-effects on the process results. The effect of variables and interacted influence on the etching results would be clearly presented in the design of experiments method. Based on the characterization results, the process parameters would be adjusted in order of the effect weight on results.

- *Development of analytical model for loading analysis*

The analytical model has been demonstrated to be suitable for pyramidal structure and could be adapted for other cone-tape structures loading analysis using the derived equations in Chapter 4 with modified momentum of cross-section. The analytical model would be use to predicate the critical loadings for microneedle fracture with substitution of exact value for microneedle dimensions. The investigation of variation of critical loadings with adjusting the top length and bottom length would provide the reasonable range of dimension for the insertion requirements, which is the ability of microneedle to successfully insert into the skin in the transdermal drug delivery.

- *Development of microsystem prototype based on the hollow microneedle*

The prototype of microneedle array bonding with glass chamber using PZT actuation system would apply for delivery of accurate amount of liquid. The model in flow design would be used for the design of microfluidic channel. The analysis of actuation mechanics would be applied to

estimate the operated conditions of PZT-glass pumping. The method of two masking layers with different pattern was developed to fabricate the inner holes and outside shape with different etching depths. This multilayer masking technology would be used to fabricate microstructure in 3-D dimension instead of 2-D plane. The enhancement of etchant for glass deep wet etch would be used for the glass with high percentage of oxides whose products from chemical reaction with HF are insoluble while the chemical reaction products with HCL are soluble. The deferent solubility of chemical reaction products with different etchants would explanation the various roughnesses of etched surface. Furthermore, the microsystem with PZT pump components can be used in automatic drug delivery in precise dosages by integrating with microprocessor.

6.3 Suggestions for Future Work

Future work for the microneedles spans a wide range of fields, from material science to mechanism of microneedle insertion into skin to microelectronics fabrication and packaging to in vivo studies. The following presents suggestions for future work to address some important issues in these areas.

- *Materials Science*

The application of the porous silicon in microneedles was based on the biodegradable material properties of the nano-structure silicon, which was achieved in electrochemical etching. The

pore size and porosity of the etched silicon layer highly depend on the etching conditions such as current density, components of electrolyte and etching protected layers. Chapter 3 clearly demonstrated the process of porous silicon structure forming in anodic electrochemical etching. However, it is difficult to draw conclusions about the mechanical properties of the fabricated porous structure, because the product from the electrochemical etching is not stable due to the residual stress after etching. Future work in this area should focus on the formation mechanism of the porous silicon and the effects of the experimental variables. Follow-up investigation may involve conducting additional experiments with parameter characterization on the residual stress in the porous layer. The method of indentation investigation [104] could be used for the stress investigation of porous silicon layer.

- *Mechanism of microneedle Insertion into skin*

The insertion mechanism of microneedle was limitedly addressed because of the few data for material properties of skin. Current investigation of microneedle insertion into skin was mostly measure of insertion force which is based on the geometry microneedle. An intact model of insertion behavior has not been well developed yet. The analytical model based on the fabricated microneedle was establishing in this study to predicate the fracture. However, the investigation of skin deformation would be a better solution to predict the real time force during the insertion. Hence, the study of the model of microneedle insertion into the skin would be a further direction for analysis the insertion behavior in transdermal drug delivery.

- *Microelectronics fabrication and packaging*

The structural properties of microneedles are highly influenced by the dry etching process conditions. The fabrication processes of the HAR microneedle consists of isotropic etching step and anisotropic etching step. It is necessary to optimize this time multiplex process to achieve high-aspect-ratio microneedles with sharp tips. The DOE method which was described for characterization of isotropic etching process in Chapter 3 should be used for optimization of the combination process to fabricate structure with short processing time.

The packaging of the microneedles is important for their use in real applications particularly in drug delivery. Microsystems based on microneedles would potentially require the incorporation of a number of active components such as a battery, a PZT driven device and a microprocessor. Some of these components are used currently in medical devices; and some companies, for example microflux®, could provide solution for transdermal delivery using solid microneedles. However, the microsystem using hollow microneedles would have additional requirements in the packaging. These include metallization of a conductive layer, location of the PZT driven disc and interconnection between the microprocessor and driven circuit.

- *In vivo testing*

The test results in Chapter 4 show the microneedles have the ability to deliver drug into model tissue. For application in human delivery, it must be shown that the microneedles operate in living system. Therefore, animal testing need to be carried out after the testing of the model delivery system was done. Later in vivo studies could utilize measurement of delivery rate, total mass delivery, and concentration vs. time profile in the animal to postulate the type of mass transport mechanisms for the microneedle based microsystems.

Bibliography

[1] R. Langer. New Methods of Drug Delivery, Science, *249*, pp.1527-1553. 1990.

[2] R. Langer. Drug Delivery and Targeting, Nature Reviews, *392*, pp.5-10. 1998.

[3] D. Liepmann, A. Pisano and B. Sage. Microelectromechanical Systems Technology to Deliver Insulin, Diabetes Technology & Therapeutics, *1*, pp.469-476. 1999.

[4] D. Liepmann, B.H. Sage, A.P. Pisano, and R.T. Howe. Integrated μFLUME Reconstitution System for Biological and Medical Supplies, DARPA, February 1997, UK.

[5] M.L. Reed and W-K. Lye. Microsystems for Drug and Gene Delivery, Proceedings of the IEEE, *92*, pp.56-75. 2004.

[6] N.A. Peppas. Intelligent Therapeutic: Biomimetic Systems and Nanotechnology in Drug Delivery, Advanced Drug Delivery Reviews, *56*, pp.1529-1531. 2004.

[7] J.D. Zahn, N.H. Talbot, D. Liepmann, A.P. Pisano. Microfabricated Polysilicon Microneedles for Minimally Invasive Biomedical Devices, Biomedical Microdevices, *2*, pp.295-303. 2000.

[8] B.C. Towe and V.B. Pizziconi. A Microflow Amperometric GlucoseBiosensor, Biosensors and Bioelectronics, *12*, pp.893-899. 1997.

[9] D.V. McAllister, M.G. Allen and M.R. Prausnitz. Microfabricated microneedles for gene and drug delivery, Annual Review of Biomedical Engineering *2*, pp.289-313. 2000.

[10] M.R.Prausnitz. Microneedles for Transdermal Drug Delivery, Advanced Drug Delivery Reviews, *56*, pp.581-587. 2004.

[11] S.Henry, D.V.McAllister, M.G.Allen and M.R.Prausunitz. Microfabricated Microneedles: a Novel Approach to Transdermal Drug Delivery, Journal of Pharmaceutical Science, *87*, pp.922-925. 1998.

[12] D.V.McAllister, P.M.Wang, S.P.Davis, J-H. Park, P.J.Canatella, M.G.Allen and M.R.Prausunitz. Microfabricated Needles for Transdermal Delivery of Macromolecules and Nanoparticles: Fabrication Methods and Transport Studies, Proceedings of the National Academy of Sciences, *100*, pp.13755-13760. 2003.

[13] J-H.Park, M.G. Allen and M.R.Prausnitz. Biodegradable Polymer Microneedle: Fabrication, Mechanics and Transdermal Drug Delivery, Journal of Controlled Release, *104*, pp.51-66. 2005.

[14] W.Martanto, S.P.Davis, N.R.Holiday, J.Wang, H.S.Gill and M.R.Prausnitz. Transdermal Delivery of Insulin Using Microneedles *in vivo*, Pharmaceutical Research, *21*, pp.947-952, 2004.

[15] W.Lin, M.Cormier, A.Samiee, A.Griffin, B.Johnson, C.Teng, G.E.Hardee and P.Daddon. Transdermal Delivery of Antisense Oligonucleotides with Microprojection Patch, Pharmaceutical Research, *18*, pp.1789-93, 2001.

[16] J.A. Matriano, M.Cormier, J.Johnson, W.A.Young, M.Buttery, Knyan and P.E.Daddina. Macroflux Microprojection Array Patch Technology: a New and Efficient Approach for

Intracutaneous Immunization, Pharmaceutical Research, *19*, pp.63-70. 2002.

[17] S.Chandrasekaran, J.D.Brazzle and A.B.Frazier. Surface Micromachined Metallic Microneedles, Journal of Microelectromechanical Systems, *12*, pp.281-288. 2003.

[18] K.Chun, G.Hashiguchi, H.Toshiyoshi and H.Fujita. Fabrication of Array of Hollow Microcapillaries Used for Injection of Genetic Materials into Animal/Plant Cells, Jpn.J.Appl.Phys. *38*, pp.279-281. 1999.

[19] M. J.Madou. Fundamentals of Microfabrication: the Science of Miniaturization, Second Edition, CRC press LLC, Boca Raton London New York, Washington DC.

[20] J.M.Bustillo, R.T.Howe, and R.S.Muller. Surface Micromachining for Microelctromechanical Systems, Proceedings of the IEEE, *86*, pp.1552-1574. 1998.

[21] G.T.A. Kovacs and K. E. Petersen. Bulk Micromachining of Silicon, Proceedings of the IEEE, *86*, pp.1536-1551. 1998.

[22] L.M. Roylance and J.B Angell. A Batch-fabricated Silicon Accelerometer, IEEE Transactions on Electron Devices, *26*, pp.1911-1917. 1979.

[23] E.Bassous, H.H Taub and L. Kuhn. Ink Jet Printing Nozzle Arrays Etched in Silicon, Applied physics Letters, *31*, pp.135-137. 1997.

[24] S.H. DeWitt. Microreactors for Chemical Synthesis, Current Opinion in Chemical Biology, *3*, pp.350-356. 1999.

[25] O.C.Jeong and S.S.Yang. Fabrication and Test of a Thermopneumatic Micropump with a Corrugated p+ Diaphragm, Sensors and Actuators A, *83*, pp.249-255. 2000.

[26] A.H.Epstein and S.D.Senturia. Macro Power from Micro Machinery, Science, *276*, pp.1211-12. 1997.

[27] A. C.R.Grayson, R. S. Shawgo, A.M.Johnson, N.T.Flynn, Y.Li, M.J Cima and R.Langer. A BioMEMS Review: MEMS Technology for Physiologically Integrated Devices, Proceedings of the IEEE, *92*, pp.6-21. 2004.

[28] D.L.Polla, A.G.Erdman, W.P.Robbins, D.T.Markus, J.D.Diaz, R.Rizq, Y.Nam,H.T.Brickner, A.Wang and P.Krulevitch. Microdevice in Medicine, Annual Review of Biomedical Engineering, *2*, pp.551-576. 2000.

[29] Mark R. Prausnitz. Current Status and Future Potential of Transdermal Drug Delivery, Nature Review Drug Discovery, *3*, pp.115-124. 2004.

[30] B.G.Amsden, M.F.A.Goosen. Transdermal Delivery of Peptide and Protein Drugs: an Overview, AIChe Journal, Bioengineering, Food and Natural Products, *41*, pp.1972-1997. 1995.

[31] Philip G. Green. Iontophoretic Delivery of Peptide Drugs, Journal of Controlled Release *41*, pp.33-48. 1996.

[32] Al-K.Mohammad , V. M. Meidan, B.M. Bozena. Iontophoretic Transdermal Delivery of Buspirone Hydrochloride in Hairless Mouse Skin, AAPS PharmSci, *5*, E14. 2003.

[33] M. R. Prausnitz. Electroporation of Mammalism Skin: a Mechanism to Enhance Transdermal Drug Delivery, Proc.Nat.Acad.Sci. *90*, pp.10504-10508. 1993.

[34] S.Mitragotri. Ultrasound-mediated Transdermal Protein Delivery, Science, *269*,

pp.850-853. 1995.

[35] T.S. Shomaker, J. Zhang, M. A. Ashburn. A Pilot Study Assessing the Impact of Heat on the Transdermal Delivery of Testosterone, J Clin Pharmacol. *41*, pp.677-682. 2001.

[36] S.Narasimha, Murthy, shobha Rani R. Hiremath. Physical and Chemical Permeation Enhancers in Transdermal Delivery of Terbutaline Sulphate, AAPS PharmSciTech, *2*, 2001.

[37] S.Henry, D.V.McAllister, M.G. Allen, and M.R.Prausnitz. Micromachined Needles for the Transdermal Delivery of Drugs, Proceedings of 11th IEEE Micro Electro Mechanical System Workshop, pp.494-498. 1998.

[38] D.V.McAllister, F. Cros, S.P. Davis, L.M. Matta, M.R.Prausnitz, M.G. Allen. Three-dimensional Hollow Microneedle and Microtube Arrays, Transducer 99, IEEE 10th Int. Conf. Solid state Sensor, Actuators, pp.1098-1101. 1999.

[39] S.P.Davis, M.R.Prausnitz and M.G.Allen. Fabrication and Characterization of Laser Micromachined Hollow Microneedles, Transducers 03, The 12th International Conference on Solid State Sensors, Actuators and Microsystems, pp.1435-1438. 2003.

[40] S.P.Davis, W.Martanto, M.G.Allen, and M.R.Prausnitz. Hollow Metal Microneedles for Insulin Delivery to Diabetic Rats, IEEE Transactions on Biomedical Engineering, *52*, pp.909-915. 2005.

[41] J-H.Park, S.P.Davis, Y-K.Yoon, M.R.Prausnitz and M.G.Allen. Micromachined Biodegradable Microstructures, Proceeding of IEEE Micro Electro Mechanical

Systems(MEMS), pp.371-374. 2003.

[42] J.A.Mikszta, J.B.Alarcon, J.M.Brittingham, D.E.Dutter, R.J.Pettis and N.G.Harvey. Improved Genetic Immunization via Micromechanical Disruption of Skin-barrier Function and Targeted Epidermal Delivery, Nature Medicine, *8*, pp.415-419. 2002.

[43] S.P.Davis, M.G.Allen, and M.R.Prausnitz. The Mechanics of Microneedles, IEEE Processing of the second joint EMBS/BMES Conference, pp.498-499. 2002.

[44] S.P.Davis, B.J.Landis, Z.H.Adams, A.G.Allen and M.R.Prausnitz. Insertion of Microneedles into Skin: Measurement and Prediction of Insertion Force and Needle Fracture Force, Journal of Biomechanics, *37*, pp.1155-1163. 2004.

[45] J.Z.Hilt and N.A. Peppas. Microfabricated Drug Delivery Devices, International Journal of Pharmaceutics, *306*, pp.15-23. 2005.

[46] I.Papautsky, J.Brazzle, H.Swerdlow, R.Weiss and A.B.Frazier. Micromachined Pipette Arrays, IEEE Transactions on Biomedical Engineering, *47*, pp.812-819. 2000.

[47] L.Lin and A.P.Pisano. Silicon-processed Microneedles, Journal of Microelectromechanical Systems, *8*, pp.78-84. 1999.

[48] J.Chen, K.D.Wise, J.F.Hetke and S.C.Bledsoe Jr.. A Multichannel Neural Probe for Selective Chemical Delivery at the Cellular Level, IEEE Transaction on Biomedical Engineering, *44*, pp.760-769. 1997.

[49] J.D.Zahn, N.H.Talbot, D.Liepmann and A.P.Pisano. Microfabricated Polysilicon Microneedles for Minimally Invasive Biomedical Devices, Biomedical Microdevices, *2*,

pp.295-303. 2000.

[50] K.Kim, D.S.Park, H.M.Lu, W.Che, K.Kim, J-B.Lee and C.H.Ahn. A Tapered Hollow Metallic Microneedle Array Using Exposure of SU-8, Journal of Micromechanics and Microengineering, *14*, pp.597-603. 2004.

[51] S.J.Moon and S.S.Lee. A Novel Fabrication Method of a Microneedle Array Using Inclined Deep X-ray Exposure, Journal of Micromechanics and Microengineering, *15*, pp.903-911. 2005.

[52] H.J.G.E.Gardeniers, R.Luttge, E.J.W.Berenschot, M.J.Boer, S.Y.Yeshurun, M.Hefetz, R.V Oever and A.VD.Berg. Silicon Micromachined Hollow Microneedles for Transdermal Liquid Transport, Journal of Microelectromechanical Systems, *12*, pp.855-862. 2003.

[53] B.Stoeber and D.Liepman. Arrays of Hollow Out-of-plane Microneedles for Drug Delivery, Journal of Microelctromechanical systems, *14*, pp.472-479. 2005.

[54] P.Griss and G.Stemme. Side-opened Out-of-plane Microneedles for Microfluidic Transdermal Liquid Transfer, Journal of Microelectromechanical Systems, *12*, pp.296-301. 2003.

[55] K.Chun, G.Hashiguchi, H.Toshiyoshi, H.Fujita, and Y.Kikuchi. An Array of Hollow Microcapillaries for the Controlled Injection of Genetic Materials into Animal/Plant Cells", MEMS'99. Twelfth IEEE International Conference of Micro Electro Mechanical Systems, pp.406-411. 1999.

[56] J.D.Brazzle, I. Papautsky, A.B.Frazier. Hollow Metallic Micromachined Needle Arrays, Biomedical Microdevices, *2*, pp.197-205. 2000.

[57] S-J. Paik, S.Byun, J-M.Lim, Y.park, A.Lee, S.Chung, J.Chang, K.Chun and D.Cho. In-plane Single-Crystal-Silicon Microneedles for Minimally Invasive Microfluid Systems, Sensors and Actuators A, *114*, pp.276-284. 2004.

[58] E.V.Mukerjee, S.D.Collins, R.R.isseroff and R.L.Smith. Microneedle Array for Transdermal Biological Fluid Extraction and in situ Analysis, Sensor and Actuators A, *114*, pp.267-275. 2004.

[59] B.Stoeber and D.Liepmann. Fluid Injection through Out-of-plane Microneedles, 1st International IEEE-EMBS Special Topic Conference on Microtechnologies in Medicine and Biology, pp.224-228. 2000.

[60] J.G.E.Gardeniers, J.W.Berenschot, M.J.Boer, Y.Yeshurun, M.Hefetz, R.Oever and A.Berg. Silicon Micromachined Hollow Microneedles for Transdermal Liquid Transfer, Proceedings of 15th IEEE international conference on MEMS, pp.141-144. 2002.

[61] P.Griss and G.Stemme. Novel, Side Opened Out-of-plane Microneedles for Microfluidic Transdermal Interfacing, Proceedings of 15th IEEE international conference on MEMS, pp.467-470. 2002.

[62] S.Chandrasekaran and A.B.Frazier. Characterization of Surface Micromachined Metallic Microneedles, Journal of Microelectromechanical Systems, *12*, pp.289-295. 2003.

[63] J. Ji, C. Iliescu, F.E.H. Tay and K.L. Tan. Optimization of the Microneedles Profile Using

Deep RIE Isotropic Etching, Proceedings of the 1st Int. Conf. on Bioengineering and Nanotechnology (ICBN), September 2004. Singapore.

[64] C. I. Hood, F. J. Schoen, S. E. Coleman and L. D. Mickley. Assessment of Tissue Reactions to Biomaterials: A Model System Using the Foreign Body Response in the Mouse Lung to Intravenously Injected Divinyl Copolymer Beads, Journal of Biomedical Materials Research, *18*, pp.1031-1041. 1984.

[65] L. Buckberry and S. Bayliss. Porous Silicon as a Biomaterial, Materials World, *7*, pp.213-15. 1999.

[66] A .Angelescu, I. Kleps, M. Mihaela, M. Simion, T. Neghina, S. Petrescu, N. Moldovan, C. Paduraru and A. Raducanu. Porous Silicon Matrix for Spplications in Biology, Rev.Adv.Mater.Sci, *5*, pp.440-449. 2003.

[67] L. Leoni, and T.A.Desai. Nanoporous Biocapsules for the Encapsulation of Insulinoma Cells: Biotransport and Biocompatibility Considerations, Biomedical Engineering, IEEE Transactions, *48*, pp.1335-1341. 2001.

[68] T.A Desai, D.J Hansford, L. Leoni, M. Essenprei, and M. Ferrari. Nanoporous Anti-fouling Silicon Membranes for Biosensor Applications, Biosensors Bioelect, *15*, pp.453-456. 2000.

[69] R.S.Shawgo, A. C. Richards Grayson, Y. Li and M. J.Cima. BioMEMS for Drug Delivery, Solid State and Materials Sciences, *6*, pp.329-334. 2002.

[70] L.Canham. Porous Silicon as a Therapeutic Biomaterial, Microtechnologies in Medicine

and Biology, 1st Annual International Conference. pp.109-112. 2000

[71] S.P.Low, K.A.Williams, L.T. Canham, and N.H.Voelcker. Evaluation of Mammalian Cell Adhesion on Surface-Modification Porous Silicon, Biomaterials, *27*, pp.4538-4546. 2006.

[72] L.T.Canham. Bioactive Silicon Structure through Nanoetching Techniques, Advanced Materials, *7*, pp.1033-1037. 1995.

[73] L.Canham, and R.Aston. Will a Chip Every Day Keep the Doctor Away? Physics World, pp.27-32. July 2001.

[74] S.C. Bayliss, R. Heald, D.I. Fletcher and L.D. Buckberry. The Culture of Mammalian Cells on Nanostructured Silicon, Advanced Materials, *11*, pp. 318-321. 1999.

[75] A.V.Sapelkin, S.C.Bayliss, B.Unal, and A.Charalambou. Interaction of B50 Rat Hippocampal Cells with Stain-Etched Porous Silicon, Biomaterial, *21*, pp.842-846. 2005.

[76] W.Sun, J.E.Puzas, T-J.Sheu, and P.M.Fauchet. Porous Silicon as a Cell Interface for Bone Tissue Engineering, Physica Status Solidi (a), *204*, pp.1429-1433. 2007

[77] J. Ji, F. E. H. Tay, J. M. Miao and J.B.Sun. Characterization of Silicon Isotropic Etch by Inductively Coupled Plasma Etcher for Microneedle Array Fabrication, Journal of Physics: Conference Series, *34*, pp.1137-1142. 2006.

[78] S.A.McAuley, H.Ashraf, L.Atato, A.Chambers, S.Hall, J.Hopkins and G.Nicholls. Silicon Micromachining Using a High-density Plasma Source, Journal of Physics. D:

Applied Physics, *34*, pp.2769-2774. 2001.

[79] M.W.Jenkins, M.T.Mocella , K.D.Allen and H. H.Sawin. The Modeling of Plasma Etching Processes Using Response Surface Methodology, Solid State Technology, *29*, pp.175-182. 1986.

[80] G.Z.Yin and D.W.Jillie, Solid State Technology. Orthogonal Design for Process Optimization and its Application in Plasma Etching, *30*, pp.127-132. 1987.

[81] A.A.Ayon, R.Braff, C.C.Lin, H.H.Sawin and M.A.Schmidt. Characterization of a Time Multiplexed Inductively Coupled Plasma Etcher, Journal of the electrochemical Society *146*, pp.339-349.1999.

[82] A.A.Ayon, R. Braff, C.C.Lin, H.H.Sawin and M.A.Schmidt. Influence of Coil Power on the Etching Characteristics in a High Density Plasma Etcher, Journal of the electrochemical Society, *146*, pp.2730-2736. 1999.

[83] M.A.Lieberman and A.J.Lichtenberg. Principles of Plasma Discharges and Materials Processing, John Wiley and Sons Inc, ISBN 0-471-00577-0, 1994.

[84] M. Christophersen, J. Carstensen, Feuerhake, and H. Foll. Crystal Orientation and Electrolyte Dependence for Macropore Nucleation and Stable Growth on P-type Si, Materials Science and Engineering B, *69*, pp.194-198, 2000.

[85] E. K. Prost and P. A. Kohl. The Electrochemical Oxidation of Silicon and Formation of Porous Silicon in Acetonitrile, J. Electrochem.Soc. *141*, pp.1006-1013. 1994.

[86] E. V. Astrova, T. N. Borovinskaya, A. V. Tkachenko, S. Balakrishnan , T. S. Perova,

A .Rafferty and Y. K. Gun'ko. Morphology of Macro-pores Formed by Electrochemical Etching of P-type Si, J. Micromech. Microeng. *14*, pp.1002-1028. 2004.

[87] O. Bisi, S. Ossicini and L. Pavesi. Porous Ailicon: a Quantum Sponge Structure for Silicon Based Optoelectronics, Surface Science Rep. *38*, pp.1-126. 2000.

[88] A.J. Mucha. The Gases of Plasma Etching: Silicon-based Technology, The Solid State Technol. *28*, pp.123-127. 1985.

[89] P.T. Docker, P. Kinnell and M.C.L. Ward. A Dry Single-step Process for the Manufacture of Released MEMS Structures, J. Micromech. Microeng. *13*, pp.790-794. 2003.

[90] J.C.Mogab, C.A.Adams and L.D.Flamm. Plasma Etching of Si and SiO2: the Effect of Oxygen Additions to CF_4 Plasmas, J.Appl.Phys. *49*, pp.3796-3803. 1978.

[91] X. Zhu, W.D.Greve and K.G. Fedder. Characterization of Silicon Isotropic Etch by Inductively Coupled Plasma Etch in Post-COMS Processing, Proc. IEEE MEMS, pp.568-573, 2000.

[92] J. Ji, F. E. H. Tay, J. M. Miao and C. Iliescu. Microfabricated Microneedle with Porous Tip for Drug Delivery, J. Micromech. Microeng. *16*, pp.958-964. 2006.

[93] C.Levy-Clement, S.Lust, M.Mamor, J.Rappich and Th.Dittrich. Investigation of P-type Macroporous Silicon Formation, Physica Status Solidi A, *202*, pp.1390-1395. 2005.

[94] S.M.Hossain, J.Das, S.Chakrabory, S.K.Dutta and H.Saha. Electrode Design and Planar Uniformity of Anodically Etched Large Area Porous Silicon, Semiconductor Science and Technology, *17*, pp.55-59. 2002.

[95] W.Y.Mai and G.A.Atkins. Further Comments on J-shaped Stress Curves and Crack Resistance of Biological Materials, Journal of physics D: Applied physics, *22*, pp.45-44, 1989.

[96] B.P. Perecira, P.W.Lucas, T. Swee-Hin. Ranking the Fracture Toughness of Thin Mammalian Soft Tissues Using the Scissors Cutting Test, Journal of Biomechanics, *30*, pp.91-94. 1997.

[97] Griffith, A.A. The Phenomena of Rupture and Flow in Solid, Phil. Trans.R.Soc.Lond.A, *221*, pp.163-198. 1921.

[98] Irwin. G.R, Analysis of Stress and Strain near the End of a Crack Transversing a Plate, J.Appl.Mech., *24*, pp.361-364. 1957.

[99] N-T, Nguyen and S.T.Wereley. Fundamentals and Applications of Microfluidics, Artech House, Norwood, MA, 02062, 2002.

[100] C.R.Hibbeler. Mechanics of Material, Fourth edition (Prentice Hall: Upper Saddle River New Jersey) 2000.

[101] K Anestou, Papadimitriou, C. Tsamis and Nassiopoulou. Stress Characteristics of Suspended Porous Silicon Microstructures on Silicon, Journal of Physics: Conference Series, *10*, pp.309-312. 2005.

[102] G. W. Smith. Analytic Solutions for Tapered Column Buckling, Computer & Structures, *28*, pp.677-681. 1988.

[103] P.S.Duttagupta, L.X.Chen, A.S. Jenekhe and M. P. Fauchet. Microhardness of Porous

Silicon Film and Composites, Solid State Communication, *101*, pp.33-37. 1997.

[104] D. Bellet, P. Lamagnere, A.Vincent and Y .Brechet. Nanoindentation Investigation of the Young's Modulus of Porous Silicon, J.Appl. Phys. *80*, pp.3772-3376. 1996.

[105] Ph.Luginbuhl, P.-E.Indermuhle, M.-A.Gretillat, F.Willemin, N.F.de Rooij, D.Gerber, G.Gervasio, J.-L.Vuilleumier, D.Twerenbold, M.Duggelin, D.Mathys and R.Guggenhein. Femtoliter Injection for DNA Mass Spectrometry, Sensors and Actuators B, *63*, pp.167-177. 2000.

[106] J.A.Fay. Introduction to Fluid Mechanics, MIT Press, Cambridges, 1994.

[107] E.Stemme and G.Stemme. A Valveless Diffuser/Nozzle-based Fluid Pump, Sensors and Actuators A, *39*, pp.159-167. 1993.

[108] A. Olsson, G. Stemme and E. Stemme. A Valve-less Planar Fluid Pump with Two Pump Chambers, Sensors and Actuators A , *46-47*, pp.549-556. 1995.

[109] A. Olsson, P. Enoksson, G. Stemme and E. Stemme. A Valve-less Planar Pump Isotropically Etched in Silicon, Journal of Micromechanics and Microengineering, *6*, pp.87-91. 1996.

[110] A. Olsson, G. Stemme and E. Stemme. Diffuser-element Design Investigation for Valve-less Pumps, Sensors and Actuators A, *57*, pp.137-143. 1996.

[111] A. Olsson, P. Enoksson, G. Stemme and E. Stemme. Micromachined Flat-walled Valve-less Diffuser Pumps, Journal of Microelectromechanical Systems, *6*, pp.161-166. 1997.

[112] F. White. Viscous Fluid Flow, Boston: McGraw- Hill, 2nd Edition. 1991

[113] B.Husband, M.Bu, A.G.R.Evans and T.Melvin. Investigation for the Operation of an Integrated Peristaltic Micropump, Journal of Micromech. Microeng., *14*, pp.S64-S69 2004.

[114] B.Husband, M.Bu, V.Apostoloulos, T.Melvin and A.G.R.Evans. Novel Actuation of an Integrated Peristaltic Micropump, Microelectronic Engineering, *73-74*, pp.858-863. 2004.

[115] L.Cao, S.Mantell and D.Polla. Design and Simulation of an Implantable Medical Drug Delivery System using Microelectromechanical Systems Technology, Sensors and Actuators A, *94*, pp.117-125. 2001

[116] J. Ji, F. E. H. Tay, J. M. Miao and C. Iliescu. Microfabricated Silicon Microneedle Array for Transdermal Drug Delivery, Journal of Physics: Conference Series, *34*, pp.1127-1131. 2006.

[117] J. Ji, F. E. H. Tay, J. M. Miao. Microfabricated Hollow Microneedle Array Using ICP Etcher, Journal of Physics: Conference Series, *34*, pp.1132-1136. 2006.

[118] P.Hao, Z.Yao, F.He and K.Zhu. Experimental Investigation of Water Flow in Smooth and Rough Silicon Microchannels, Journal of Micormechanicis and Microengineering, *16*, pp.1397-1402. 2006.

[119] W.Qu, and D.Li. Heat Transfer for Water Flow in Trapezoidal Silicon Microchannels, Int.J.Heat Mass Transfer, *43*, pp.3925-3936. 2000.

[120] W.Qu, and D.Li. Pressure-Driven Water Flows in Trapezoidal Silicon Microchannels, Int.J.Heat Mass Transfer, *43*, pp.353-364. 2000

[121] Y.Hu, C.Werner and D.Li. Influence of Three-Dimensional Roughness on Pressure Driven Flow Through Microchannels, Journal of Fluids Engineering, *125*, pp.871-879. 2003

[122] X.Wang, C.Yap and A.S.Mujumdar. Effect of Two-Dimensional Roughness in Flow in Microchannels, Journal of Electronic Packaging, *27*, pp. 357-361. 2005.

[123] C. Iliescu, J. Ji, F. E. H. Tay, J. M. Miao and T. T. Sun. Characterization of Masking Layers for Deep Wet Etching of Glass in an Improved HF/HCl Solution, Surface and Coatings Technology, *198*, pp.314-318. 2005.

[124] C-K.Chung. Geometrical Pattern Effect on Silicon Deep Etching by an Inductively Coupled Plasma System, J.Micromech.Microeng, *14*, pp.656-662. 2004.

[125] J. Sun and J. Miao. High Performance MEMS Inductors Fabricated on Localized and Planar Thick SiO2 Layer, Electronics Letter, *41*, pp.446-447. 2005.

[126] H. Jansen, M.Boer, R.Wiegerink, N. Tas, E. Smulders, C.Neagu and M.Elwenspoek. RIE Lag in High Aspect Ratio Trench Etching of Silicon, Microelectronic Engineering, *35*, pp.45-50, 1997.

Appendix A. Publications Related to This Thesis

[1] J. Ji, F. E. H. Tay, J. M. Miao and C. Iliescu. Microfabricated Microneedle with Porous Tip for Drug Delivery, J. Micromech. Microeng., *16*, pp.958-964. 2006.

[2] J. Ji, F. E. H. Tay, J. M. Miao and J.B.Sun. Characterization of Silicon Isotropic Etch by Inductively Coupled Plasma Etcher for Microneedle Array Fabrication, J. of Phys: Conf. Ser., *34*, pp.1137-1142. 2006.

[3] J. Ji, F. E. H. Tay, J. M. Miao. Microfabricated Hollow Microneedle Array Using ICP Etcher, J. of Phys: Conf. Ser., *34*, pp.1132-1136. 2006.

[4] J. Ji, F. E. H. Tay, J. M. Miao and C. Iliescu. Microfabricated Silicon Microneedle Array for Transdermal Drug Delivery, J. of Phys: Conf. Ser., *34*, pp.1127-1131. 2006.

[5] F. E. H. Tay, C. Iliescu, J. Ji and J. M. Miao. Defect-free Wet Etching through Pyrex Glass Using Cr/Au Mask, Microsyst. Technol., *12*, pp.935-939. 2006.

[6] C. Iliescu, J. Ji, F. E. H. Tay, J. M. Miao and T. T. Sun. Characterization of Masking Layers for Deep Wet Etching of Glass in an Improved HF/HCl Solution, Surface and Coatings Technology, *198*, pp.314-318. 2005.

Conference Papers:

[1] C. Iliescu, F.E.H. Tay, J. Ji and J.M. Miao. Deep Wet Etching of Pyrex Glass for Bio-MEMS Devices, Proceedings of the 1st Int. Conf. on Bioengineering and Nanotechnology (ICBN), September 2004, Singapore.

[2] J. Ji, C. Iliescu, K. L. Tan and F. E. H. Tay. Optimization of the Profile of Nanotips for Thermoelectric Coolers, Proceedings of Japan-Singapore Symposium on Nanoscience & Nanotechnology, November 2004, Singapore

[3] J. Ji, C. Iliescu, F.E.H. Tay and K.L. Tan. Optimization of the Microneedles Profile Using Deep RIE Isotropic Etching, Proceedings of the 1st Int. Conf. on Bioengineering and Nanotechnology (ICBN), September 2004, Singapore.

[4] J. Ji, C. Iliescu, F. E. H. Tay, J. M. Miao and T. T. Sun. Characterization of Masking Layers for Deep Wet Etching of Glass in an Improved HF/HCl Solution, Proceedings of the 2nd International Conference on Technological Advances of Thin Films and Surface Coatings and 1st International Conference on Nanotechnology, July 2004, Singapore.